

A theoretical and experimental study of geometry, microstructure and mechanical properties of 316l stainless steel manufactured by direct energy deposition-based hybrid manufacturing

by

Ali Baghersaghchi Khorasani

A dissertation submitted to the graduate faculty

in partial fulfillment of the requirements for the degree of

DOCTOR OF PHILOSOPHY

Major: Industrial Engineering

Program of Study Committee:

Frank Peters, Major Professor

Scott Chumbley

Matthew Frank

Stephen Vardeman

Cameron MacKenzie

The student author, whose presentation of the scholarship herein was approved by the program of study committee, is solely responsible for the content of this dissertation. The Graduate College will ensure this dissertation is globally accessible and will not permit alterations after a degree is conferred.

Iowa State University

Ames, Iowa

2020

TABLE OF CONTENTS

ACKNOWLEDGMENTS	iv
ABSTRACT.....	v
CHAPTER 1. INTRODUCCION.....	1
Additive manufacturing	1
Direct energy deposition	2
Hybrid manufacturing.....	3
DED process parameters.....	4
Mechanical tests.....	5
Tension testing	6
Tensile shear test.....	7
Block-Shear Test.....	9
References.....	13
CHAPTER 2. EFFECT OF DIRECT ENERGY DEPOSITION PARAMETERS AND LASER REMELTING ON SURFACE QUALITY OF 316L STAINLESS STEEL	15
Introduction.....	15
Methodology and Materials	19
Results.....	22
Discussion.....	33
Effect of step over.....	33
Effect of scanning speed	34
Microstructure and Microhardness	34
Laser remelting	35
Conclusion	36
Acknowledgements.....	37
References.....	37
CHAPTER 3. A NEW TEST METHOD FOR EVALUATING INTERFACIAL BONDING STRENGTH FOR METAL ADDITIVE MANUFACTURING	40
Introduction.....	40
Theoretical Description.....	46
Methodology and Materials	55
Block Shear test	55
Tensile Shear test	58

Finite Element Method	60
Results and discussion	64
Microstructural features	64
Tensile shear test.....	67
Block shear test.....	69
Macro-fractography	70
SEM fractography	71
Conclusion	75
References.....	76
CHAPTER 4. THE CHARACTERIZATION OF MICROSTRUCTURE AND MECHANICAL PROPERTIES OF SUBSTRATE/DEPOSITED MATERIAL INTERFACE IN DIRECT ENERGY DEPOSITION	79
Introduction.....	79
Methodology and Materials	83
Results and Discussion	94
Microstructure.....	96
Heat Transfer	102
Conclusion	115
References.....	116
CHAPTER 5. CONCLUSION AND FUTURE WORK	119
Summary and Contribution.....	119
Future Work	121

ACKNOWLEDGMENTS

I would like to express my sincere gratitude to my advisor Prof. Frank Peters for the endless support of my Ph.D study, for his precious knowledge, patience, and motivation throughout my research. I would also like to thank my committee members, Prof. Scott Chumbley, Prof. Matthew Frank, Prof. Stephen Vardeman, and Prof. Cameron MacKenzie, for their guidance and contributions to this study.

Last but not least, I would like to thank my family: my parents, and sisters for their support and positive attitudes throughout my life and my work. I would also like to thank to my beloved wife, Dr. Soheila Shabaniverki for her support and encouragement along this journey.

Finally, I am grateful to my friends, colleagues, the department of Industrial and Manufacturing Systems engineering faculty and staff, for their time, help and suggestions.

Ali

ABSTRACT

This thesis presents a study of the surface quality, test design for evaluating the strength of substrate/deposited material interface, and characterization of the microstructure and mechanical properties of the interface in parts manufactured via hybrid manufacturing. Hybrid manufacturing is a term that describes the combination of additive and subtractive manufacturing within the same machine. Direct energy deposition (DED) is defined as an additive manufacturing process that typically used to repair damaged components or add features to existing parts.

In surface quality study, the influence of DED process parameters such as scanning speed, step over, and laser remelting on the surface quality of 316L stainless steel are examined. Experiments are carried out at four levels of scanning speed and four levels of step over. In this work, surface quality refers to surface texture (roughness and waviness) and mechanical properties (microhardness). A profilometer is used to measure the surface roughness and waviness. Microhardness measurements are performed on the polished samples using a LECO LM247AT microhardness tester. The microstructure morphology at different regions of deposited layer, and geometry of the beads are examined using optical microscopy. The analysis of results confirmed that the variation of surface texture with process parameters depends on bead geometry, partially melted particles, and non-uniformity of bead along the deposition direction. The measurements also showed that laser remelting is an effective technique for reducing the surface roughness and waviness of DED parts

In test design study, a new testing method which is called block shear test is developed to evaluate the substrate/deposited material interfacial bonding strength. To validate the results of block shear test of DED part, a set of specimens are manufactured, using machining process and

thereafter the block shear test is used to evaluate the bonding strength in these specimens. The analysis of results show that among the existing testing methods for evaluating mechanical properties such as tensile shear test, the block shear test is demonstrated a reliable testing method for measuring the shear strength of the interface in DED parts. The results from block shear test are compared to the standard tensile shear test theoretically and experimentally. The scanning electron microscopy is used to analyze the fracture morphology of samples after block shear and tensile shear experiments. The fractography observations showed that in block shear specimens, fracture takes place in interface plane by shear stress while in tensile shear test specimens the combination of shear and tensile fracture is observed.

In substrate/deposited material interface study, it is demonstrated that in order to prevent the formation of porosity during DED process, a suitable range of process parameters should be selected. The formation of porosity in DED part may negatively affect the mechanical properties of substrate/deposited material interface. No porosity was detected in the specimens, so the only factor that can influence the strength of the interface is microstructure. A detailed study on heat transfer mechanisms in the melt pool and their effects on melt pool geometry, microstructure and mechanical properties is undertaken. The microstructural characterization of the part is examined using optical microscopy and the strength of the interface is evaluated using block shear test. The analysis of variance (ANOVA) is employed to establish a correlation between process parameters and the strength of interface. The analysis of the results showed that yield strength has a direct correlation with scanning speed, however it is inversely proportional to the laser power and powder feed rate.

CHAPTER 1. INTRODUCCION

Additive manufacturing

Additive manufacturing (AM) is a process that allows us to produce near-net shape parts and create complex 3D objects by layering material based on a 3D model data that is not possible to build them using conventional subtractive processes. The main advantages of AM technique include low cost, low material waste, low energy usage, and complex shape-building ability. ASTM F2792-10 [1] defines additive manufacturing as "The process of joining materials to make object from 3D model data, usually layer upon layer, as opposed to subtractive manufacturing technologies." Additive manufacturing is also known as additive processes, additive fabrication, additive layer manufacturing, and additive techniques. Hederick [2] in a comprehensive review paper published in 2011 presented different categories of AM equipment and reported that there has been no sufficient information to link between AM process parameters and the microstructure and mechanical properties of parts fabricated via AM. Several essential standardization were developed by the American Society for Testing and Materials F42 Committee in 2009 to advance the AM processes [3].

ASTM F42 introduces the metal AM standard classification [4]. Based on this standard terminology, additive manufacturing processes are classified into seven major categories, including photopolymerization, material jetting, sheet lamination, material extrusion, binder jetting, powder bed fusion (PBF), and direct energy deposition (DED). Among these AM processes, sheet lamination, binder jetting, powder bed fusion, and direct energy deposition are listed as metal AM processes. Metal AM systems can be classified in terms of heat source, feeding stock, etc. For example, depending on the type of the heat source, powder bed fusion can be subdivided into two processes, including selective laser melting (SLM) and electron beam

melting (EBM). In direct energy deposition category, there are two types of energy sources, including laser and electron-beam and two types of feeding systems, including wire fed and powder fed.

Direct energy deposition

Direct energy deposition (DED) is a metal AM technique that uses focused heat source (electron beam or laser) to melt the material in order to produce complex parts or repair damage components. The melting and the deposition of the material occur simultaneously. This additive manufacturing technique is a more complex, and commonly used for repairing and maintaining of the existing parts. In DED process, either the metal powder or wire is deposited in a melt pool which is generated by a focused energy. The deposition efficiency of wires is higher compared to the powders as the powders would be melted partially. Different heat input sources can be used in this process, including plasma arc, laser and electron beam [5], [6]. Post-processing for DED is essential as it ensures that the finished part meet the design requirements. Post-processing include thermal and mechanical processes that are used to reduce the residual stress and to achieve the desired final geometry, respectively [5]. In DED systems multiple nozzles can be used to eject different materials which allows for the fabrication of functionally graded materials [7].

One of the most commercialized forms of DED process is powder fed that feed metal powder into a melt pool. In powder based DED process, a shield gas such as nitrogen or argon covers the melt pool to prevent oxidation. In addition, for reactive metals such as titanium the chamber is filled with shield gas to reduce the oxidation of powder. By using a heat source, the metal powders are melted as they are deposited in the melt pool. This process is highly precise

and capable of depositing layers of material with a thickness ranging from 0.1 mm to a few millimeters. One of the interesting features of this process is the metallurgical bonding of the deposited material with the substrate. In order to expand the potential applications of DED process and enhance their capabilities, a multi-axis system is often required. In three-axis machine the platform is stationary, however in five-axis machine it is on rotating position which allows the machine to access the different sides and produce complex geometries [5].

Hybrid manufacturing

Hybrid manufacturing technology has received significant attention in recent years due to its capability to produce various parts in a more efficient way. Hybrid manufacturing combines additive manufacturing such as 3D printing and subtractive processes such as machining within the same machine. Hybrid manufacturing can provide an appropriate solution to the drawbacks of manufacturing processes. For example, because of technological limitations of additive manufacturing processes, it is not always feasible to produce complex parts with high accuracy. Consequently, it is difficult to control dimensional accuracy, mechanical properties, etc. [8], [9]. Based on the above-mentioned problems, the combination of CNC milling for material removal and additive process that is known as hybrid manufacturing can provide new opportunities of manufacturing to produce more complex parts with high dimensional accuracy in a relatively shorter time. The process that has been used in the current thesis uses energy deposition for metal powder deposition and CNC machining for material removal that work in five-axis motion mode to minimize the production time and eliminate the post-processing.

DED process parameters

Process parameters in direct energy deposition (DED) play a significant role on the final properties of the part. The main process parameters in DED include laser power, scanning speed, and powder feed rate. The variation of these parameters may lead to different microstructure characteristics, mechanical properties, surface finish, and melt pool geometry of the part built via DED. Thus, by controlling these parameters the final product with desired microstructural features, mechanical properties, dimensional accuracy and surface quality can be achieved. In addition to these parameters, there are some parameters that are related to powder such as powder quality, powder particle size and impact temperature [10]. In the present work, only the effect of DED process parameters have been considered. In order to achieve the desired properties, firstly it is essential to have a deep understanding of the effect of process parameters on the final properties.

The effect of process parameters are analyzed by varying one parameter and at that time other parameters are kept constant. Zhang et al. [11] demonstrated the effect of laser power and scanning speed on microstructure and mechanical properties of 316L stainless steel parts manufactured by DED. The laser power was varied between 600 W and 1400 W, while the scanning speed was varied between 2 mm/s and 10 mm/s. They showed that with decreasing scanning speed and increasing laser power, yield strength and ultimate tensile strength decrease. Mahamood [12] investigated the influence of laser power, ranging from 1800 W to 3000 W, on the microstructure, mechanical properties and surface quality of titanium alloy produced by DED. He measured surface roughness and showed that better surface finish is produced at laser power of 3000 W. Shah et al. [13] demonstrated that the powder feed rate play a role in determining the size of melt pool so that with an increase in powder feed rate the melt pool area

increases. The overall effect of scanning speed in DED is that with increasing scanning speed, the surface temperature decreases and the powder would not perfectly bind to the base metal. On the other hand, with decreasing scanning speed, the surface temperature increases, leading to higher dilution and consequently lower yield and tensile strength [14]. In order to melt larger particle-sized powders in DED, more heat input and therefore more laser power or less scanning speed is needed, while smaller powders can be melted by using less heat input. Moreover, for particle size smaller than 400 mesh, the powders are not able to flow efficiently during the feeding and consequently causes some difficulties in the deposition process [15].

Mechanical tests

The mechanical properties are critical features of hybrid manufactured parts. In previous studies, the mechanical properties of the bulk region of DED parts have been examined, however the substrate/deposited part interfacial strength has not been analyzed yet. It is interesting that there was not found any standard testing method for measuring interfacial bonding strength in hybrid manufacturing. To characterize the mechanical properties of interfacial strength, the first step is to design and develop a new testing method that is capable of measuring the strength of interface. A key distinction between this work and previous studies is that the authors designed a new testing method to evaluate the interfacial strength and thereafter investigated the relationship between process parameters and microstructure and mechanical properties of substrate/deposited part interface. The following review describes the existent mechanical testing methods that are typically used to evaluate the mechanical properties of DED parts. Because of the limitations of these testing methods that are discussed in detail in the following chapters, new needs have

emerged for developing a testing method that is suitable and efficient for measuring the strength of interface.

Tension testing

Tensile test can be performed following the ASTM E8M standard [16]. This test provides information about the ductility, yield strength, and tensile strength of materials in uniaxial tensile stress condition. According to this information we are able to compare materials in terms of mechanical properties. This test is normally conducted at room temperature that ranges from 50 to 100F.

For metallic materials with nominal thickness of 5 to 12.5 mm, Plate-Type specimen is used. However, for metallic materials with nominal thickness of 0.13 to 5 mm the Sheet-Type specimen is used. Pin ends specimen is primarily used to avoid buckling that occurs either in high-strength or thin materials. For metallic materials with a nominal thickness of 12.5 to 19 mm Round test specimen is used. Small-size specimens are mostly used when gauge length is four times of diameter.

There are efforts that have examined the mechanical properties of AM parts, using tensile testing method. Liu et al. [17] have evaluated the tensile properties of silicon bronze-mild steel bimetallic plate. The tensile test specimens were extracted according to the ASTM E8M-11. The dimensions of these specimens are of length of 50 mm, width of 12.5 mm and thickness of 6 mm. In another work, Tolosa et al. [18] have measured the mechanical properties of AISI 316L stainless steel manufactured by selective laser melting (SLM) in all the possible directions in order to observe anisotropy in properties. Therefore, tensile test samples have been extracted in different directions, including 0°, 30°, 45° and 90°. They showed that tensile properties such as

yield strength of the part after SLM process are higher compared to this alloy in rolled conditions.

The main advantage of tensile test is that it is a conventional method that makes it possible to compare the results with the previous studies. Beside this, for conducting tensile test no fixture is needed. Despite all of its advantages, there are some challenges associated with this testing method. For example, the machining of test specimens is necessary before running the test. In addition, the minimum overall length of test specimen should be 100 mm, so the minimum length of printed part should be more than 40 mm. Technically, depositing such a long part layer-by-layer through AM is challenging and time consuming. In addition, defocusing of the laser beam focal point can strongly affect the dimensional accuracy of the printed part.

Figure 1 shows the schematic of two types of tensile test specimens used for AM parts.

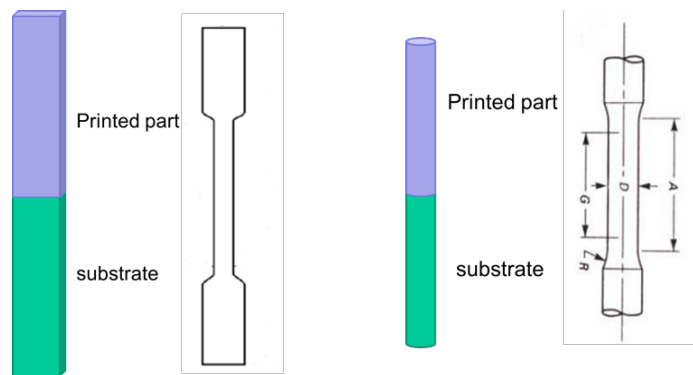


Figure 1- Schematic of two types of tensile test specimens used in additive manufacturing.

Tensile shear test

Tensile shear test is widely used in explosion welding to evaluate the strength between the interface and welded part. Compression force is applied using a universal test machine to

determine the strength of the interface once the samples that have been welded together pushed apart. Tricario et al. [19] have carried out tensile shear test to evaluate the strength of explosion-welded steel/aluminum joints and characterized the mechanical properties of the interface. They reported the final results in term of maximum shear strength of the bond interface that is in the range of 75 MPa to 90 MPa, depending on the dimension of the sample and the welding condition. Dhib et al. [20] conducted tensile shear test under the condition that the compression load is parallel to the interface and applied on the top of test specimen to determine the shear strength of stainless steel clad plates. They reported that the fracture occurs at the interface line and the value of shear bond strength of the clad plate was measured about 280 MPa. They found that the shear bond strength between the parent metal and the clad plate is higher when compared to the shear strength of the parent metal.

Tensile test specimen for AM parts consisting of a rectangular substrate with dimensions of $65 \times 25 \times 10$ mm and a printed part with dimensions of $25 \times 4.5 \times 3$ mm that is added to the substrate. The main advantage of this testing method is that for making the test specimen only a small part needed to be printed on the substrate and there is no need to print large parts which is material and time consuming. In addition, there is no need to conduct very precise and complicated contour machining process. On the other hand, to perform tensile shear test a fixture should be designed to hold the specimen during the test. The dimensions and schematic of tensile shear test is depicted in Figure 2.

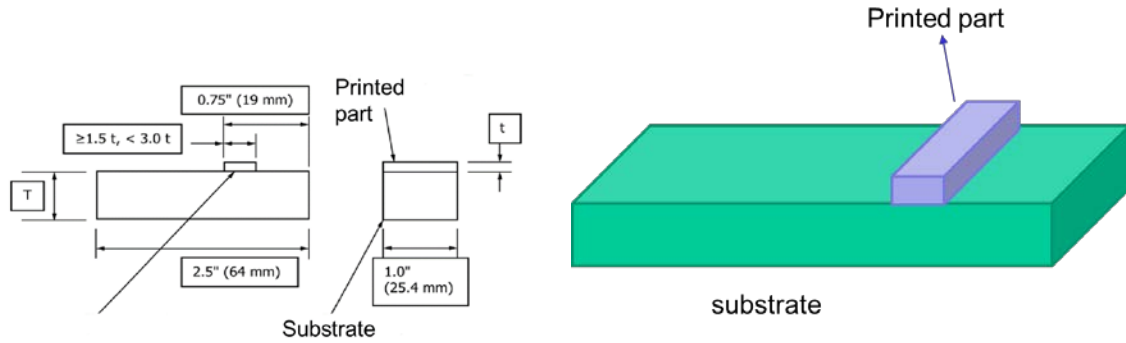


Figure 2- Dimensions and schematic of tensile shear test specimen.

Block-Shear Test

In the present thesis, the block shear testing method was proposed for determining the interfacial bonding strength of parts produced via DED. Figure 3 shows the schematic of this testing method. The detailed description of block shear test utilized by the authors and their findings on which dimensions of test specimen is best suited for block shear testing is presented in Chapter 3. Block shear test can serve as a reliable method for evaluating the strength of interface in AM parts. Like tensile shear test, to prepare the test specimen, there is no need to print large part and perform very complicated machining process. A specific fixture is designed to consistently conduct block shear experiments. The answer to block shear test is a force versus displacement graph that can be converted to stress-strain. After block shear test, the maximum force at which the specimen fails via fracture is obtained. If the fracture occurs completely in the interface of substrate and printed part, the strength of the interface can be approximately calculated as,

$$\tau = \frac{F_{max}}{A}$$

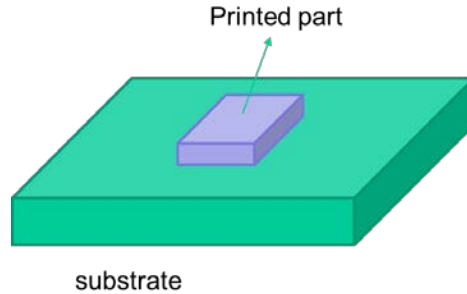


Figure 3- schematic of block shear test specimen.

This dissertation is formatted as three journal papers. To improve our fundamental understanding of the surface quality and the strength of the interface in a part manufactured via DED process, the research objectives of my research are:

Research objective 1: Evaluate the effect of DED process parameters on surface quality of 316L stainless steel-In Chapter 2 of the present thesis, the DED process is investigated to understand the influence of the scanning speed, step over and laser remelting on the surface quality of 316L stainless steel. Experiments are performed with four different scanning speeds of 200, 350, 500, and 650 mm/min, and four step over values of 0.4, 0.5, 0.6, and 0.7 mm. In this work, surface quality refers to surface texture (roughness and waviness) and mechanical properties (microhardness). The results confirm that the variation of surface texture with process parameters depends on bead geometry, partially melted particles, and non-uniformity of bead along the deposition direction. The analysis of the results showed that with increasing scanning speed from 200 mm/min and 650 mm/min, the waviness decreases. Because with varying scanning speed at a constant step over, bead height and bead width vary which eventually affect the waviness. With increasing scanning speed, the decrease in bead height, from 0.8 mm at 200 mm/min to 0.2 mm at 650 mm/min, is dominant compared to bead width. Surface roughness

generally increases with step over increasing from 0.4 mm to 0.7 mm at a constant scanning speed. The DED scanning speed also affect the microstructure and microhardness of the printed part so that with increasing scanning speed the microhardness increases from 155 HV at 200 mm/min to 180 HV at 650 mm/min which is a result of a finer microstructure. The measurements showed that laser remelting leads to a substantial reduction in average surface roughness up to 91% and average waviness up to 52%. These findings could serve as a guideline to understand the effects of process parameters on the 316L stainless steel surface texture, microhardness and microstructure that are built using DED.

Research objective 2: Develop a new test method for evaluating interfacial bonding strength for metal additive manufacturing- Chapter 3 of the present thesis aims at studying the interfacial bonding properties of hybrid manufactured (HM) parts. The authors argue that the existing testing methods for measuring the interfacial strength of the HM parts are not suitable in terms of reliability. Therefore, a new testing method which is called block shear test was developed that is capable of evaluating the shear strength of the interface. The block shear test specimen is comprised of the base substrate with dimensions of 50.8, 50.8 and 12.7 mm to which a protrusion with dimensions of 25.4, 6.35 and 3.18 mm is added via additive manufacturing. In this study, the block shear test is demonstrated as a reliable testing method for evaluating the shear strength of the interface. The results from block shear test were compared to tensile shear tests, both theoretically and experimentally. Finite element analysis was performed for computing the stress distribution in the block shear and tensile shear test specimens. Scanning electron microscopy showed that the fracture morphology of the block shear specimens contain small shear dimples that indicate the mode of fracture is dominated by shear deformation. On the other hand, the results of tensile shear test showed different behavior; fractography

observations after tensile shear test showed that the fracture does not take place in the interface plane. In other words, crack starts from the interface plane and propagate through the substrate. As a result, the dimples are large and deep, and the interfacial bonding strength is the combination of shear and tensile. The stress- displacement measurements, finite element analysis, and fractography observations proved that the block shear testing method exhibits reliable and acceptable results for the interfacial shear strength of parts manufactured via DED.

Research objective 3: Characterize the microstructure and mechanical properties of substrate/deposited material interface in a part manufactured via DED-In Chapter 4, the effect of DED process parameters on the microstructural characteristics and strength of the substrate/deposited material interface have been examined. Little is known about the mechanical properties of the substrate/deposited material interface in DED process as prior studies have only focused on the mechanical properties of the printed part. A suitable range of process parameters have been selected to minimize the formation of porosity in DED part. The microstructural characterization of the part was carried out using optical microscopy and the yield strength of the interface was evaluated using block shear test. A detailed study on the heat transfer modes and thermal history in the melt pool and their effects on microstructure and therefore mechanical properties was undertaken. The analysis of variance (ANOVA) was employed to relate the process parameters with geometry characteristics of the melt pool. As a result, a correlation between process parameters and the strength of interface was established. The metallography results detected no porosity in the parts built by DED. Thus, the only factor that can influence the strength of the interface is microstructure. In order to characterize the microstructure evolution of DED part, it is necessary to clearly define the solidification behavior under the DED

processing conditions. The results showed that yield strength has a direct correlation with scanning speed, however it is inversely proportional to the laser power and powder feed rate.

References

- [1] F42 Committee, “Terminology for Additive Manufacturing Technologies,” ASTM International. doi: 10.1520/F2792-10.
- [2] “Additive Manufacturing of Metals: A Review - Electronic Device Failure Analysis Society.” https://www.asminternational.org/web/edfas/search/-/journal_content/56/10192/CP2011MSTP1413/PUBLICATION;jsessionid=5369BB5C4B7954E6739AD9D7C0A9C1DD?p_p_id=101&p_p_lifecycle=0&p_p_state=maximized&p_p_mode=view (accessed Oct. 04, 2020).
- [3] W. E. Frazier, “Metal Additive Manufacturing: A Review,” *J. Mater. Eng. Perform.*, vol. 23, no. 6, pp. 1917–1928, Jun. 2014, doi: 10.1007/s11665-014-0958-z.
- [4] ASTM International, *Standard terminology for additive manufacturing technologies: designation F2792-12a*. West Conshohocken, PA: ASTM International, 2012.
- [5] W. J. Sames, F. A. List, S. Pannala, R. R. Dehoff, and S. S. Babu, “The metallurgy and processing science of metal additive manufacturing,” *Int. Mater. Rev.*, vol. 61, no. 5, pp. 315–360, Jul. 2016, doi: 10.1080/09506608.2015.1116649.
- [6] A. Saboori, A. Aversa, G. Marchese, S. Biamino, M. Lombardi, and P. Fino, “Microstructure and Mechanical Properties of AISI 316L Produced by Directed Energy Deposition-Based Additive Manufacturing: A Review,” *Appl. Sci.*, vol. 10, no. 9, Art. no. 9, Jan. 2020, doi: 10.3390/app10093310.
- [7] B. Onuikwe, B. Heer, and A. Bandyopadhyay, “Additive manufacturing of Inconel 718—Copper alloy bimetallic structure using laser engineered net shaping (LENSTM),” *Addit. Manuf.*, vol. 21, pp. 133–140, May 2018, doi: 10.1016/j.addma.2018.02.007.
- [8] T. Tawakoli and B. Azarhoushang, “Influence of ultrasonic vibrations on dry grinding of soft steel,” *Int. J. Mach. Tools Manuf.*, vol. 48, no. 14, pp. 1585–1591, Nov. 2008, doi: 10.1016/j.ijmachtools.2008.05.010.
- [9] R. Kolleck, R. Vollmer, and R. Veit, “Investigation of a combined micro-forming and punching process for the realization of tight geometrical tolerances of conically formed hole patterns,” *CIRP Ann.*, vol. 60, no. 1, pp. 331–334, Jan. 2011, doi: 10.1016/j.cirp.2011.03.141.
- [10] W. U. H. Syed, A. J. Pinkerton, Z. Liu, and L. Li, “Coincident wire and powder deposition by laser to form compositionally graded material,” *Surf. Coat. Technol.*, vol. 201, no. 16, pp. 7083–7091, May 2007, doi: 10.1016/j.surfcoat.2007.01.020.

- [11] K. Zhang, S. Wang, W. Liu, and X. Shang, "Characterization of stainless steel parts by Laser Metal Deposition Shaping," *Mater. Des.*, vol. 55, pp. 104–119, Mar. 2014, doi: 10.1016/j.matdes.2013.09.006.
- [12] R. M. Mahamood, "Effect of Laser Power and Gas Flow Rate on Properties of Directed Energy Deposition of Titanium Alloy," *Lasers Manuf. Mater. Process.*, vol. 5, no. 1, pp. 42–52, Mar. 2018, doi: 10.1007/s40516-018-0052-8.
- [13] K. Shah, A. J. Pinkerton, A. Salman, and L. Li, "Effects of Melt Pool Variables and Process Parameters in Laser Direct Metal Deposition of Aerospace Alloys," *Mater. Manuf. Process.*, vol. 25, no. 12, pp. 1372–1380, Dec. 2010, doi: 10.1080/10426914.2010.480999.
- [14] F. Meriaudeau, F. Truchetete, C. Dumont, E. Renier, and P. Bolland, "Acquisition and image processing system able to optimize laser cladding process," in *3rd International Conference on Signal Processing, 1996*, Oct. 1996, vol. 2, pp. 1628–1631 vol.2, doi: 10.1109/ICSPGP.1996.571205.
- [15] Y. Yang and H. C. Man, "Microstructure evolution of laser clad layers of W–C–Co alloy powders1This paper is sponsored by The Natural Science Foundation of Guangdong Province, China.1," *Surf. Coat. Technol.*, vol. 132, no. 2, pp. 130–136, Oct. 2000, doi: 10.1016/S0257-8972(00)00909-9.
- [16] E28 Committee, "Test Methods for Tension Testing of Metallic Materials," ASTM International. doi: 10.1520/E0008_E0008M-16AE01.
- [17] L. Liu, Z. Zhuang, F. Liu, and M. Zhu, "Additive manufacturing of steel–bronze bimetal by shaped metal deposition: interface characteristics and tensile properties," *Int. J. Adv. Manuf. Technol.*, vol. 69, no. 9–12, pp. 2131–2137, Dec. 2013, doi: 10.1007/s00170-013-5191-7.
- [18] I. Tolosa, F. Garcandía, F. Zubiri, F. Zapirain, and A. Esnaola, "Study of mechanical properties of AISI 316 stainless steel processed by 'selective laser melting', following different manufacturing strategies," *Int. J. Adv. Manuf. Technol.*, vol. 51, no. 5–8, pp. 639–647, Nov. 2010, doi: 10.1007/s00170-010-2631-5.
- [19] L. Tricarico and R. Spina, "Experimental investigation of laser beam welding of explosion-welded steel/aluminum structural transition joints," *Mater. Des.*, vol. 31, no. 4, pp. 1981–1992, Apr. 2010, doi: 10.1016/j.matdes.2009.10.032.
- [20] Z. Dhib, N. Guermazi, A. Ktari, M. Gasperini, and N. Haddar, "Mechanical bonding properties and interfacial morphologies of austenitic stainless steel clad plates," *Mater. Sci. Eng. A*, vol. 696, pp. 374–386, Jun. 2017, doi: 10.1016/j.msea.2017.04.080.

CHAPTER 2. EFFECT OF DIRECT ENERGY DEPOSITION PARAMETERS AND LASER REMELTING ON SURFACE QUALITY OF 316L STAINLESS STEEL

Ali Baghersaghchi Khorasani^{1*}, Frank Peters¹, Iris Rivero²

1. Department of Industrial and Manufacturing Systems Engineering, Iowa State University, 3004 Black Engineering, Ames, IA 50011
2. Department of Industrial and Systems Engineering, Rochester Institute of Technology, NY

Introduction

Direct energy deposition (DED) uses a system of a laser beam and powder delivery nozzles that converge at the surface of the material creating a melt pool to produce near net shape parts. This system follows a path to create a 2D layer of the part; this process is repeated until the desired geometry is created[1,2]. Advantages of this manufacturing process include remanufacturing and repairing applications [3], design flexibility for a part, and building part with functionally graded materials [4]. However, adequate surface quality is required to leverage these advantages.

Additive manufacturing processes typically produce surfaces that are rougher than most machining processes, and DED is no exception. The surface results from the layer wise (staircase effect) nature of the AM process [5], sticking of non-melted or partially melted particles on the free surfaces and the formation of menisci with more or less pronounced curvature radii [6]. Surface roughness and waviness are basically dependent on the DED process parameters. The process parameters also affect the microstructural characteristics (grain size and morphology) and mechanical properties (hardness and strength) of the printed part. The melt pool characteristics (i.e. shape, geometry, dynamics and degree of temperature localization) are affected by DED processing parameters that consequently impact the thermal history experienced by the part. This thermal history will directly influence the degree of porosity and

the microstructural characteristics, and thus mechanical properties of the printed part [7]. In this work, surface quality refers to surface texture and mechanical properties. The surface roughness and waviness analysis are used to characterize the surface texture. Moreover, the microstructure characterization and measuring the microhardness allow us to understand the mechanical properties of the surface.

Therefore, in order to reach desired surface characteristics, the focus should be on the DED process parameters such as scanning speed (V), laser power (P) and mass feed rate (F). In a study conducted by Peyre et al. [6], surface finish after direct energy deposition of Ti6Al4V was studied as a function of the process parameters to find the best process windows to minimize surface variation. They showed that there is a high correlation between an increased scanning speed and decreased waviness. In addition, it was shown that with increasing scanning speed there is a peak in surface roughness at 200 mm/min. Gharbi et al. [8] used DED process with a titanium alloy (Ti-6Al-4V) to study the effect of DED main parameters including scanning speed and laser power, on surface roughness and waviness as main corresponding parameters to surface finish. In their study, the scanning speed varied from 100 mm/min to 400 mm/min which led to a reduction in waviness. Mahmood et al. [9] investigated the effect of scanning speed on surface finish of Ti6Al4V manufactured by direct energy deposition. They showed that with increasing scanning speed the surface roughness increased.

The relationship between DED processing parameters and a single laser track geometry (e.g. height, width and dilution) have been established in previous studies. Olivera et al. [10] found a correlation between coaxial laser cladding parameters and single bead geometry. Their study is based on two fundamental combined parameters: powder per unit length of the laser beam (F/V) and heat input per unit length of the laser beam (P/V). It is shown that there is a linear correlation

between laser track height and F/V. They found that laser track width is a function of laser power and scanning speed. In a similar study, Ocelik et al. [11] demonstrated that a single laser track height and width have a linear correlation with F/V and $P/V^{0.5}$ respectively. Toyserkani et al. [12] showed the relationship between laser cladding parameters and a single bead geometry via finite element modeling. They showed that with decreasing laser scanning speed the laser bead height increases.

Some studies report the relationship between DED or welding tracks overlap and surface waviness. Cao et al. [13] suggested four mathematical models for the profile of a single track that was deposited by robotic welding. They showed that there is an optimum overlapping coefficient that below this value with increasing overlap the surface roughness decreases while for the overlaps higher than optimum value with increasing overlap ratio the surface roughness increases. Li et al. [14] applied stainless steel on mild steel by laser cladding technique. They showed that with increasing the overlap the surface waviness decreased in an oscillating manner. In a recent study, Ocelik et al. [15] developed a recursive model to calculate the coat geometry based on the overlap of a single track. They defined the overlap ratio (OR) as below:

$$OR = \frac{W-L}{W} \quad \text{Eq.1}$$

where L is the center distance of neighbor tracks and W is the single track width. They showed that with increasing overlap ratio, the relative surface waviness decreases. Nenadl et al. [16] proposed equations to predict the geometry of the overlapping tracks based on laser cladding parameters. This study revealed that an increase in the overlap ratio leads to a reduction in surface waviness.

A phenomenon that plays a critical role in the surface roughness of DED parts is the agglomeration of powders that cannot be fully melted in the melt pool and formation of partially melted particles [17]. The percentage of partially melted particles is a function of the standoff distance, powder size, gas flow rate, particle speed and the ratio of the melt pool area and powder stream area [18,19]. Rosa et al. [20] defined the density of partially melted particles on the surface (D_p) and investigated the influence of DED parameters on the surface roughness. They showed that the particle density does not change significantly with increasing scanning speed or laser track step.

Laser remelting is an effective technique for reducing the surface roughness and waviness of additive manufactured parts. While the thin layer of surface is remelted, the roughness and waviness of the initial surface decreases by remelting the partially melted particles and the surface tension of the melt pool, respectively [21]. Rombouts et al. [5] carried out laser remelting after deposition in DED on stainless steel 316L and concluded that laser remelting using a high laser power and low scanning speed is more effective to reduce surface roughness.

As mentioned above, DED parameters affect the microstructure and microhardness of the deposited part. Increasing the scanning speed leads to a short time for laser/material interaction. Hence, the melt pool is smaller and the solidification time decreases, resulting in smaller grain sizes [22]. Wu et al. [23] showed that with increasing scanning speed and decreasing laser power, the grain size decreases. Senthilkumaran et al. [24] defined laser power density as

$$E = \frac{P}{D_L V} \quad \text{Eq.2}$$

Where E is laser energy density, P is laser power, D_L is the laser beam diameter and V is the scanning speed. Mahmood et al. [25] used laser power density parameter and showed that with increasing laser power density the microhardness increases and then decreases.

Stainless steel 316L has higher corrosion resistance compared to the other types of stainless steel due to its molybdenum and nickel. In addition to corrosion resistance, it has good weldability in part because of its relatively low carbon content [26]. In this study, the effect of scanning speed and laser track step over on surface texture including roughness, waviness, microstructure and microhardness is investigated.

Methodology and Materials

A UMC750HAAS 5-axis vertical milling machine retrofitted with an AMBIT laser deposition head was used to produce the test pieces. The direct energy deposition head, Figure 1A, includes a laser beam and coaxial gas-powder. Argon gas was used as a shielding gas. The DED laser beam head is directed towards the substrate and creates a melt pool where material is continuously added in the process direction.

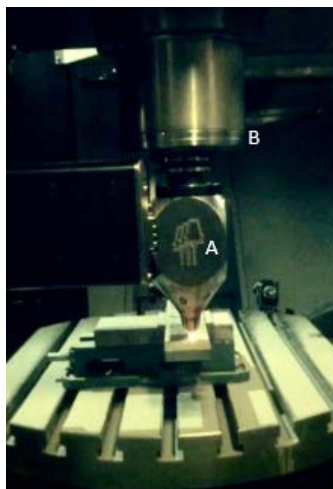


Figure 1- Experimental set-up: DED machine is depositing layers. A) AMBIT laser based DED head. B) HAAS 5 Axis Vertical Milling Machine.

The substrate material is stainless steel 316 with dimensions of 50mm x 250mm x 13mm and Table 1 shows its chemical composition. The thickness of the substrate was chosen to be 13 mm; at this thickness the component was thick enough to prevent significant distortion during processing. The powder used was 316L stainless steel, which was sold as LPW-316-AAAW from LPW Technology Inc. The particle size was between 45 to 90 μm and its chemical composition is shown in Table1. During the sample builds, the laser power and powder feed rate were maintained at 300W and 4g/min, respectively; a 1mm laser head was used. The rastering paths for the deposition layers and the laser finishing are illustrated in Figure2. The spacing between center of the tracks is defined as step over (D); four discrete values were used: 0.4, 0.5, 0.6 and 0.7 mm. To better understand the effect of DED parameters on surface texture, 4 different single beads at various scanning speeds of 200, 350, 500 and 650 mm/min were deposited. For further investigation, 7 double bead samples were deposited as following: 4 samples at scanning speed of 650 mm/min and step over of 0.4, 0.5, 0.6 and 0.7 mm; 3 samples at step over of 0.6 and scanning speed of 200, 350 and 500 mm/min.

Table1- Chemical composition of stainless steel 316 of the substrate and the powder

Material Composition	Substrate (wt.%)	Powder (wt.%)
Iron	58.23-73.61	58.23-73.61
Carbon	0-0.08	0-0.03
Chromium	16-18.5	16-18.5
Copper	0-1	0-0.75
Manganese	0-2	0-2
Molybdenum	0-3	2-3
Nickel	10-15	10-14
Nitrogen	0-0.1	0-0.2
Phosphorus	0-0.045	0-0.045
Silicon	0-1	0-0.75
Sulfur	0.35	0-0.015

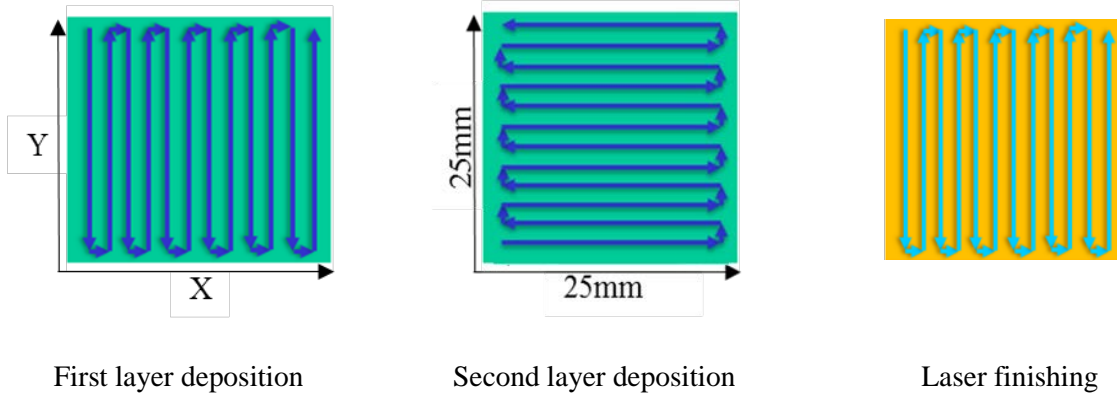


Figure 2 - Schematic illustration of scanning strategy. The spacing between the rasters is a variable of the experiment and varies from 0.4 to 0.8 mm.

Samples were made with each combination of scanning speed and step over, in addition, four additional samples were used to study the use of laser remelting, Table 2.

Table 2 - Sample number, scanning speed, step over and option of laser finish

Sample	Scanning Speed (mm/min)	Step over (mm)	Laser remelting
1	200	0.7	yes
2	200	0.7	no
3	200	0.6	no
4	200	0.5	no
5	200	0.4	no
6	350	0.7	yes
7	350	0.7	no
8	350	0.6	no
9	350	0.5	no
10	350	0.4	no
11	500	0.7	yes
12	500	0.7	no
13	500	0.6	yes
14	500	0.5	no
15	500	0.4	yes
16	500	0.4	no
17	650	0.7	no
18	650	0.6	no
19	650	0.5	no
20	650	0.4	no

A *MarSurf SD 26* profilometer was used to measure the surface roughness. It was measured perpendicular to the direction of the final deposition layer. The R_a and R_t values were recorded. The metallography samples were cut, ground and polished with a final diamond grit size of 1 μm . To reveal the microstructure, the samples were chemically etched in a methanolic aqua regia (45 ml HCL, 15 ml HNO_3 and 20 ml methanol [27].) for 5 min. Microstructure observations were carried out using Leco LX31 microscope. Microhardness measurements were performed on the polished samples using a LECO LM247AT microhardness tester using 500g load and 15s dwell time, according to ASTM E384 [28]. Focused variation technique was used to visualize the deposited layer geometry.

Results

Figure 3 shows the 16 samples that were printed. All the samples were printed with two layers; the first layer in the X-direction, followed by the second layer in the Y-direction. It should be noted that for the sample with the scanning speed of 200 mm/min and step over of 0.4 mm, the printing process could not be completed because the track overlap for these samples are too much for printing a flat layer. On the other words, the following bead is deposited on top of the previous bead instead of the substrate. For the sample with the scanning speed of 200 mm/min and step over of 0.5 mm, the deposition can be completed in the first layer. However, in the second layer due to the high temperature of first layer, the beads are deposited on top of each other in Z-direction. Consequently, the layer deposition could not be completed, and the printing process should be stopped.

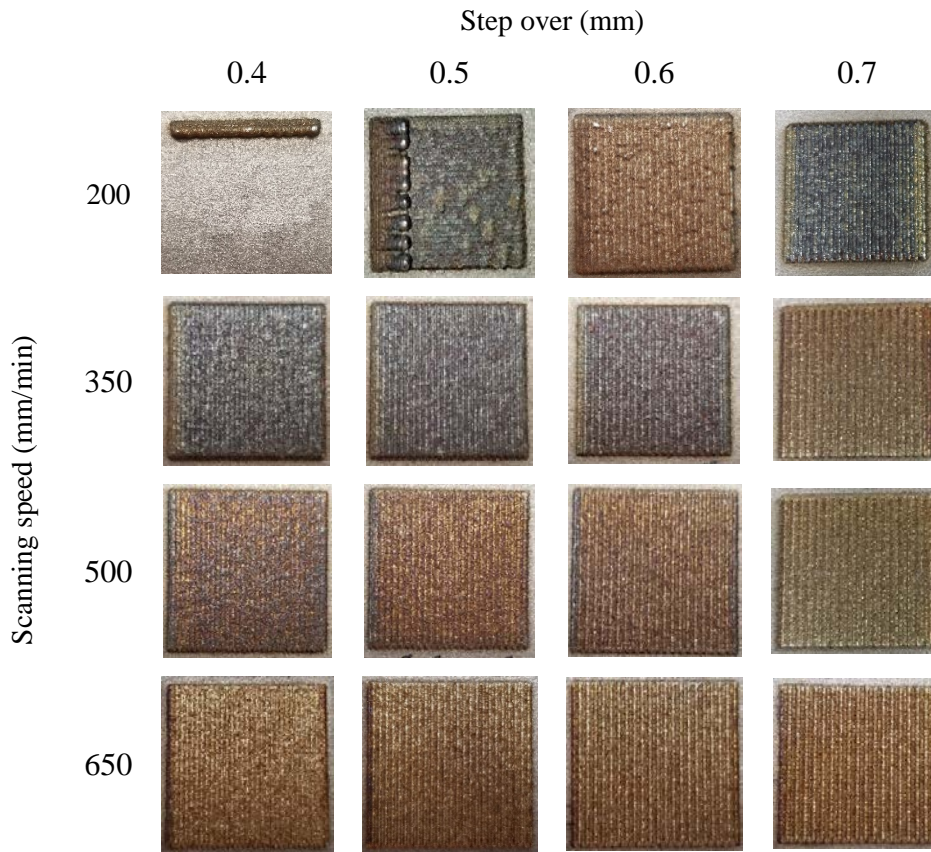


Figure 3- Depositions made at different combinations of scanning speed and step over distances.

Figures 4A and 4B show the arithmetic average R_a and the maximum height of the profile R_t , respectively. As seen in this Figure, the step over value had a bigger influence on surface roughness, with surface roughness generally increasing with higher step over values, as expected. However, there was not a discernable difference in roughness for the samples made with the 0.4 mm and 0.5 mm step over values.

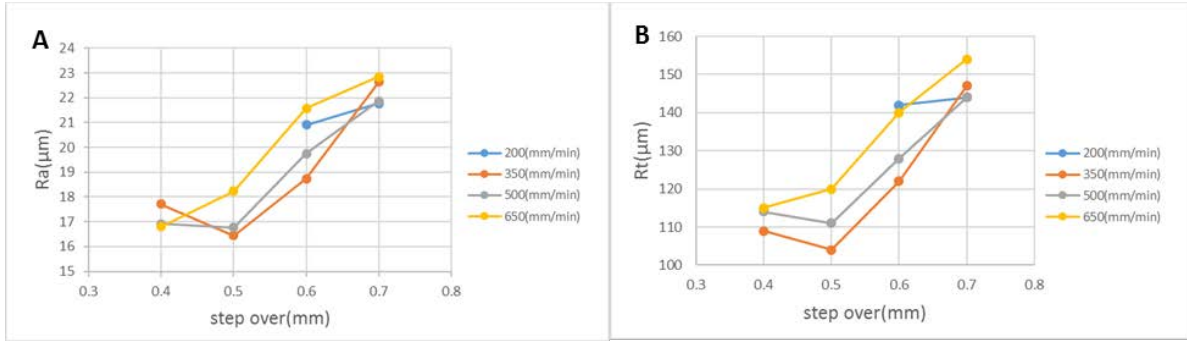


Figure 4- surface roughness (A) R_a vs. step over for different values of scanning speed, and (B) R_t vs. step over for different values of scanning speed.

Figure 5A and 5B show the results of average waviness (W_a) and total waviness (W_t), respectively, as a function of scanning speed and step over values. It was observed that for the ranges tested, step over does not have a discernable impact on W_a and W_t measurements. In other words, at a constant scanning speed, there is no noticeable relationship between step over values and waviness. However, there is a general decrease in the waviness values with increasing scanning speed.

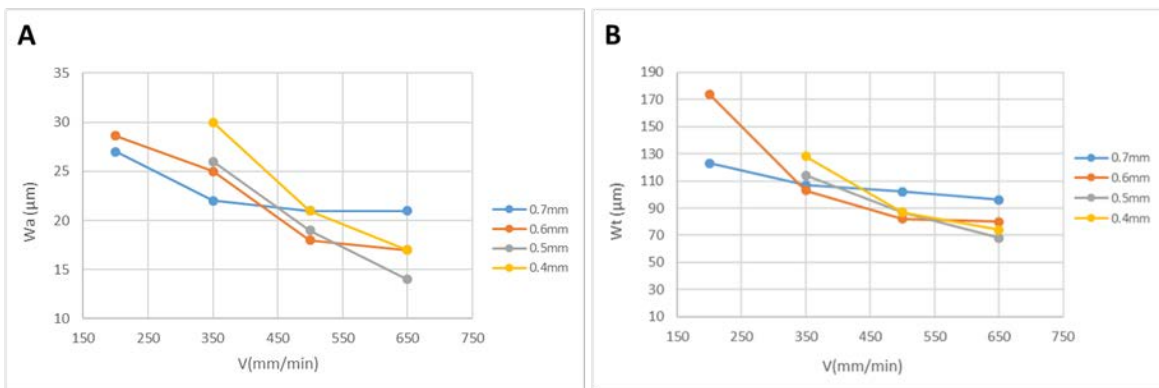


Figure 5- Waviness (A) W_a vs. scanning speed for different values of step over, and (B) W_t vs. scanning speed for different values of step over.

Figure 6 shows the surface texture of DED printed part. Surface texture consists of a meniscus and partially melted particles. Figure 6A shows the cross section of after two layers of

deposition, utilizing optical microscopy, in which the step over is 0.7 mm. This Figure clearly exhibits peaks and valleys. Figures 6B, 6C and 6D are obtained using focused variation technique. The deposited beads are clearly seen in Figure 6B. To precisely observe the peaks and valleys Figure 6C can be used. The partially melted particles can be seen in higher magnification as shown in Figure 6D.

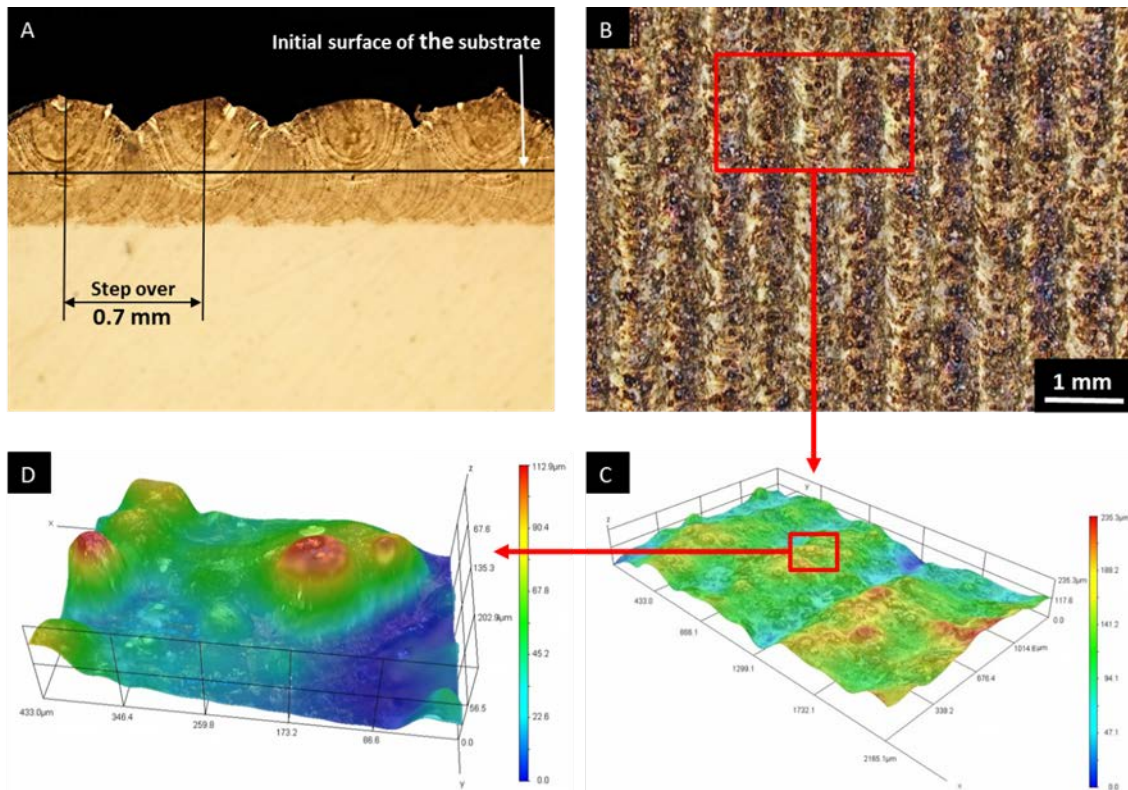


Figure 6- (6A) cross section view after two deposition layers with step over of 0.7 mm obtained using optical microscopy. Focused variation technique of (6B) top view of deposited layer texture which includes meniscus and partially melted particles, (6C) the peaks and valleys, and (6D) partially melted particles that can be seen clearly at high magnification.

Figure 7 shows the cross section of single bead produced at different scanning speeds. The geometry and shape of the single bead can be seen in this Figure. As seen in this Figure, the single bead at scanning speed of 200 mm/min has arc shape, however at scanning speed of 650

mm/min, the shape of single bead is parabolic. The study of single bead shape allows the further detailed observations of surface topology and the effect of process parameters on surface roughness and waviness. To compare geometry at different scanning speeds, the height and width of single beads are measured and shown in Figure 8. As seen, with increasing scanning speed, the values of height and width of beads decrease.

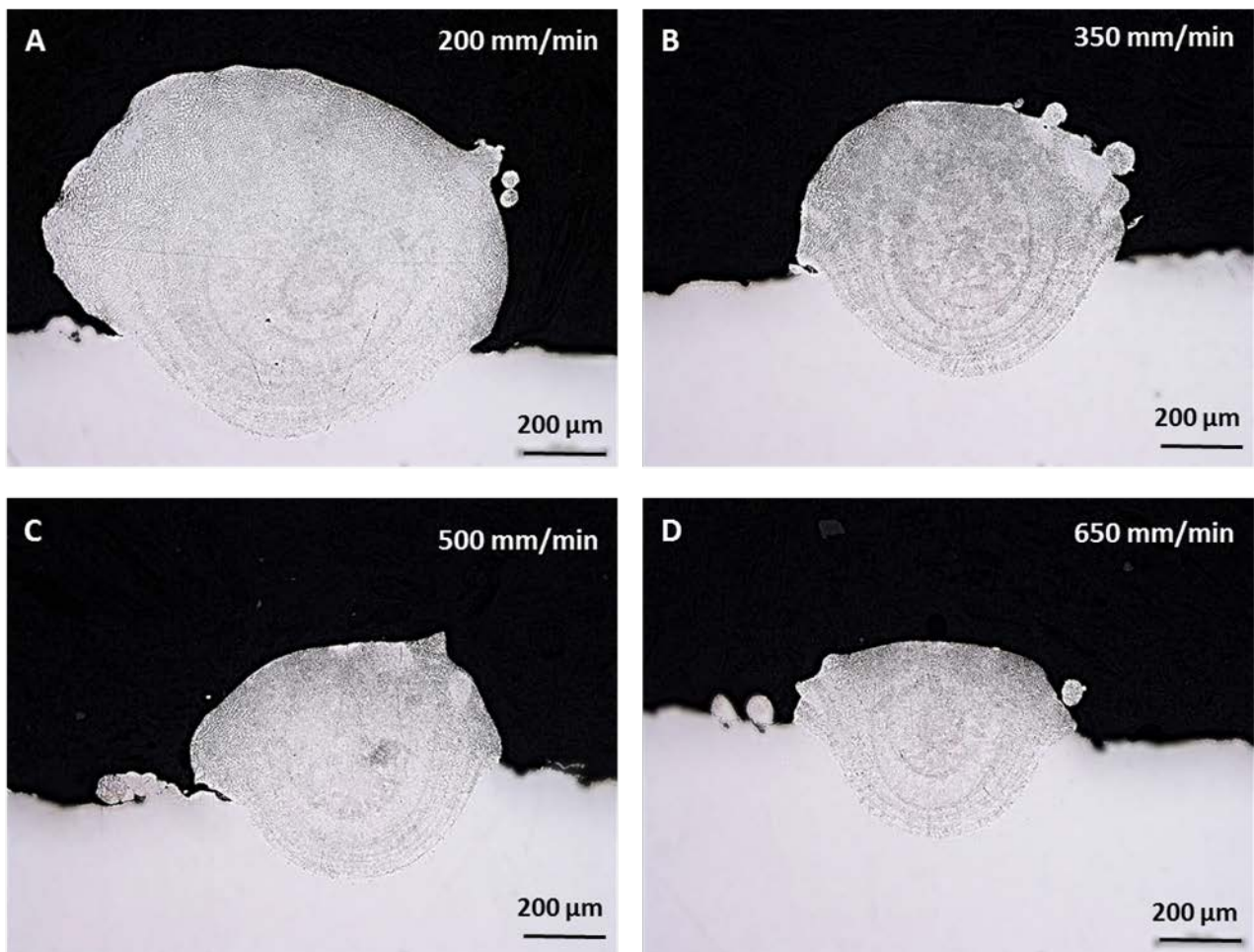


Figure 7- Optical microscopy images of the cross section of a single bead cross-section at different scanning speeds, (7A) 200 mm/min, (7B) 350 mm/min, (7C) 500 mm/min, and (7D) 650 mm/min. The scale bar in figures A to D is 200 μm .

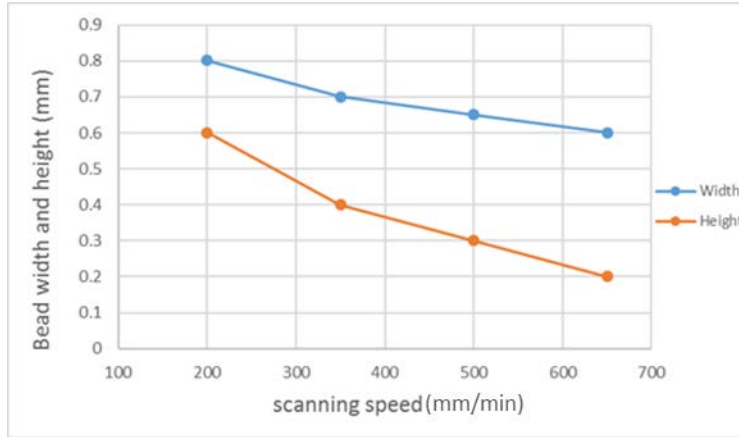


Figure 8- The measured values of width and height of the single beads at different scanning speeds, using the cross-section images shown in Figure 7.

Figure 9 shows the non-uniformity of the surface of a single bead at a scanning speed of 200 mm/min. As seen in this Figure, the geometry of single bead is not uniform along the length and the bead forms an uneven surface. This phenomenon is different from that created by a meniscus and partially melted particles. Evidence of the effect of this phenomenon on surface quality was not found in the literature; however, it might have impact on the surface texture particularly at higher overlaps.

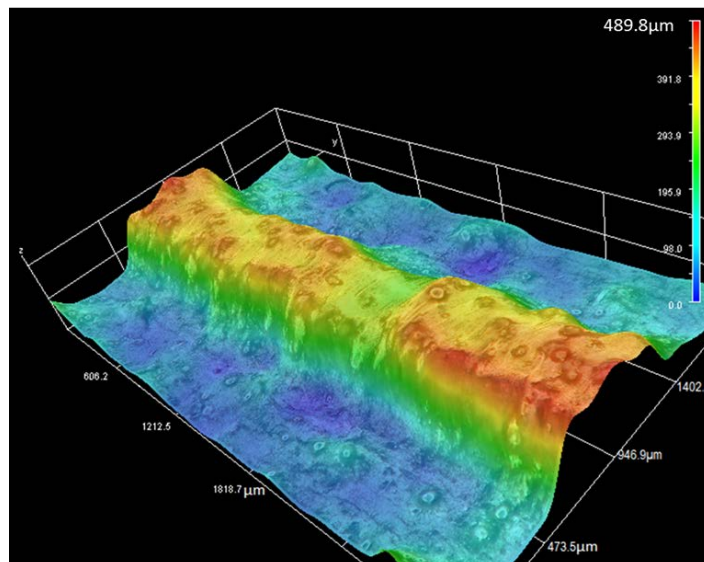


Figure 9- Non-uniformity of surface of single bead at scanning speed of 200 mm/min. It is seen that the geometry of single bead is not uniform along the length of bead.

Figure 10 compares the geometry and characteristics of two beads at a constant scanning speed of 650 mm/min and step over values increasing from 0.4 to 0.7 mm. As seen, with decreasing the step over, the second bead is formed over the first bead and the overlap increases. These observations allow us to study the effect of step over on surface roughness and waviness. Figure 11 provides cross sections for pairs of beads produced with the same step over value but with varying scanning speeds. Figure 11 shows with decreasing scanning speed, although the step over is constant, overlap increases.

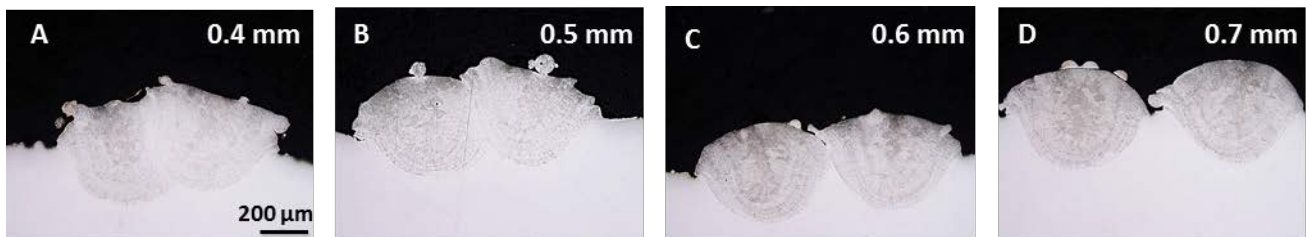


Figure 10- Microscopic images of cross-section of two beads at scanning speed of 650 mm/min and different step overs range from 0.4 to 0.7 mm. The scale bar in figures A to D is 200 μm .

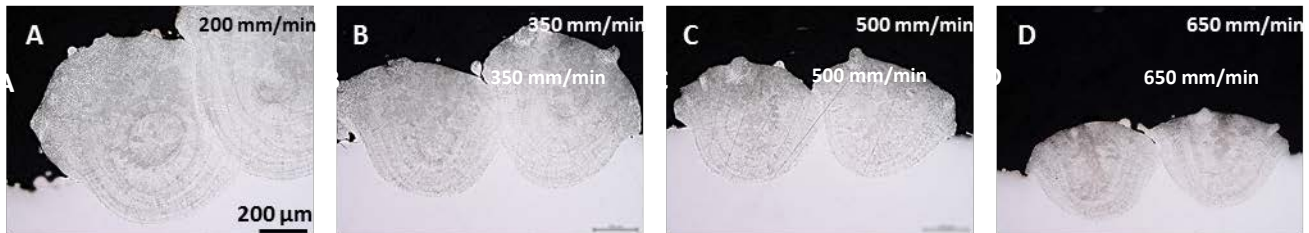


Figure 11- Microscopic images of cross-section of two beads at step over of 0.6 mm and different scanning speeds range from 200 to 650 mm/min. The scale bar in figures A to D is 200 μm .

Figure 12 shows the microstructure of different zones of the deposited layer produced with a scanning speed of 200 mm/min. In the bottom of the bead, columnar cellular substructure is seen that starts from the boundary and drags into the bead as seen in Figure 12C. In Figure 12A, the coaxial sub-grain cellular structures in the middle of the deposited layer are seen in which the microstructure is smaller. Figure 12B shows the top of the deposited layer or the free surface of

the sample. The molten pool boundary is an arc shape because of the Gaussian laser beam distribution (Figure 12D). In this Figure, the alignment and orientation of the grains are unknown. In order to determine this diffraction techniques such as electron back-scattering patterns (EBSD) could be used.

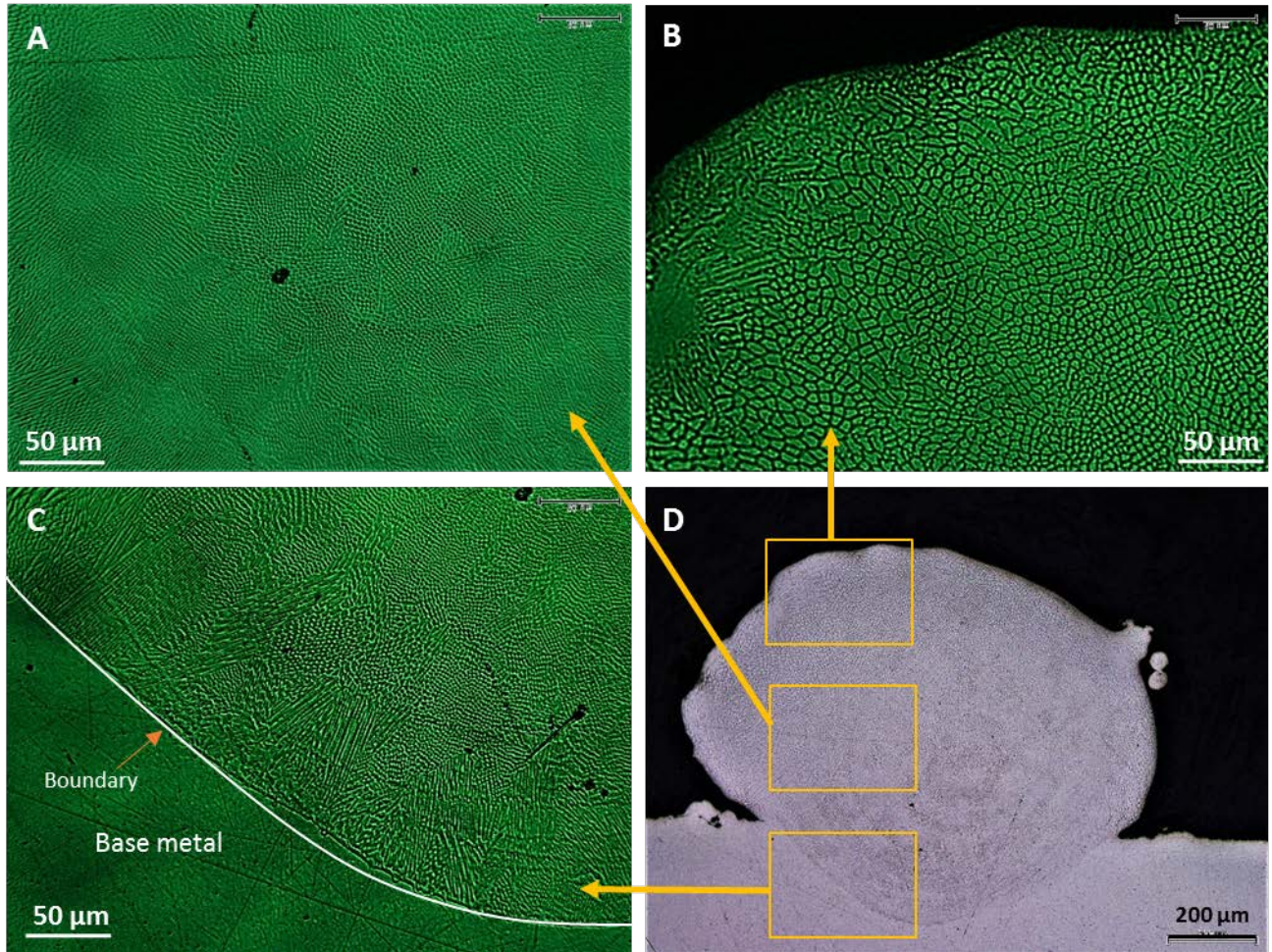


Figure 12- Optical microscopy of microstructure morphology at different regions of deposited layer at scanning speed of 200 mm/min. (12A) cellular substructure in the middle of deposited layer, (12B) Top of the deposited layer that has larger cellular substructure compared to the middle of the sample, (12C) columnar structure in the bottom of the bead. Each observed image corresponds to the position marked by the yellow box in figure 12D. The circular arc shape of molten pool boundary is seen in figure 12D.

Figure 13 shows the average sub-grain size created at different scanning speeds range from 200 to 650 mm/min. The microstructure has a significant effect on the mechanical properties

and can be controlled by the DED parameters. To measure the sub-grain size, the linear intercept method has been used [29]. As the scanning speed increased from 200 to 650 mm/min, the sub-grain size decreases from approximately 5 μm to 2 μm (Figure 13A). Figure 13B to 13E demonstrate the microstructure of the printed part at different scanning speed to visually reveal the effect of deposition rate on the substructure. In order to understand the influence of scanning speed on the surface quality, the microhardness of the second deposited layer was studied. Figure 14 compares the microhardness as a function of scanning speed. This Figure shows that the microhardness increases from 155 HV at 200 mm/min to 180 HV at 650 mm/min. As seen in Figures 13 and 14, microhardness increases with decreasing sub-grain size. Generally, small microstructure improves the overall mechanical properties of the material.

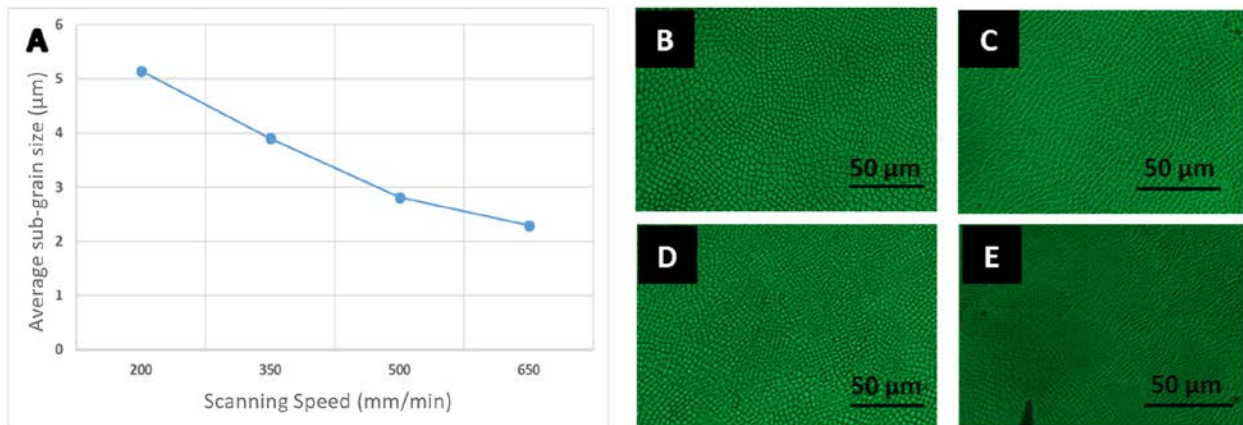


Figure 13- (A) Average sub-grain size at different scanning speeds; The optical microscopy images of the printed part at (B) 200, (C) 350, (D) 500, and (E) 650 mm/min.

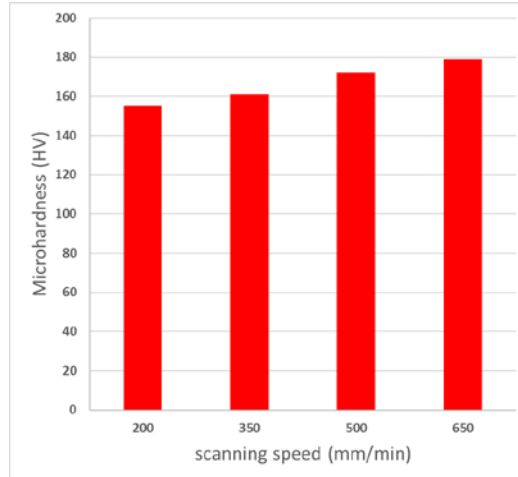


Figure 14- Microhardness values of the second layer of deposited part at different scanning speeds that increase continuously with scanning speed from 155 HV at 200 mm/min to 180 HV at 650 mm/min.

Table 3 compares the surface roughness of samples before and after laser remelting. The laser remelting had a larger reduction in the smaller scale roughness than in the longer scale waviness, as expected. Laser remelting of the sample with a scanning speed of 500 mm/min and a step over of 0.6 mm produced the largest decrease in surface roughness. Overall, the percent decrease in R_t values is more than the R_a values. This shows that remelting a sample greatly reduces the peak values and creates a more uniform surface profile. Figure 15 shows the visual appearance of the samples before and after laser remelting. The optical microscopy of the cross section of laser remelted sample at scanning speed of 500 mm/min and step over of 0.4 mm is shown in Figure 16 and the roughness and waviness profiles of this sample, obtained from profilometry measurement, is shown in Figure 17A and 17B, respectively. As seen, laser remelting technique leads to a reduction in surface roughness and waviness, and general improvement in the surface quality.

Table 3- comparison of surface roughness and waviness in laser remelted conditions.

Sample	V (mm/min)	D (mm)	Before Laser Remelt				After Laser Remelt				% decrease			
			R _a (μm)	R _t (μm)	W _a (μm)	W _t (μm)	R _a (μm)	R _t (μm)	W _a (μm)	W _t (μm)	R _a	R _t	W _a	W _t
1	200	0.7	21	144	27	132	3	14	21	108	85	90	20	18
2	350	0.7	22	147	22	107	5	29	14	68	77	80	37	36
3	500	0.7	21	144	21	102	5	30	11	47	75	79	49	54
4	500	0.6	19	128	18	82	1	19	9	37	91	85	52	55
5	500	0.4	16	114	19	87	2	13	12	50	88	91	38	43

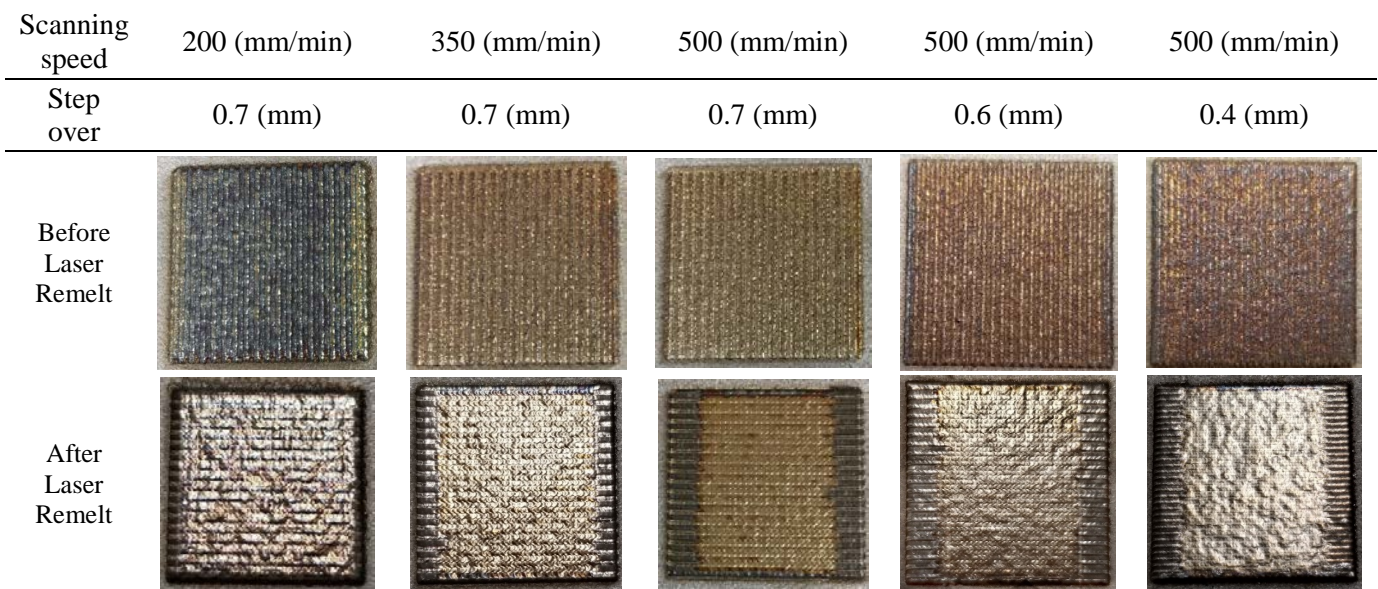


Figure 15- The visual appearance of the surface quality of samples before and after laser remelting. The roughness and waviness of the surfaces decrease after laser remelting.

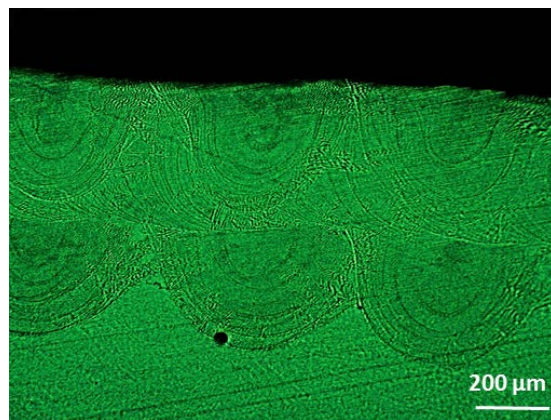


Figure 16- The optical microscopy image of cross section of the sample at scanning speed of 500 mm/min and step over of 0.4 mm after laser remelting. The laser remelting clearly decreases the surface roughness and waviness, makes the surface smoother and improves the surface quality.

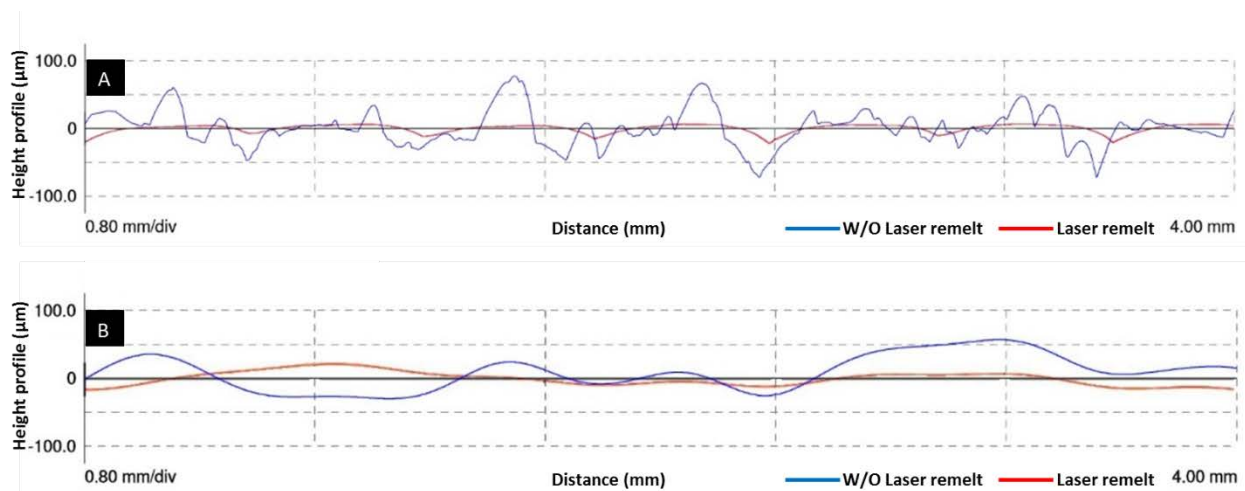


Figure 17- The profilometry measurements of (17A) surface roughness, and (17B) surface waviness before laser remelt (blue line), and after laser remelt (red line) of the sample at scanning speed of 500 mm/min and step over of 0.4 mm. The red lines are smoother than the blue lines which means that the surface roughness and waviness considerably decrease after the laser remelting.

Discussion

Effect of step over

The width of a single bead (W) is expected to remain constant as long as the DED parameters are constant. Equation 1 shows that as long as W is constant, with an increasing step over, the overlap ratio (OR) decreases. As reported in previous studies on simulation of the bead geometry, it is expected that with decreasing overlap ratio the waviness increases [15]. Although, in these models, the bead geometry is assumed to be uniform along the length of the bead. In this work, it has been observed that the bead is not uniform geometry along the length (Figure 9). There are some reasons that cause the non-uniformity of the bead along the printing direction, including process parameters instabilities, systematic error and roughness and waviness of the substrate. In a sample with non-zero overlap, the texture of the surface depends on the uniformity of the beads. In the case of overlapping deposition, the laser beam remelts some part of the previous bead. Therefore, the deposited material consists of this remelted material and the molten powder that is

added to the melt pool. Due to non-uniformity, the distribution of the remelted material is not the same along the length of the bead because there is less material at some regions of the bead. Consequently, the non-uniformity pattern is followed by the new beads. Hence, the non-uniformity has a cumulative effect, leading to an unevenness of the printed surface.

Surface roughness of parts manufactured by DED are mainly affected by partially melted particles. The size, shape and quantity of these partially melted particles depend on DED process parameters. With decreasing step over, the more part of the previous bead is remelted, so the more partially melted particles which are remained over the previous bead, have chance to be remelted that leads to a decrease in the surface roughness.

Effect of scanning speed

With varying scanning speed at a constant step over, two geometry parameters affect the waviness: bead width and bead height. With increasing scanning speed, both bead width and bead height decrease. According to Eq. 2, with decreasing the bead width, at constant step over, the overlap decreases that leads to an increase in waviness. On the other hand, the effect of the scanning speed on bead height is more notable (Figure 7). Thus, since the decrease in bead height is dominant, the waviness decreases with increasing scanning speed.

Microstructure and Microhardness

Understanding the correlation between process parameters and microstructure allows us to adjust the parameters to achieve the best quality of surface texture, microstructure and mechanical properties of the printed part. The microstructure is affected by kinetic of mass transfer (R) and the ratio of thermal gradient (G). The ratio of thermal gradient and mass transfer (G/R) determines the microstructure morphology of a single bead [30,31]. Optical microscopy images reveal that at

the bottom of melt pool, the columnar cellular substructures are formed and drag into the bead because in the bottom of the melt pool the thermal gradient is higher than the melt pool surface. At the bottom of the melt pool, the ratio of G/R satisfies the columnar solidification conditions. In addition, at the very top of the melt pool, coarse equiaxed sub-grains are observed due to a lower cooling rate. In the middle of the melt pool which is defined as the regions near the very top, the fine equiaxed sub-grains are found, because the cooling rate of this region of the melt pool is higher than the very top region. With increasing scanning speed, less material is deposited, increasing the cooling rate and leading to a finer microstructure. The finer microstructure is contributed to higher microhardness values as predicted by Hall-Petch equation [32]. This equation indicates that for finer microstructure the material becomes harder.

Laser remelting

The results of profilometry show that laser remelting after layer deposition has obtained a smoother surface. Laser remelting can serve as an inexpensive technique to reduce the surface roughness and waviness and allow us to eliminate the need for machining processes in some specific applications. The laser beam moves over the surface with a predefined scanning speed, so there is a chance for some of the partially melted particles to be melted and which will reduce the surface roughness. In addition, the reduction of surface waviness has been observed after the laser remelting process because of the surface tension of the molten material. During laser remelting, a layer of material that is being melted superficially is able to relocate easily and move on the surface, thus these molten materials can flow into the cavities that generally lead to a significant decrease in roughness and waviness. This technique is an ideal method for

achieving a smoother surface texture and meeting surface characteristic specifications that are required for specific applications.

Conclusion

In this work, a specific focus has been put on surface finish of 316L stainless steel manufactured by direct energy deposition. The effect of scanning speed, step over and laser remelting on surface roughness and surface waviness of the DED parts have been investigated. The laser power was kept at 300 W. This work represents for the first time that the geometry of the printed surface is not uniform along the length. The authors defined this phenomenon as non-uniformity. It was demonstrated that with decreasing step over, the effect of non-uniformity on the overall surface texture becomes remarkable. The surface waviness mainly depends on bead geometry. When step over varies, it was found that two factors affect waviness: overlap ratio and non-uniformity. At scanning speeds of 200 mm/min and 350 mm/min, with increasing step over, the effect of uniformity is dominant and waviness increases. At a constant step over, with varying of scanning speed, bead geometry changes that eventually affects the surface waviness. The surface roughness of DED parts are clearly dependent on the partially melted particles remaining agglomerated at the metal surface. With decreasing step over, the more partially melted particles are remelted, and surface roughness decreases. Moreover, the microstructure and mechanical properties of printed part have been investigated in this study. The investigations revealed that the microstructure and microhardness are affected by DED process parameters particularly scanning speed. It was determined that the morphology transition from the bottom to the top region of a single bead based on the ratio of thermal gradient and mass transfer (G/R). The optical microscopy images showed that with increasing scanning speed, the cooling rate increases that leads to a finer

microstructure. Also, the measurements indicated that the finer microstructure is contributed to higher microhardness values. Furthermore, it has been observed that the surface roughness and surface waviness of the samples after laser remelting significantly decrease. Overall, this work demonstrates that the right combinations of DED processing parameters along with using laser remelting in order to achieve a better surface finish will prevent the need for secondary finishing operation and decrease the cost of manufacturing.

Acknowledgements

ABK, FP and IR acknowledge financial support from Iowa State University. We also thank Dr. Hantang Qin from Department of Industrial and Manufacturing Systems Engineering, Iowa State University for providing access to focused variation equipment.

References

- [1] Peyre P, Aubry P, Fabbro R, Neveu R, Longuet A. Analytical and numerical modelling of the direct metal deposition laser process. *J Phys Appl Phys* 2008;41:025403. doi:10.1088/0022-3727/41/2/025403.
- [2] Mahamood RM, Akinlabi ET, Shukla M, Pityana S. Revolutionary additive manufacturing: an overview 2014.
- [3] Song J, Deng Q, Chen C, Hu D, Li Y. Rebuilding of metal components with laser cladding forming. *Appl Surf Sci* 2006;252:7934–40. doi:10.1016/j.apsusc.2005.10.025.
- [4] Mahamood RM. Laser Basics and Laser Material Interactions. In: Mahamood RM, editor. *Laser Met. Depos. Process Met. Alloys Compos. Mater.*, Cham: Springer International Publishing; 2018, p. 11–35. doi:10.1007/978-3-319-64985-6_2.
- [5] Rombouts M, Maes G, Hendrix W, Delarbre E, Motmans F. Surface finish after laser metal deposition. *Phys Procedia* 2013;41:810–4.
- [6] Peyre P, Gharbi M, Gorny C, Carin M, Morville S, Carron D, et al. Surface Finish Issues after Direct Metal Deposition. *Mater Sci Forum* 2012. doi:10.4028/www.scientific.net/MSF.706-709.228.
- [7] Shamsaei N, Yadollahi A, Bian L, Thompson SM. An overview of Direct Laser Deposition for additive manufacturing; Part II: Mechanical behavior, process parameter optimization and control.

- Addit Manuf 2015;8:12–35. doi:10.1016/j.addma.2015.07.002.
- [8] Gharbi M, Peyre P, Gorny C, Carin M, Morville S, Le Masson P, et al. Influence of various process conditions on surface finishes induced by the direct metal deposition laser technique on a Ti–6Al–4V alloy. *J Mater Process Technol* 2013;213:791–800. doi:10.1016/j.jmatprotec.2012.11.015.
- [9] Mahamood RM, Akinlabi ET. Effect of scanning speed and gas flow rate on surface roughness of LMD titanium-alloy 2016.
- [10] de Oliveira U, Ocelík V, De Hosson JTM. Analysis of coaxial laser cladding processing conditions. *Surf Coat Technol* 2005;197:127–36. doi:10.1016/j.surfcoat.2004.06.029.
- [11] Ocelík V, de Oliveira U, de Boer M, de Hosson JTM. Thick Co-based coating on cast iron by side laser cladding: Analysis of processing conditions and coating properties. *Surf Coat Technol* 2007;201:5875–83. doi:10.1016/j.surfcoat.2006.10.044.
- [12] Toyserkani E, Khajepour A, Corbin S. 3-D finite element modeling of laser cladding by powder injection: effects of laser pulse shaping on the process. *Opt Lasers Eng* 2004;41:849–67.
- [13] Cao Y, Zhu S, Liang X, Wang W. Overlapping model of beads and curve fitting of bead section for rapid manufacturing by robotic MAG welding process. *Robot Comput-Integr Manuf* 2011;27:641–5. doi:10.1016/j.rcim.2010.11.002.
- [14] Li Y, Ma J. Study on overlapping in the laser cladding process. *Surf Coat Technol* 1997;90:1–5. doi:10.1016/S0257-8972(96)03022-8.
- [15] Ocelík V, Nenadl O, Palavra A, De Hosson JTM. On the geometry of coating layers formed by overlap. *Surf Coat Technol* 2014;242:54–61. doi:10.1016/j.surfcoat.2014.01.018.
- [16] Nenadl O, Ocelík V, Palavra A, Hosson JTMD. The Prediction of Coating Geometry from Main Processing Parameters in Laser Cladding. *Phys Procedia* 2014;56:220–7. doi:10.1016/j.phpro.2014.08.166.
- [17] Lin J. A simple model of powder catchment in coaxial laser cladding. *Opt Laser Technol* 1999;31:233–8. doi:10.1016/S0030-3992(99)00046-8.
- [18] Zekovic S, Dwivedi R, Kovacevic R. Numerical simulation and experimental investigation of gas–powder flow from radially symmetrical nozzles in laser-based direct metal deposition. *Int J Mach Tools Manuf* 2007;47:112–23. doi:10.1016/j.ijmachtools.2006.02.004.
- [19] Tan H, Hu G, Zhang F, Fan W, Hou W, Huang W. Formation mechanism of adhering powder and improvement of the surface quality during laser solid forming. *Int J Adv Manuf Technol* 2016;86:1329–38. doi:10.1007/s00170-015-8269-6.
- [20] Rosa B, Brient A, Samper S, Hascoët J-Y. Influence of additive laser manufacturing parameters on surface using density of partially melted particles. *Surf Topogr Metrol Prop* 2016;4:045002. doi:10.1088/2051-672X/4/4/045002.
- [21] Temmler A, Willenborg E, Wissenbach K. Laser polishing. *Laser Appl. Microelectron. Optoelectron. Manuf. LAMOM XVII*, vol. 8243, International Society for Optics and Photonics; 2012, p. 82430W. doi:10.1117/12.906001.

- [22]Mahamood RM. Processing Parameters in Laser Metal Deposition Process. In: Mahamood RM, editor. *Laser Met. Depos. Process Met. Alloys Compos. Mater.*, Cham: Springer International Publishing; 2018, p. 61–92. doi:10.1007/978-3-319-64985-6_4.
- [23]Wu X, Liang J, Mei J, Mitchell C, Goodwin PS, Voice W. Microstructures of laser-deposited Ti–6Al–4V. *Mater Des* 2004;25:137–44. doi:10.1016/j.matdes.2003.09.009.
- [24]Senthilkumaran K, Pandey PM, Rao PVM. Influence of building strategies on the accuracy of parts in selective laser sintering. *Mater Des* 2009;30:2946–54. doi:10.1016/j.matdes.2009.01.009.
- [25]Mahamood RM, Akinlabi ET, Shukla M, Pityana S. Characterizing the Effect of Laser Power Density on Microstructure, Microhardness, and Surface Finish of Laser Deposited Titanium Alloy. *J Manuf Sci Eng* 2013;135:064502-064502–4. doi:10.1115/1.4025737.
- [26]Yakout M, Elbestawi MA, Veldhuis SC. On the characterization of stainless steel 316L parts produced by selective laser melting. *Int J Adv Manuf Technol* 2018;95:1953–74. doi:10.1007/s00170-017-1303-0.
- [27]ASM Handbook Volume 9: Metallography and Microstructures - ASM International n.d. https://www.asminternational.org/search/-/journal_content/56/10192/06044G/PUBLICATION (accessed November 20, 2018).
- [28]E04 Committee. Test Method for Microindentation Hardness of Materials. ASTM International; n.d. doi:10.1520/E0384-17.
- [29]E04 Committee. Test Methods for Determining Average Grain Size. ASTM International; n.d. doi:10.1520/E0112-13.
- [30]Yan F, Xiong W, Faierson EJ. Grain Structure Control of Additively Manufactured Metallic Materials. *Materials* 2017;10:1260. doi:10.3390/ma10111260.
- [31]Li J, Deng D, Hou X, Wang X, Ma G, Wu D, et al. Microstructure and performance optimisation of stainless steel formed by laser additive manufacturing. *Mater Sci Technol* 2016;32:1223–30. doi:10.1080/02670836.2015.1114774.
- [32]Liu MY, Shi B, Wang C, Ji SK, Cai X, Song HW. Normal Hall–Petch behavior of mild steel with submicron grains. *Mater Lett* 2003;57:2798–802. doi:10.1016/S0167-577X(02)01377-0.

CHAPTER 3. A NEW TEST METHOD FOR EVALUATING INTERFACIAL BONDING STRENGTH FOR METAL ADDITIVE MANUFACTURING

Ali Baghersaghchi Khorasani^{1*}, Frank Peters¹, Scott Chumbley²

1. Department of Industrial and Manufacturing Systems Engineering, Iowa State University, 3004 Black Engineering, Ames, IA 50011
2. Department of Materials Science and Engineering, Iowa State University, 2240 Hoover, Ames, IA 50011

Introduction

Direct energy deposition (DED) uses a system of a laser beam and powder delivery nozzles that converge at the surface of the material creating a melt pool to produce near net shape metal parts. This system follows a path to create a 2D layer of the part; this process is repeated and rasters across the surfaces line by line until the desired geometry is created [1], [2]. There are a broad range of applications for this manufacturing process, including remanufacturing and repairing applications [3], design flexibility for a part, and building part with functionally graded materials that makes DED become favorable in some industries such as aerospace and biomedical [4]. While additive manufacturing has many advantages, it is often not the most economical solution for some part features. Hybrid solutions which use conventional manufacturing processes for producing the large geometrical simple segment of the part, followed by AM for adding complex feature to this segment [5] is an increasingly viable solution. Hybrid manufacturing (HM) combines additive manufacturing (AM) with conventional manufacturing processes, such as machining [6], [7]. The characterization of mechanical properties and interfacial bonding strength of hybrid manufactured parts becomes important. Applications of AM and HM parts in critical structures leads to the necessity of a comprehensive understanding of the microstructure and mechanical properties of these parts,

including fracture behavior, fatigue and crack growth [8], [9]. Generally, mechanical properties of a hybrid manufactured part depends on mechanical properties and microstructure of the substrate/deposited interface [10].

A review of the literature and standards did not reveal a universally accepted testing method for measuring the interfacial bonding strength of hybrid manufactured parts. There are a number of researchers that put efforts to evaluate the interfacial strength using a variety of existing methods. Tensile testing was commonly used for characterizing the HM parts in some studies. For example, Zhai et al. [9] studied the mechanical properties of Inconel and Ti-6Al-4V alloys manufactured by DED. For testing interface performance, they used a standard tensile test (ASTM E8) with 101.6mm total length and 25.4 mm gauge length. The samples manufactured such that half of the sample is substrate and another half is deposited material; the interface of substrate and deposited is placed in the middle of the gauge. The Ti-6Al-4V samples with different test conditions fractured in the deposited part that shows the good interface strength. Inconel 718 deposited with low power fractured in the deposited part, whereas samples deposited with high power fractured in the substrate which show adequate interface strength. Shi et al. [10] investigated the mechanical properties of hybrid manufacturing of Ti-6Al-4V. Their hybrid manufacturing method includes wire arc additive manufacturing (WAAM) on a selective laser melting part. For measuring the mechanical properties, three different tensile test samples are extracted, using wire electrical discharge machining. First group are manufactured by WAAM. Half of the second and third groups of test samples are manufactured by WAAM and the other halves are manufactured by SLM with different deposition direction. Tensile tests samples have 34.29 mm overall length and 10.16 mm gauge length as shown in Figure 1A. Thereafter, tensile strength, yield strength and elongation of these three groups are compared to each other. In these

samples they indicated three different zones consist of WAAM zone, interface zone and SLM zone. All samples fractured in WAAM zone which shows the good metallurgical bonding in interface zone, better than WAAM zone (Figure 1B).

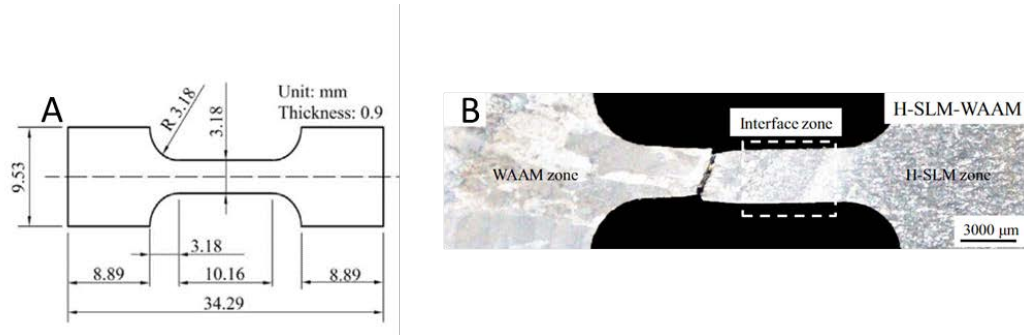


Figure 1- Hybrid-processed tensile testing (A) sample geometry , (B) after failure [10].

Zhang et al. [11] made TC11/Ti2AlNb dual alloy with DED and investigated the tensile properties of the TC11/Ti2AlNb interface. The tensile test specimens are prepared using wire cutting machine and the proper surface finish is achieved by 600 and 1000 grit sand paper. The test specimens composed of half TC11 and half Ti2AlNb with the interface in the gauge length with an overall length of 40 mm and gauge length of 14 mm. Tensile testing was carried out at room temperature and at 650 °C with the tensile rate of 0.5 mm/min. Fracture occurs in TC11 alloy side and Ti2AlNb alloy side at room temperature and 650 °C, respectively. In both cases, the interface was not the area of fracture. .

Dongare et al. [12] argued that the conventional ASTM E-8 tensile test is an insufficient method for characterizing interfacial bonding strength of additive manufactured parts in some cases because the production of large samples is economically unreasonable, time consuming, or even it is not possible because of the geometry and process limitations. In addition, they claim that smaller tensile samples are more suitable for measuring location-dependent properties.

Therefore, tensile test method with miniature specimens with overall length of 17.739 mm and gauge length of 3.3 mm is defined and procedures for testing set-up and analysis is covered. It should be considered that in the case of large grain size this test reports higher values for yield and ultimate tensile strength.

Because of two reasons, the tensile test is not an appropriate approach for determining the strength of interface in HM parts. The tensile test specimen is taken such that half of the specimen is the substrate (wrought material), and half is the deposited material. Therefore, according to the ASTM E8 geometry, it is necessary to deposit at least 50.8 mm on top of the substrate. Printing a part with the mentioned size is not only expensive and time consuming, but also technically challenging. Second, in the case that fracture of additive or hybrid manufactured part does not take place in the interface, the tensile test is not able to measure the interfacial bonding strength; only a minimum value for the interface can be obtained. Therefore, tensile test is not a reliable method for determining the interfacial bonding strength.

Consequently, an alternative to tensile testing is warranted for studying the interfacial bonding strength. Paul et al. [13] investigated the strength of interface of WC-12 Co cladded on low carbon steel. They claimed that the tensile adhesion test can be used for measuring the adhesion strength of coating. In tensile adhesion test (ASTM C633-79 [14]) a jig is attached to the surface, using a polymer based adhesive. However, this method is limited to the adhesive strength. Therefore, they used another test method that is called the adhesion cohesion test. Test samples include a disk (20 mm diameter and 6.25 mm thickness) as the substrate and 2.5 mm thick clad deposited using laser. Then, using a universal testing machine, they put a load on the clad part and determine the interface strength as shown in Figure 2. For most samples, the fracture occurred in the interface area and in some samples partial fracture took place in both the

cladding part and interface zone. Thus, this testing method is not reliable enough for measuring the interfacial strength of DED parts.

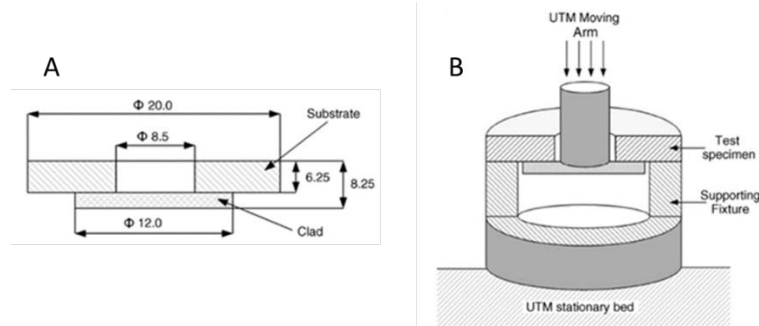


Figure 2- The adhesion-cohesion test sample (A) and set-up (B) [13].

Xu et al. [15] investigated the effect of laser cladding parameters on interfacial bonding shear strength. They used samples that were a cylindrical substrate of carbon steel C45 with diameter of 20 mm and length of 100 mm for which cladding is added circumferentially at a thickness of 2 mm radially and 2 mm in height. To measure the interface shear strength, the specimen is cut using wire electrical discharging machine and embedded in a fixture with 20 mm diameter hole placed under a compressive load. For nickel-based sample, the cladding was fell of completely, however the sample with an iron based cladding was partially fractured. The following equation shows the calculated bonding shear strength,

$$\tau = \frac{F_p}{\pi D h} \quad (1)$$

where F_p is maximum applied load, D is substrate diameter, and h is the clad height. The result shows that the material breaks apart from the substrate.

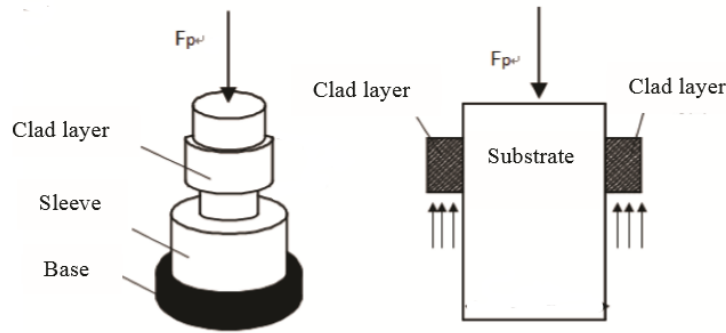


Figure 3- Schematic illustration of shear test designed and used in Ref [15].

Wei et al. [16] investigated interfacial fracture of laser clad maraging steel. Cylindrical T-shaped test specimens were prepared using machining process as shown in Figure 4. To measure the interfacial bonding strength, an additional machining was used to create a circular-arc shape at the interface as shown in Figure 4B. All samples fractured in the interfacial plane. Because the notch causes stress concentration, in peripheral of the interfacial plane, the maximum stress in this area leads to plastic deformation. With increasing load, the plastic deformation extended inward and the interfacial cracks initiate and propagate along the interface. It is reported that in case of good plasticity, the notch effect can be ignored.

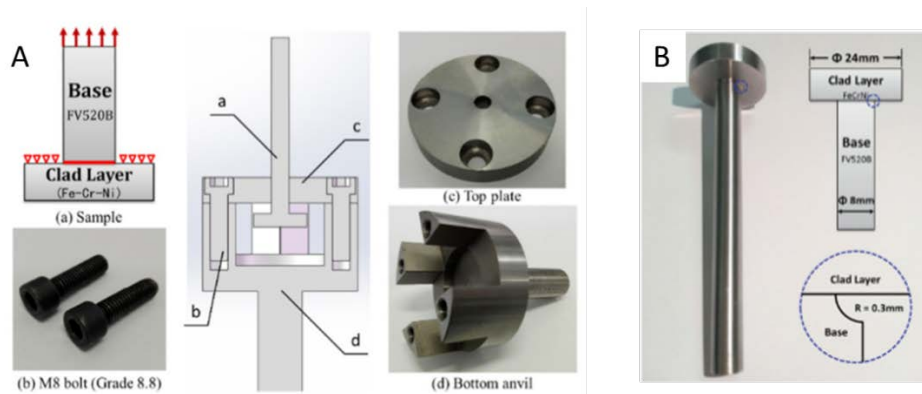


Figure 4- (A) Fixture set-up and assembly used for tensile test, (B) The dimensions of testing sample [16].

Among the abovementioned testing methods, a reliable method was not found for measuring the interfacial bonding strength of hybrid manufactured parts because these testing methods fail to prove that the fracture occurs completely in the interface. The authors first conducted preliminary experiments to measure interfacial bonding strength, using tensile shear test which is a testing method that is widely used for clad plates [17]. However, the results obtained from tensile shear test, which are presented in detail in the following sections, are not strongly consistent. Hence, in the present work, a new testing methodology is proposed to measure the bonding strength between the substrate and the deposited part in hybrid manufacturing. This testing method is called the block shear test. Theoretical and numerical analysis have been undertaken to better understand the stress distribution under this test condition. The test results and fractography observations demonstrate that the developed testing method is reliable and provides with information about bonding strength.

Theoretical Description

Mechanical testing aims to define mechanical properties of materials that enables characterization of the material properties regardless of the part geometry. There are many testing methods for determining different mechanical properties of materials including tensile, impact, fatigue, creep, hardness, fracture toughness and non-destructive testing. For determining the interfacial bonding strength, tensile test is a basic test method that can provide us with the amount of stress that causes interface to fail and start plastic deformation and also ultimate tensile strength. As discussed above, tensile test is not a reliable method for characterizing the interface of hybrid manufactured parts because the failure can occur at any location along the gauge length, and there is no warranty that it occurs at the interfacial bonding. An alternative to tensile test is the use of a shear test to evaluate the interface mechanical characteristics such as

shear stress, shear strain, and shear modulus. While the applied force in compression and tensile tests is perpendicular to the relevant plane, in shear tests, the force and the contact surface are parallel which leads to sliding failure. Since the material behavior is different in tension and compression versus shear tests, the results lead to different strength values.

Figure 5 shows a general schematic action of shear force. As it is difficult to determine the accurate stress distribution, the assumption of uniformly stress distribution is reasonable and conventional. Based on this assumption the average shear stress can be calculated, where A is the area of the plane that force is applied to [18],

$$\tau = \frac{P}{A} \quad (2)$$

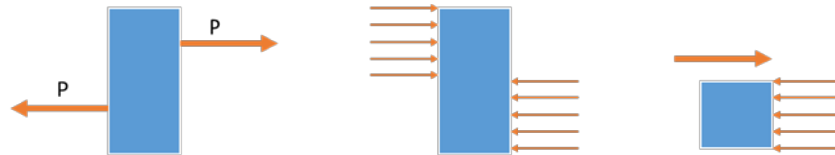


Figure 5- General schematic diagram of shear force.

Figure 6A shows a cantilever beam with a cross section shown in Figure 6B. The theory and equations developed in this section are derived from engineering mechanics texts [18], [19]. As shown in the Figure 6, in the distance of “L” from the interface, force “P” is applied parallel to the interface plane. Because it is in a static situation, the sum of the momentum and forces should be zero in any direction. Therefore, the average shear stress at the interface is given by,

$$\tau = \frac{P}{A} \quad (3)$$

where A is the area of the interface.

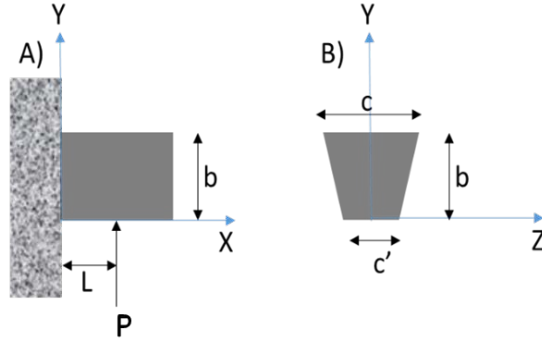


Figure 6- (A) Schematic of a cantilever beam under the applied load P; (B) Cross-section view of the cantilever beam.

Force P also causes bending, which results in a bending moment at interface. This bending moment causes a tensile stress in the lower and a compressive stress at the upper part of the interface [20],

$$\sigma(y) = \sigma_0(y_0 - y) \quad (4)$$

$$\sigma_0 = \frac{36(c' + c)P_f L}{b^3(c'^2 + 4cc' + c^2)} \quad (5)$$

where y_0 indicates the neutral axis location. The tensile stress at any Y position could be calculated if the value of y_0 and σ_0 are inserted into Equation 4. The maximum tensile stress is located at $y = b$. Because failure occurs in the location with higher stress, if failure occurs due to tensile stress it should be at $y=b$; so, the failure load is expressed as [20],

$$\sigma_f = \frac{12(2c' + c)P_f L}{b^2(c'^2 + 4cc' + c^2)} \quad (6)$$

This calculated stress represents tensile bond strength. On the other hand, Equation 7 represents shear bond strength as,

$$\tau_f = \frac{P_f}{A} \quad (7)$$

The bonding strength of the interface can be tensile, shear or combination of tensile and shear.

The initiation of failure and therefore the bonding strength depends on the type of the stress (shear or tensile). Thus, the load that causes failure for tensile and shear modes can be calculated as Equations 8 and 9, respectively [20],

$$P_f = \frac{b^2(c'^2 + 4cc' + c^2)\sigma_f}{12(2c' + c)L} \quad (8)$$

$$P_f = \tau_f A \quad (9)$$

In this study the samples have a rectangular interface cross section in which $y_0 = b/2$ and $c = c'$, as shown in Figure 7. Therefore, according to the Equation 11, stress distribution in X direction should be point symmetric in y_0 as shown in Figure 8. Thus,

$$\sigma_0 = \frac{12P_\sigma L}{b^3 c} \quad (10)$$

$$\sigma(y) = \frac{12P_\sigma L}{b^3 c} \left(\frac{b}{2} - y \right) \quad (11)$$

$$\sigma_{max} = \sigma(0) = \frac{6P_\sigma L}{b^2 c} \quad (12)$$

$$\tau_{max} = \frac{P_\tau}{bc} \quad (13)$$

In the case that the loading causes the failure in tensile mode, Equation 14 can be used to relate the applied load and the yield strength of the sample as,

$$P_\sigma = \frac{b^2 c \sigma_y}{6L} \quad (14)$$

However, when the failure occurs in the shear mode, the relationship between the applied load and the shear strength can be expressed as,

$$P_\tau = \tau_{max} bc \quad (15)$$

Thus, in the designed specimen that fracture occurs due to shear stress, the load that is required for shear failure should be less than that of tensile one so,

$$P_{\tau} < P_{\sigma} \quad (16)$$

$$\tau_{max}bc < \frac{b^2c\sigma_y}{6L} \quad (17)$$

Based on Von-Mises criterion, at the onset of yielding, the magnitude of the shear yield stress in pure shear is $(\sqrt{3})$ times lower than the tensile yield stress in the case of simple tension.

$$\sigma_y = \sqrt{3\tau_{max}} \quad (18)$$

$$\tau_{max}bc < \frac{b^2c\sqrt{3}\tau_{max}}{6L} \quad (19)$$

$$\tau_{max}bc < \frac{b^2c\sqrt{3}\tau_{max}}{6L} \quad (20)$$

$$L < \frac{b}{2\sqrt{3}} \quad (21)$$

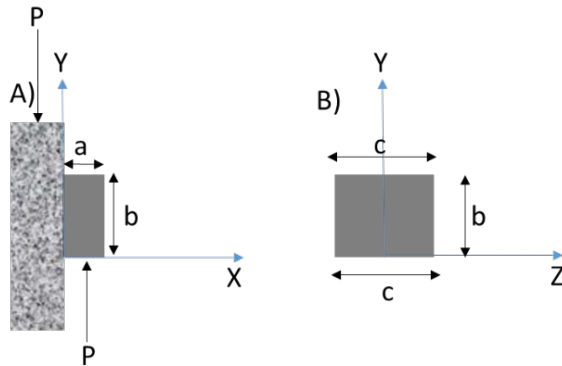


Figure 7- schematic of the shear test sample. A) Side view. B) Cross-section view of the deposited part.

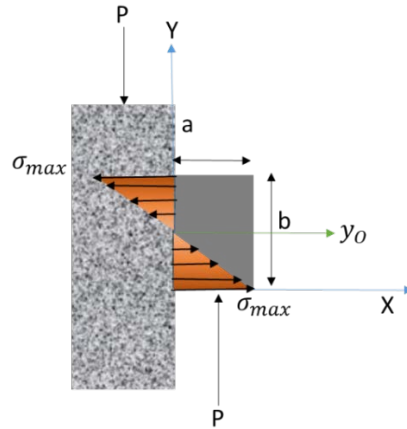


Figure 8- schematic of stress distribution in x-direction.

In order to calculate L , the force distribution under the protrusion should be defined. If evenly distributed, L is equal to $a/2$. However, in this study the force that applies on the protrusion is the reaction force acting on the sample generated by the fixture. This reaction force could be considered as a compressive force. For compressive forces, the distribution of the force is not uniform on top and the bottom of a sample. Meyers and Chawla [21] suggested an equation for calculating the pressure differences.

$$p = \sigma_0 e^{2\mu(a-r)/h} \quad (22)$$

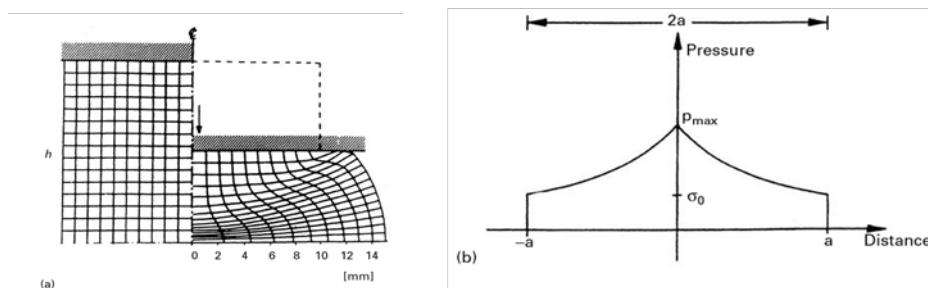


Figure 9- Variation in pressure on surface of specimen being compressed [21].

where P is pressure, σ_0 is yield stress, and μ is friction coefficient. Figure 10 shows a schematic of the distributed force on the bottom of the protrusion. To calculate L , the centroid of this exponential function should be defined.

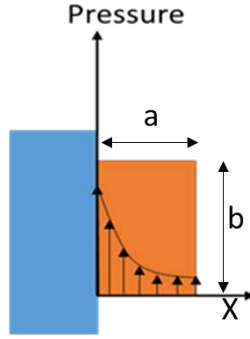


Figure 10- schematic of stress distribution caused by the reaction force.

$$L = \frac{\int_0^a x \sigma_0 e^{2\mu(x-a)/b} dx}{\int_0^a \sigma_0 e^{2\mu(x-a)/b} dx} = \frac{e^{\frac{2\mu x}{b}} \left(\frac{2\mu x}{b} - 1 \right) \Big|_0^a}{\frac{2\mu}{b} e^{\frac{2\mu x}{b}} \Big|_0^a} = \frac{e^{\frac{2\mu a}{b}} \left(\frac{2\mu a}{b} - 1 \right) + 1}{\frac{2\mu}{b} \left(e^{\frac{2\mu a}{b}} - 1 \right)} \quad (23)$$

$$L = \frac{e^{\frac{2\mu a}{b}} \left(\frac{2\mu a}{b} - 1 \right) + 1}{\frac{2\mu}{b} \left(e^{\frac{2\mu a}{b}} - 1 \right)} \quad (24)$$

$$\frac{e^{\frac{2\mu a}{b}} \left(\frac{2\mu a}{b} - 1 \right) + 1}{\frac{2\mu}{b} \left(e^{\frac{2\mu a}{b}} - 1 \right)} < \frac{b}{2\sqrt{3}} \quad (25)$$

$$\frac{\sqrt{3} \left(e^{\frac{2\mu a}{b}} \left(\frac{2\mu a}{b} - 1 \right) + 1 \right)}{\mu \left(e^{\frac{2\mu a}{b}} - 1 \right)} < 1 \quad (26)$$

As a reasonable assumption, consider $\mu=0.15$. Thus,

$$\frac{\sqrt{3} \left(e^{\frac{0.3a}{b}} \left(\frac{0.3a}{b} - 1 \right) + 1 \right)}{0.15 \left(e^{\frac{0.3a}{b}} - 1 \right)} < 1 \quad (27)$$

$$\frac{a}{b} < 0.562 \quad (28)$$

It can be concluded that for the design of a new test method, the necessary condition is that the ratio of a/b should be less than 0.562 to provide us with information about shear strength of the interface. As long as the sample design meets this criterion, we can assure that the fracture occurs in the shear plane.

Hook's law expresses the stress-strain relationship for elastic condition as below,

$$\varepsilon_x = \frac{1}{E}(\sigma_x - \nu(\sigma_y + \sigma_z)) \quad (29)$$

$$\varepsilon_y = \frac{1}{E}(\sigma_y - \nu(\sigma_x + \sigma_z)) \quad (30)$$

$$\varepsilon_z = \frac{1}{E}(\sigma_z - \nu(\sigma_x + \sigma_y)) \quad (31)$$

To simplify the calculations, a 2D problem for the interface plane is solved as shown in Figure 3B,

$$\varepsilon_z = \frac{1}{E}(\sigma_z - \nu\sigma_y) \quad (32)$$

$$\varepsilon_y = \frac{1}{E}(\sigma_y - \nu\sigma_z) \quad (33)$$

The deformation in Z direction is constrained by the base material. Therefore, there is no strain in this direction ($\varepsilon_z = 0$ and $\sigma_z = \nu\sigma_y$).

Based on Von-Mises criteria, for this condition,

$$\sigma_0 = [(v\sigma_y - \sigma_y)^2 + (\sigma_y)^2 + (v\sigma_y)^2 + 3(\sigma_{zy}^2)]^{0.5} \quad (34)$$

All aforementioned equations are satisfied when the dimensions of the base part are much greater than the dimensions of the protrusion. However, if the size of the protrusion is equal to the size

of the base part in the Z direction, a new boundary condition should be defined so that the two sides of the protrusion are considered free surfaces, therefore the stress components in these surfaces are zero. In addition, under this boundary condition, the reaction force distribution in Z direction is not uniformly distributed and the stress conditions are similar to those in the compression test, as shown in Figure 11. According to Equation 22, the pressure distribution in this Figure is obtained as,

$$p = \sigma_0 e^{2\mu(c/2-z)/b} \quad (35)$$

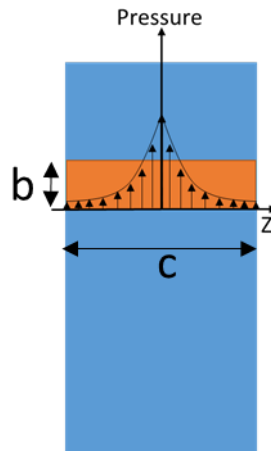


Figure 11- Pressure distribution in cantilever beam where the size of the base and protrusion are equal in Z direction.

To calculate the three-dimensional stress and strain distributions for different boundary conditions of a cantilever beam under the applied force, it is very difficult to obtain the analytical solution and the use of numerical methods such as finite element method appears to be essential. The finite element method (FEM) is a useful tool for problems with complicated geometries and loading where analytical solutions are difficult to obtain. For this reason, in this work, FEM simulation has been utilized to solve the abovementioned problem.

Methodology and Materials

A Haas UMC750 5-axis vertical milling machine retrofitted with an AMBIT Series 7 laser deposition head was used to produce the test pieces. The direct energy deposition head includes a laser beam and coaxial gas-powder. Argon gas was used as a shielding gas. The DED laser beam head is directed towards the substrate and creates a melt pool and material is continuously added in the process direction. The substrate material is 316L stainless steel. The direct energy deposition process was carried out at the scanning speed of 650 mm/min, and laser power of 300 W. The details about composition of substrate and powder are shown in the Table 1.

Table1- Chemical composition of stainless steel 316 of the substrate and the powder

Material Composition	Substrate (Wt %)	Powder (Wt %)
Iron	58.23-73.61	58.23-73.61
Carbon	0-0.08	0-0.03
Chromium	16-18.5	16-18.5
Copper	0-1	0-75
Manganese	0-2	0-2
Molybdenum	0-3	2-3
Nickel	10-15	10-14
Nitrogen	0-0.1	0-0.
Phosphorus	0-0.045	0-0.045
Silicon	0-1	0-0.75
Sulfur	0.35	0-0.015

Block Shear test

As mentioned, until now no documented efforts have been undertaken to establish a testing method for characterizing the bonding strength of hybrid manufactured parts. Based on the developed theory and the numerical calculations, this work tries to advance the design efforts of hybrid manufactured specimens for mechanical tests. For this purpose, a new testing method

has been proposed which is called block shear (BS) test to measure the magnitude of shear strength of the interface. The block shear test specimen is comprised of the base substrate with dimensions of 50.8, 50.8 and 12.7 mm to which a protrusion with dimensions of 25.4, 6.35 and 3.18 mm is added via additive manufacturing, as shown in Figure 12. To allow for a comparison, some samples were machined out of a single piece of substrate including the protrusion; these had the same geometry as the parts shown in Figure 12. The naming of different samples is shown in Table 2. The deposition rastering strategy is parallel, in which the deposition directions for all layers are the same, to avoid the formation of porosity between the layers of the deposited material.

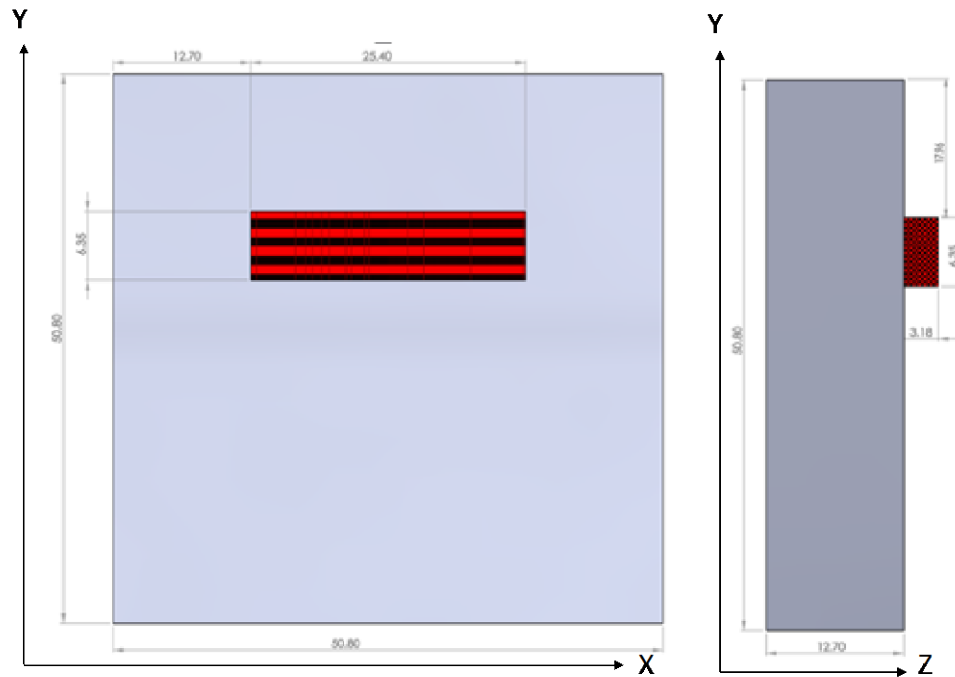


Figure 12- Top view and side view of block shear test samples manufactured by DED process along with the dimensions (mm) of the substrate and the printed part.

Table 2- Four different groups of samples for block shear and tensile shear

Testing method/manufacturing process	Machining	DED
Block Shear	M-BS	DED-BS
Tensile Shear	M-TS	DED-TS

The block shear test was conducted in the fixture that the authors designed for this work, Figure 13A. The fixture is composed of two main components, the body (50.8 x 50.8 x 100 mm) and the back plate. The back plate is 100 x 64 x 25 mm, with an extruded cut of size 12.7 x 60 mm. By using 4 screws that are designed in the back of the back plate, the distance between the body and back plate can be adjusted. For conducting the test, the sample is placed into the fixture with a 0.127 mm shim behind the sample. The screws are tightened to have a full contact between sample and fixture, and then the shim is removed as shown in Figure 13B. This assures a constant spacing between the fixture and sample. Thereafter, the fixture and sample are placed in a tensile test machine and a vertical load that is directed downward is applied upon the top of the sample. In this work, these experiments are conducted at room temperature, with a displacement rate of 1 mm/min, using a Shimadzu UH-300KNX tensile test machine.

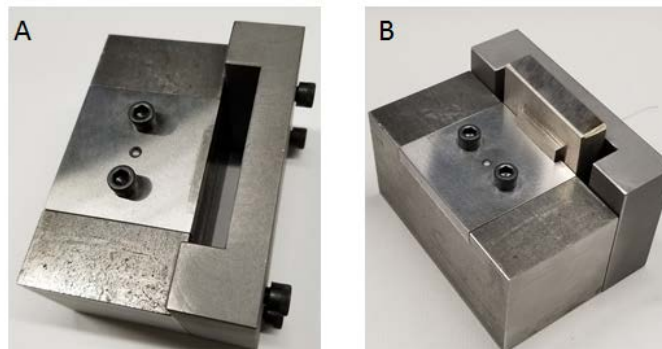


Figure 13- (A) Block shear test fixture; (B) the sample is placed in the fixture and block shear test is conducted using tensile test machine.

Tensile Shear test

The tensile shear test is mostly used for characterization of mechanical properties of clad parts. To understand the differences between the standard ASTM A264-09 shear test which is known as tensile shear test (Figure 14) and the block shear test that proposed by the authors, two groups of specimens are made: the specimen that is machined out of wrought material (M-TS sample), and the specimen that is made out of wrought material as the base and depositing material as the step (DED-TS sample). The specimens of tensile shear test are prepared according to the standard ASTM A264-09. Figure 15 shows the schematic of the tensile shear testing specimen that consists of wrought and deposited material (DED part) along with the corresponding dimensions. The depositing strategy is also shown in this Figure. For all samples, after deposition, the machining process is used to machine the part to the accurate dimensions. The tensile shear test was carried out using Shimadzu UH-300KNX tensile testing machine at room temperature and strain rate of 1mm/min. Each of the four samples shown in Table 2 were replicated five times.

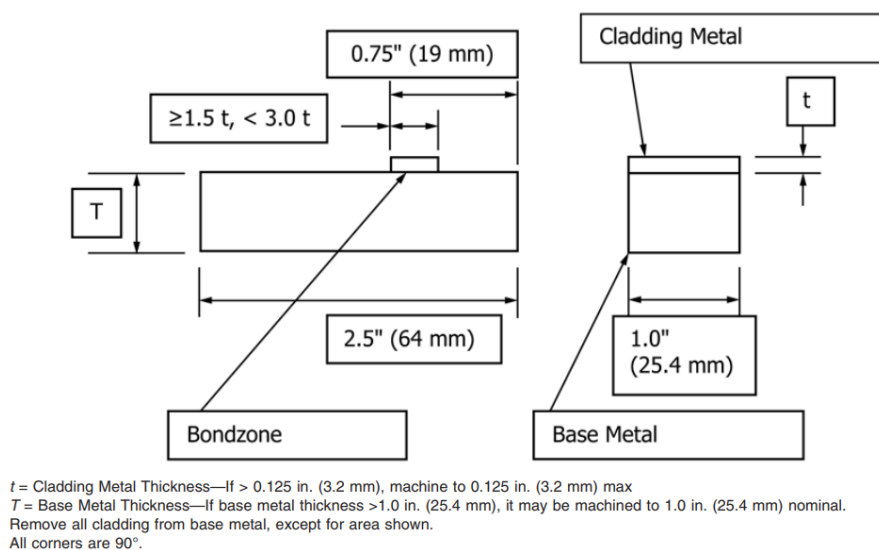


Figure 14- Tensile shear testing protocol according to the standard ASTM A264-09 [17].

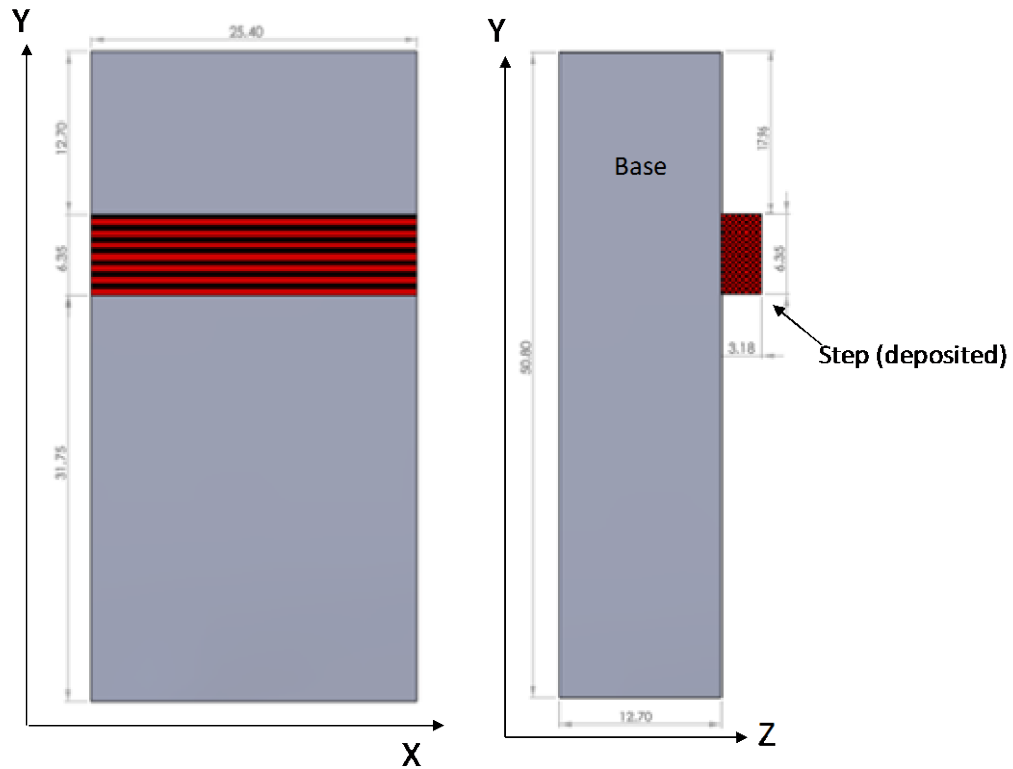


Figure 15- Top view and side view of tensile shear test specimens manufactured by DED process along with the dimensions (mm) of the substrate and the printed part.

Microstructural features of DED samples were investigated using optical microscopy. The metallography samples were cut, ground and polished with a final diamond grit size of 1 μm . To reveal the microstructure, the samples were chemically etched in a methanolic aqua regia (45 ml HCL, 15 ml HNO₃ and 20 ml methanol [22]) for 5 min. Microstructure observations were carried out using Leco LX31 microscope. Fractography studies were carried out on four different groups of samples, including DED- BS, M-BS, DED- TS, and M- TS, using scanning electron microscopy (SEM).

Finite Element Method

To simulate the block shear and standard tensile shear testing methods and comparing the stress distribution under these two test conditions, a two-dimensional and three-dimensional modeling were developed using finite element method (FEM) that was carried out in ABAQUS software. The model inputs include the part geometry, meshing, properties of material, and the initial and boundary conditions.

To validate the theory that the authors developed in the previous section and to analyze the force distribution in the protrusion component during shear testing, a two-dimensional finite element analysis was developed. A general static finite element procedure is considered for this analysis. The actual dimensions of the sample defined earlier were used as inputs into the FEM model. In this model, a distributed load was applied on top surface of the base part. The boundary condition in this problem are those that restrain the movement of the base part in X direction so that the displacement is 0 in X direction. The other boundary condition is that the bottom of the protrusion is constrained in Y direction as shown in Figure 16A. The reaction force distribution of 2D analysis of shear test sample is shown in Figure 16B. Comparison between the Figure 10 in the theory section and Figure 16 shows a reasonable agreement in the distribution of the reaction force.

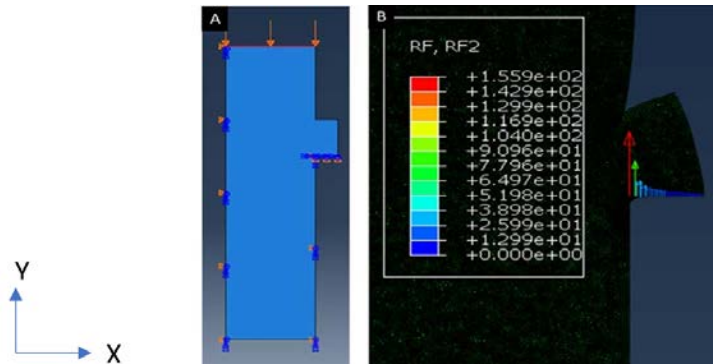


Figure 16- (A) The boundary conditions applied in the FEM analysis; (B) Two-dimensional analysis of force distribution under the shear test.

In this work, the FEM was used to analyze the distribution of stress during shear test under three dimensional conditions. The part geometry is defined for the block shear and tensile shear test specimens with dimensions identical to those of the experimental samples discussed in the methodology section. The material properties of the 316L stainless steel are density of 8000 kg/m^3 , Poisson's ratio of 0.28 and elastic modulus of 200 GPa. The plastic deformation properties of substrate material obtained from tensile testing are used as input in the FEM model. The fixture and load plate are defined as a discrete rigid body using a reference point. Degrees of freedom for these parts are defined on their respective reference points (RF). Figure 17 shows the overall framework of the finite element analysis of block shear and tensile shear testing method. The displacement and rotation of fixture's reference point in all directions is predefined as 0, so the fixture is fixed during the simulation. For the load plate, the displacement in Y direction is defined as -3 mm and 0 mm in the other directions. For modeling the shear test, a quasi-static state problem is considered that ignores the inertia effect during testing. To increase the computational efficiency the explicit dynamic finite element procedure is used rather than an implicit procedure. The interaction between surfaces is assumed to be contact-friction using the Penalty Method with the friction coefficient considered as 0.3 and isotropic directionality.

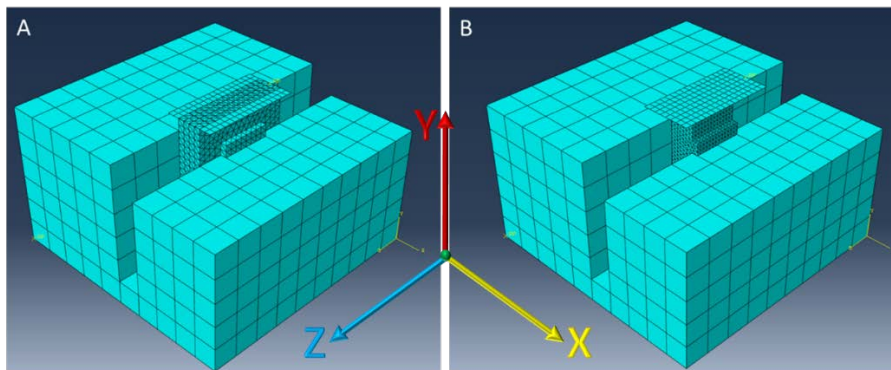


Figure 17- The overall framework of the finite element analysis of (A) block shear and (B) tensile shear testing method.

The FEM results of stress distribution from a three dimensional analysis of the block shear and tensile shear tests are presented in Figure 18. As seen in this Figure, the stress distribution at the interface of these two test methods is different. Figure 18 A, C, E, G show the stress distribution in block shear sample and Fig 18 B, D, F, H show the stress distribution in tensile shear sample in different planes and different directions. Figure 18A and 18B show the distribution of the normal stress in the X direction.

The stress distribution is different in block shear and tensile shear samples. In the tensile shear sample, the normal stress acting in the X direction affects a considerable region in the edge of the interface (denoted by red). Figure 18C and 18D show the shear stress acting in the interface plane in the Y direction. As seen in Figure 18C the shear stress is mainly distributed in the interface plane, while for the tensile shear sample, Figure 18D, shear stress is distributed not only in the interface plane, but also in the regions out of the interface plane. Figure 18E and 18F demonstrate the stress distribution in the XY plane and Z direction (S33). As discussed in the theory section, the stress in the free surface is zero. As seen in Figure 18F, the distribution of normal stress in the Z direction is non-uniform with maximum value in the center and zero value at the two ends (free surfaces). In addition, the simulation results show the concentration of shear stress in the XY plane of tensile shear sample, Figure 18H, whereas in block shear sample, the shear stress in the XY plane is distributed uniformly along the interface as shown in Figure 18G.

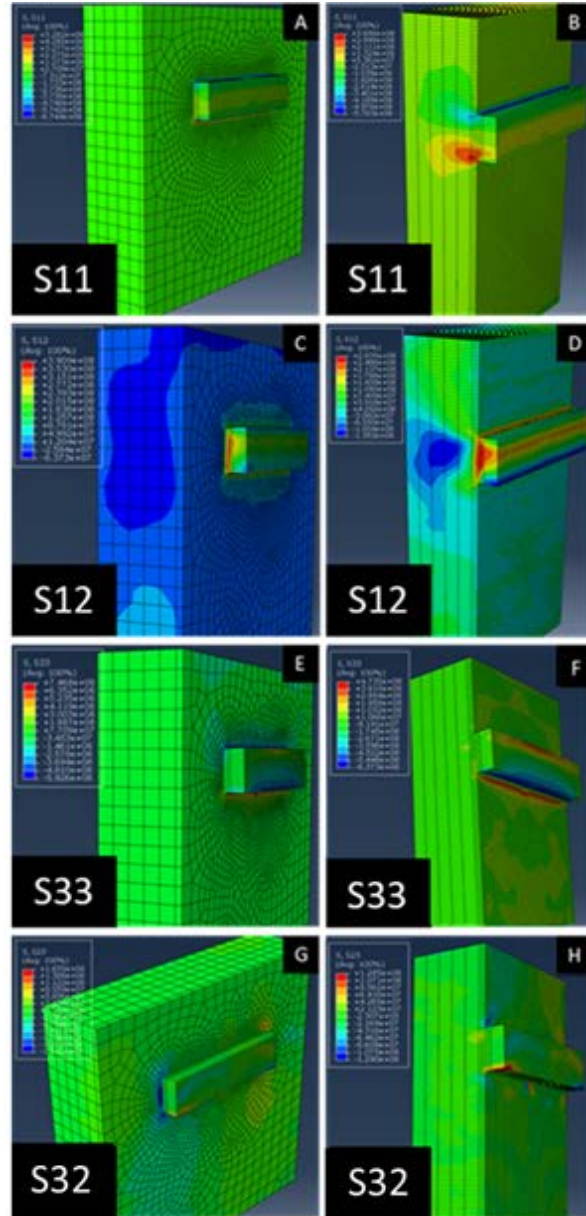


Figure 18- Three-dimensional analysis of stress distribution in different directions after the block shear test (A) YZ plane and X direction; (C) YZ plane and Y direction; (E) XY plane and Z direction; (G) XY plane and Y direction; and after the tensile shear test (B) YZ plane and X direction; (D) YZ plane and Y direction; (F) XY plane and Z direction; (H) XY plane and Y direction.

The differences in the stress distribution between the block shear and tensile shear samples come from their geometry and boundary conditions. For the tensile shear samples, the two sides are free surfaces and the stresses on these surfaces are zero. In addition, there is no constraint for deformation on these free surfaces. On the other hand, the protrusion feature in

block shear sample is constrained with the base part. The results of FEM can be used to numerically analyze the differences between these two testing methods in terms of stress and strain distribution in different planes and directions. The testing method in this work is defined as a method that can provide us with information about the shear strength of the interfacial bonding of hybrid manufactured part. The results obtained from FEM allow us to analyze the stress distribution in the interface plane under the block shear and tensile shear test conditions and help to design a suitable testing method for determining the interfacial bonding strength. In addition, the experimental results can be used to verify the finite element analysis.

Results and discussion

In this work, the block shear test has been proposed as a method for measuring the interfacial bonding strength of hybrid manufactured parts. Several experiments were designed and performed to demonstrate that this testing method is capable of providing reliable and meaningful results. In this section the results of microstructural observations, mechanical properties and fractography of the specimens after testing are presented. The results of the proposed block shear test are compared with the existing tensile shear testing method.

Microstructural features

A review of the microstructures created during these experiments is presented here to provide a basis for the testing conducted. Figure 19 shows the optical microscopy of the deposited layers, molten pool boundaries from longitudinal cross section, and microstructure at different zones of the deposited layer produced with a scanning speed of 650 mm/min and laser power of 300 W. Under optical microscopy observation, the arc-shaped molten pool boundaries due to Gaussian energy distribution of laser beam are shown in Figure 19B. Figure 19C shows

the arc-shaped interface of the first and second layer of the deposited part. This pattern is repeated with the proceeding of successive layer-upon-layer deposition. The microstructure of deposited layer in zone D consists of coaxial grains. In zone E the columnar grains are seen due to the rapid solidification that are dragged into the layer. Zone F illustrates the boundary between the first layer of the deposited part and the substrate.

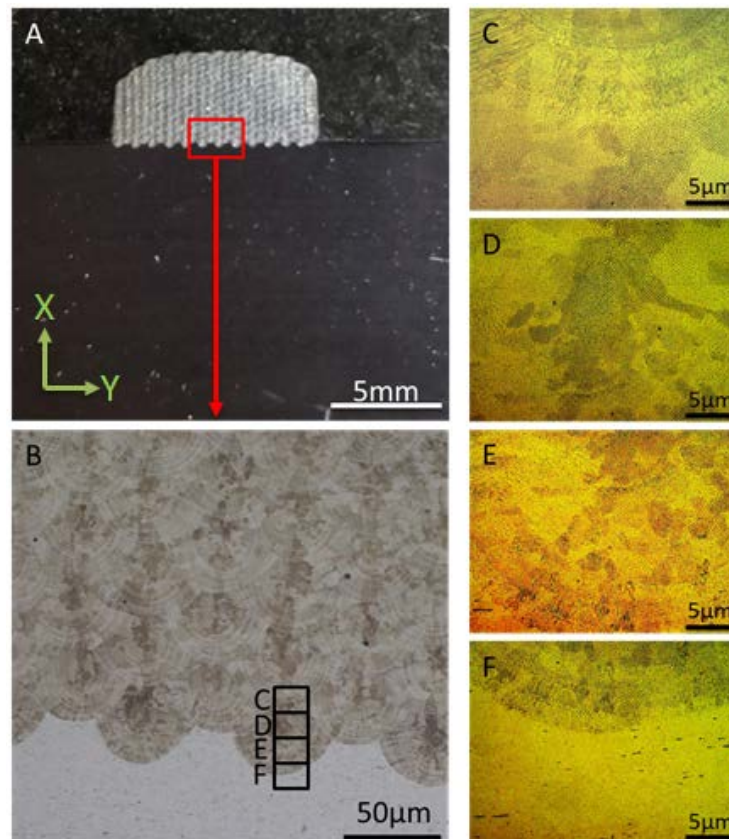


Figure 19- Optical microscopy of (A) cross section of deposited layers, (B) molten pool boundaries, (C) arc shape interface of the first and second layer of the deposited part, (D) coaxial grain morphology (E) Columnar grains (F) boundary between the substrate and deposited part.

Figure 20 shows the optical microscopy representation of the boundary of substrate/ deposited part, and the interface between different layers of the deposited part at different magnifications. It is interesting that despite the high cooling rate, no Heat Affected Zone (HAZ)

has been detected in the Figures 20A to 20D. Generally, a HAZ is formed due to the grain growth in the substrate adjacent to the molten pool. Grain growth depends on initial grain size, time and temperature of the process according to equation below [23]:

$$D^2 - D_0^2 = Kt \quad (36)$$

where D is average grain diameter, D_0 is the initial grain size, t is time and K is temperature dependent constant. The below Equation shows the relationship between K and heating temperature T .

$$K = K_0 e^{-\frac{Q}{RT}} \quad (37)$$

here, K is constant, and Q is the activation energy for boundary mobility.

In DED method, since the cooling rate is relatively high, there is not sufficient time for significant growth of the grains. Also, a very small region is affected by high temperature during the DED process. For these reasons, no heat affected zone is detected in the microstructure, or it might be very small that cannot be detected.

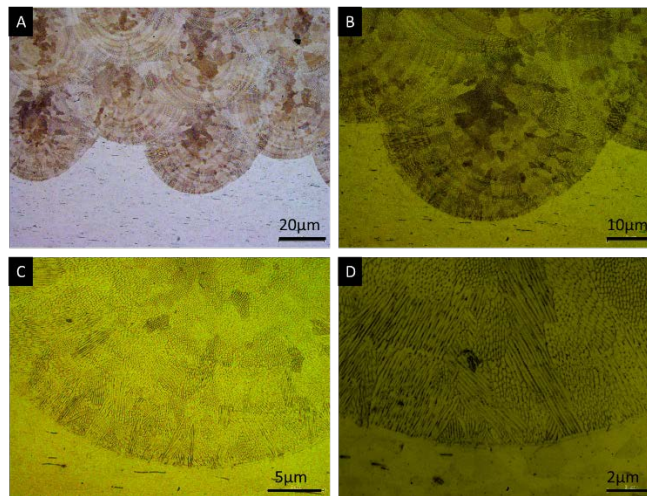


Figure 20- Optical microscopy of the boundary of substrate/ deposited part at different magnifications. No heat affected zone is detected in this Figure.

The microstructure of the deposited layer and the substrate can be compared under optical microscopy observation in Figure 21. As shown in Figure 21A, the deposited layer consists of fine coaxial grains with smaller size, whereas the substrate is composed of coarse grains.

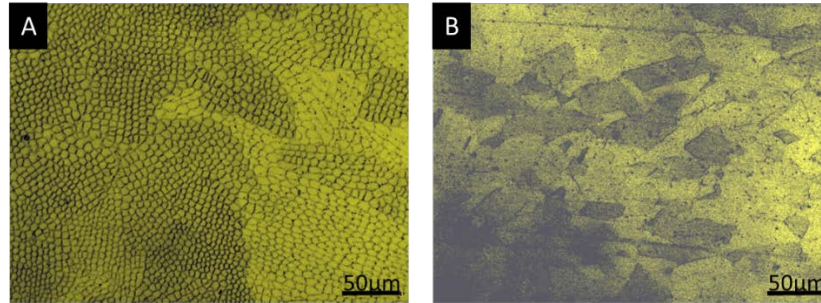


Figure 21- The optical microscopy of grain morphology of (A) deposited layer and (B) substrate.

Tensile shear test

Stress-displacement curves of parts manufactured by DED process (DED_TS), and machining (M_TS) obtained from the tensile shear test are shown in Figure 22. The experiments have been replicated five times under the same conditions. The tensile shear test is a suitable method for evaluating the bonding strength of clad plates. In this work, the standard tensile shear test method was conducted for DED and machined parts and the stress-displacement results and fractography observations were compared with block shear test. Results demonstrate different behavior for tensile shear test of the DED and machined specimens.

As seen in Figure 22, for the machined specimens, it is interesting that there are two linear regions in the stress-displacement curve. Thus, the stress-displacement curve obtained from tensile shear test is different from uniaxial tensile test and pure shear test. One possible reason for the aforementioned result is that in the case of tensile shear test of machined part the

fracture mode is changed from opening mode to shearing mode during the test. The other reason of this behavior might be due to the work hardening that occurs for the material during the test. Generally, the stress value obtained from tensile shear test does not show the pure shear strength of the interface. Moreover, the stress-displacement curve for machined part and DED part obtained from the tensile shear test are not consistent. Thus, it is not possible to validate the results of tensile shear test for DED part. As seen, all five measurements of the stress-displacement curves for both groups of samples show the same trend. The most important information that these five data sets can provide is that all the replicate measurements show a similar trend of stress-displacement relationship.

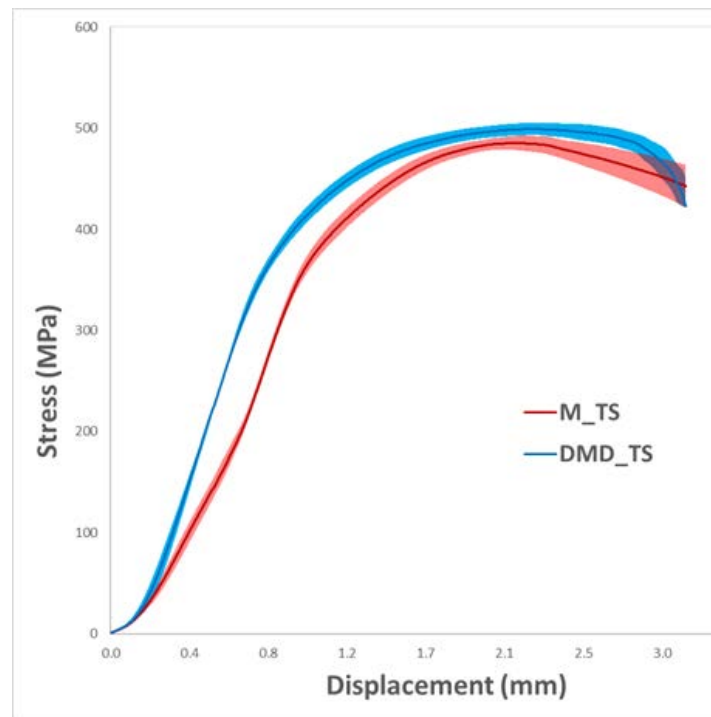


Figure 22- Stress-displacement graphs of 316L stainless steel manufactured by DED process, and machining process after tensile shear test.

Block shear test

To evaluate the interfacial bonding strength of the substrate and the printed part of 316L stainless steel fabricated by DED method, the block shear test was used. The specimens were fabricated at a scanning speed of 650 mm/min and laser power of 300 W. To demonstrate that the block shear test is a reliable testing method for evaluating interfacial bonding strength, the specimens with the same dimensions as the hybrid parts were fabricated using machining process and the block shear test was performed to evaluate the bonding strength of these specimens. Figure 23 shows engineering stress-displacement curves of the DED part (DED-BS sample), and the wrought part fabricated by machining process (M-BS sample). Each experiment has been replicated five times. A first observation shows that the DED part has higher yield stress compared to machined wrought material. The average yield stress is measured as 330 MPa and 280 MPa for DED part and machined part, respectively. The higher yield stress of DED part is because of the rapid solidification that results in the formation of fine grains in deposited layers of the stainless steel during the DED. Also, the elongation at break is seen to be lower for DED part compared to the machined specimen. A possible explanation is the internal stress and the existence of porosity that are unfavorable for ductility. As seen in this Figure, the ultimate strength of DED part is approximately equivalent to that of the machined part. Unlike the tensile shear test, for the block shear test we are able to validate the test result by performing the same test on machined part. Generally, by comparison the block shear test results of DED part and machined part, it can be concluded that this test method is reliable for evaluating interfacial bonding strength of additive manufactured parts.

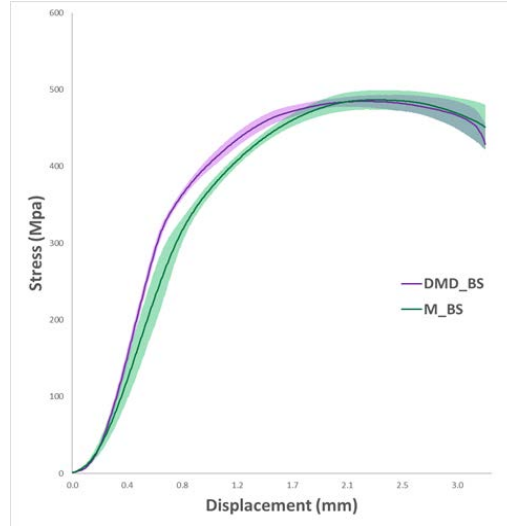


Figure 23- Stress-displacement graphs of 316L stainless steel manufactured by DED process, and machining process after block shear test.

Macro-fractography

Figure 24 shows the crack formation and propagation process at room temperature, where the samples are manufactured and tested at different conditions; (A) machined part under block shear test, (B) DED part under block shear test, (C) DED part under tensile shear test, and (D) machined part under tensile shear test. It can be seen from Figure 24 that the cracks in A, B and C start to appear and propagate in the main shear plane parallel to the loading direction, whereas in Figure 24D the crack propagates in multiple directions. Afterwards, these cracks quickly develop, and the propagation speed becomes faster until fracture of the samples. The modes of fracture are different depending on different shear test conditions and manufacturing process. The macro-fractography of the crack path in Figure 24D can be used to explain the observation from stress-distribution curve in Figure 22 in which the tensile shear test results of machined part do not follow the pattern of stress-strain relationship of the standard tensile or pure shear test.

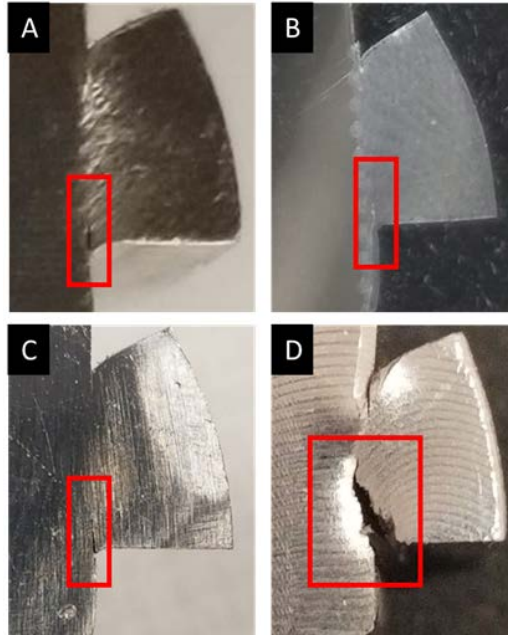


Figure 24-Crack formation and propagation in (A) machined part under block shear test, (B) DED part under block shear test, (C) DED part under tensile shear test, and (D) machined part under tensile shear test.

SEM fractography

The tensile shear and block shear tests were conducted under the condition that the load is applied parallel to the interface line to investigate the interfacial bonding strength of parts. The interfacial morphologies of fractured surfaces of different parts were examined by scanning electron microscopy (SEM). Variations of fracture with the test method are shown in Figures 25 to 28. The fractural surface morphology after tensile shear test of DED part is shown in Figure 25. The fractography shows the mixture of two fracture morphologies. The dimples are not elongated, but there are a few deep and large dimples in the fracture surface. The elongated dimples are formed due to the shear deformation; however, the deep and large dimples are formed under the influence of tensile stress. As seen in Figure 25, the dimples are not oriented in the shear direction. In general, the orientation of dimples and the fracture morphology show that the final fracture caused by the shearing and tensile mechanisms. From the SEM fractography, it

can be concluded that the interfacial bonding strength obtained from the stress-strain curve is the mixture of shear and tensile stress.

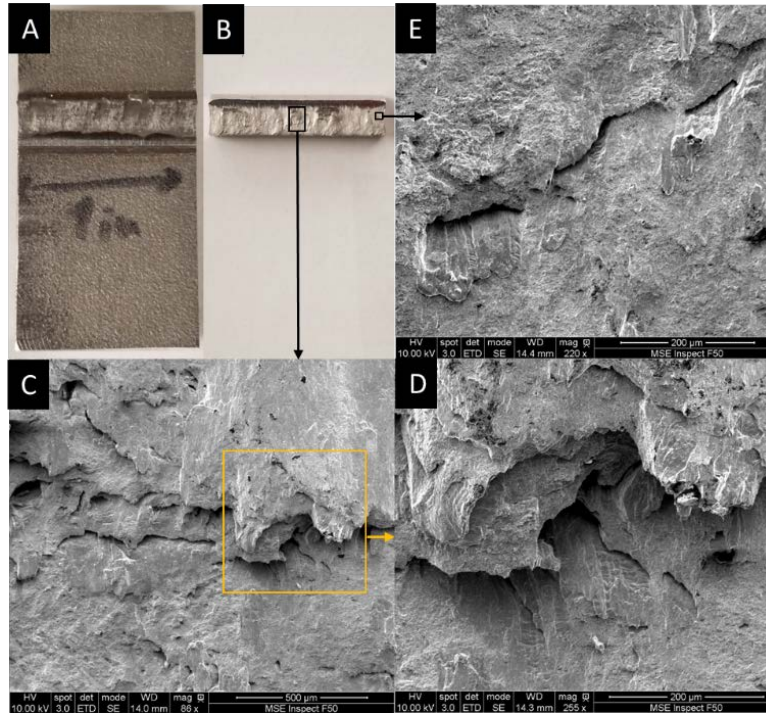


Figure 25- Fractography of DED part after tensile shear test; (A) Macro-fractography of substrate; (B) Macro-fractography of deposited part; (C), (D) and (E) scanning electron microscopy of the fracture surface, showing that the dimples are not oriented in the shear direction.

Figure 26 reveals the fracture surface of the machined part after tensile shear test. It is important to note that in this sample, fracture does not occur in one plane. The macro-fractography in Figure 24D shows that the specimen was found not to be fractured at the interface bonding surface. The SEM fractography proved this observation that the crack starts from the interface and propagates through the substrate. The fracture surface here exhibits deep and large dimples in different planes. In Figure 26D, dimples with sharp edges are seen that are oriented in the direction of the applied load which generally indicates the classic tensile dimples [24]. The fracture mode of this sample is expected to be the result of the combination of tensile

and shear stresses. The fracture surface features of the machined and DED samples after tensile shear test seem to be different, comparing the SEM images. These results are in good agreement with the argument that why tensile shear test is not a reliable testing method for measuring shear strength of the DED parts.

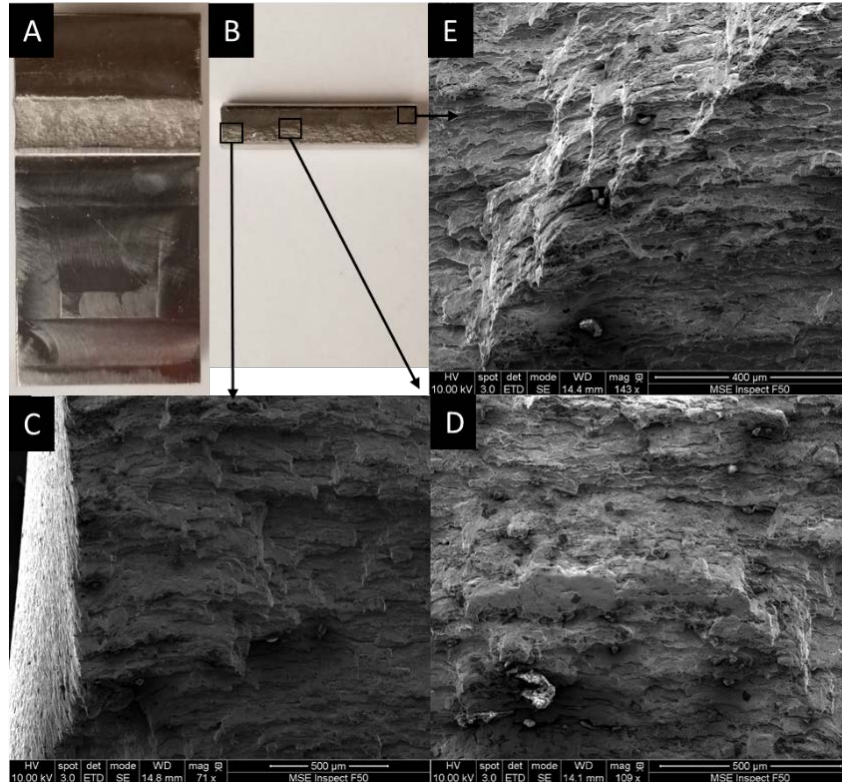


Figure 26- Fractography of machined part after tensile shear test; (A) and (B) Macro-fractography images, showing that the fracture does not occur at the interface; (C), (D) and (E) scanning electron microscopy of the fracture surface, showing deep and large dimples in different planes.

The SEM image of interfacial fractography after block shear test of DED part is illustrated in Figure 27. With regards to this Figure, there are small dimples which are oriented in the fracture direction. Since the dimples are elongated in the shear direction, it can be concluded that dimples are formed in the presence of shear deformation [25]. At the end of the block shear test of DED part, the specimens are cut off along the bonding interface. In other

words, the fracture direction is seen to be parallel to the interface plane that shows the mode of fracture is dominated by shear stress. The elongated shallow small shear dimples observed in the fracture surface is indicative of ductile fracture [26]. At the end of the block shear test, the interfacial delamination occurs due to the total separation between the substrate and printed part.

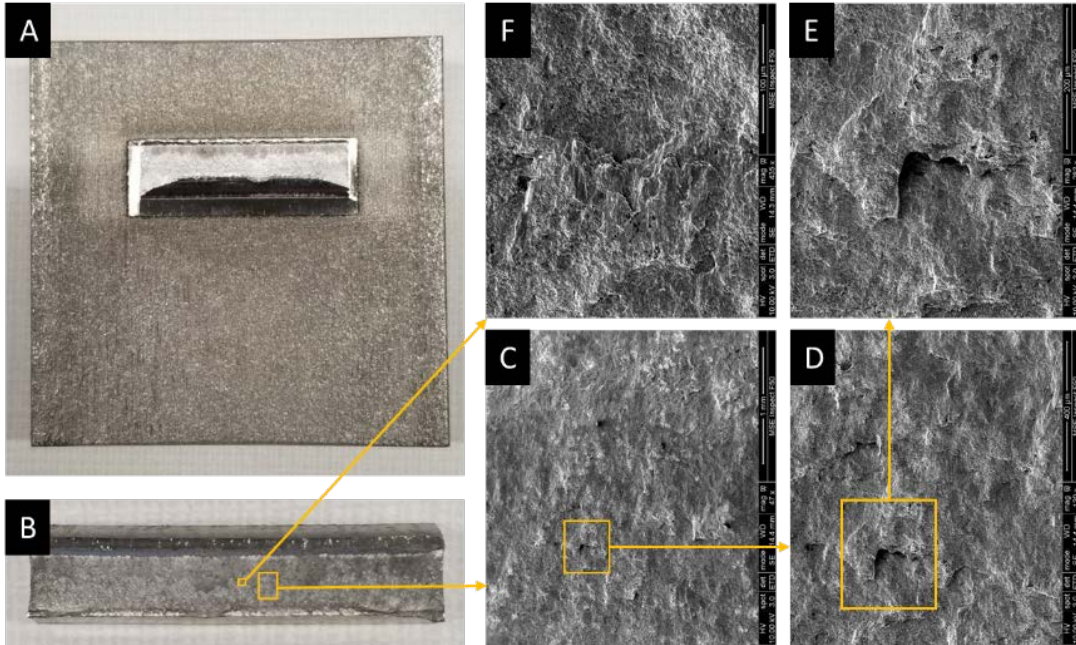


Figure 27- Fractography of DED part after block shear test; (A) Macro-fractography of substrate; (B) Macro-fractography of deposited part; (C) and (D) scanning electron microscopy of the fracture surface; (E) and (F) direction of dimples, showing that they are elongated in the direction of shear stress.

Figure 28 demonstrates the fracture appearance of the stainless steel after block shear test of the machining part. The observation shows dimpled fracture surface similar to Figure 27. After block shear test, unlike the tensile shear test, the dimples are elongated in the shear load direction which is parallel to the interface of substrate and printed part. It can be seen from Figure 27 and 28 that for block shear test of machining and DED parts, the fractural surface morphologies are mostly the same. In the case of machining and DED parts, the average shear strength after the block shear test was found to be about 480 MPa. The observations indicate that

block shear test is a reliable test method for evaluating interfacial bonding strength of both parts manufactured by DED and machining.

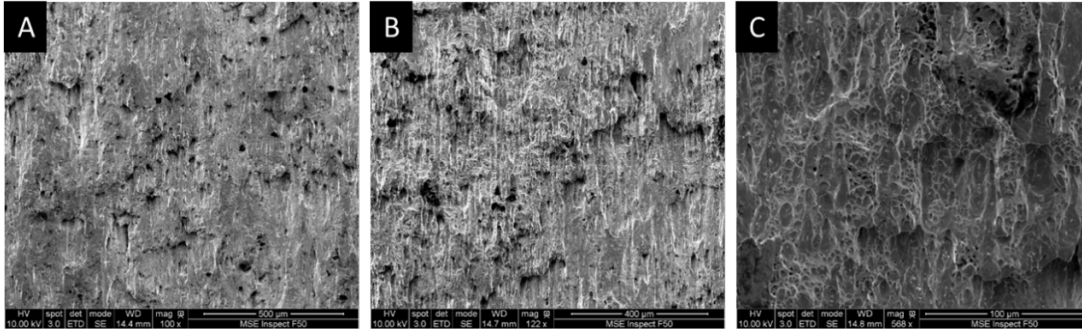


Figure 28- Scanning electron microscopy of the fracture surface after block shear test of machined part. (A), (B) and (C) show the elongated dimples in different regions of fracture surface.

Conclusion

In this work, a testing methodology for measuring the interfacial bonding strength of hybrid manufactured parts was proposed which is called block shear test. For this purpose, block shear test specimens were manufactured such that the 316L stainless steel was deposited with specific dimensions on the substrate. Based on the theory that has been developed, the dimensions of the test specimens were determined. The finite element analysis (FEM) was used to numerically analyze the distribution of the stress in the interface plane of the sample under block shear test loading. The results of FEM predicted that the fracture occurs at the interface of the substrate/deposited material due to shear stress. The fractography observations proved this, showing that the fracture takes place due to the shear stress in the interface plane. To validate this testing methodology, another group of specimens were fabricated completely by machining. All of the same experiments were performed on these specimens. The comparison showed that the stress- displacement relationship and fractography of machined part, generally, are in good agreement with those of DED part. Prior to the block shear experiments, the tensile shear test

was carried out on two groups of specimens: hybrid manufactured and machined specimens. The results of tensile shear test were not consistent. Consequently, the authors proposed and validated a new testing method. It was concluded that the results of interfacial strength obtained from block shear test are strongly reliable that makes it a suitable testing method for measuring the interfacial bonding strength in hybrid manufacturing.

References

- [1] P. Peyre, P. Aubry, R. Fabbro, R. Neveu, and A. Longuet, “Analytical and numerical modelling of the direct metal deposition laser process,” *J. Phys. Appl. Phys.*, vol. 41, no. 2, p. 025403, Jan. 2008, doi: 10.1088/0022-3727/41/2/025403.
- [2] R. M. Mahamood, E. T. Akinlabi, M. Shukla, and S. Pityana, “Revolutionary additive manufacturing: an overview,” 2014.
- [3] J. Song, Q. Deng, C. Chen, D. Hu, and Y. Li, “Rebuilding of metal components with laser cladding forming,” *Appl. Surf. Sci.*, vol. 252, no. 22, pp. 7934–7940, Sep. 2006, doi: 10.1016/j.apsusc.2005.10.025.
- [4] R. M. Mahamood, “Laser Basics and Laser Material Interactions,” in *Laser Metal Deposition Process of Metals, Alloys, and Composite Materials*, R. M. Mahamood, Ed. Cham: Springer International Publishing, 2018, pp. 11–35.
- [5] M. Merklein, D. Junker, A. Schaub, and F. Neubauer, “Hybrid Additive Manufacturing Technologies – An Analysis Regarding Potentials and Applications,” *Phys. Procedia*, vol. 83, pp. 549–559, Jan. 2016, doi: 10.1016/j.phpro.2016.08.057.
- [6] K. p. Karunakaran, C. Amarnath, and A. Sreenathbabu, “Statistical process design for hybrid adaptive layer manufacturing,” *Rapid Prototyp. J.*, vol. 11, no. 4, pp. 235–248, Sep. 2005, doi: 10.1108/13552540510612929.
- [7] M. Kerschbaumer and G. Ernst, “Hybrid manufacturing process for rapid high performance tooling combining high speed milling and laser cladding,” *Int. Congr. Appl. Lasers Electro-Opt.*, vol. 2004, no. 1, p. 1710, Oct. 2004, doi: 10.2351/1.5060234.
- [8] N. Shamsaei, A. Yadollahi, L. Bian, and S. M. Thompson, “An overview of Direct Laser Deposition for additive manufacturing; Part II: Mechanical behavior, process parameter optimization and control,” *Addit. Manuf.*, vol. 8, pp. 12–35, Oct. 2015, doi: 10.1016/j.addma.2015.07.002.
- [9] Y. Zhai, D. A. Lados, E. J. Brown, and G. N. Vigilante, “Understanding the microstructure and mechanical properties of Ti-6Al-4V and Inconel 718 alloys manufactured by Laser Engineered Net Shaping,” *Addit. Manuf.*, vol. 27, pp. 334–344, May 2019, doi: 10.1016/j.addma.2019.02.017.

- [10]X. Shi *et al.*, “Selective laser melting-wire arc additive manufacturing hybrid fabrication of Ti-6Al-4V alloy: Microstructure and mechanical properties,” *Mater. Sci. Eng. A*, vol. 684, pp. 196–204, Jan. 2017, doi: 10.1016/j.msea.2016.12.065.
- [11]Y. Z. Zhang, Y. T. Liu, X. H. Zhao, and Y. J. Tang, “The interface microstructure and tensile properties of direct energy deposited TC11/Ti2AlNb dual alloy,” *Mater. Des.*, vol. 110, pp. 571–580, Nov. 2016, doi: 10.1016/j.matdes.2016.08.012.
- [12]S. Dongare, “A Mechanical Testing Methodology for Metal Additive Manufacturing Processes.”
- [13]C. P. Paul, H. Alemohammad, E. Toyserkani, A. Khajepour, and S. Corbin, “Cladding of WC–12 Co on low carbon steel using a pulsed Nd:YAG laser,” *Mater. Sci. Eng. A*, vol. 464, no. 1, pp. 170–176, Aug. 2007, doi: 10.1016/j.msea.2007.01.132.
- [14]B08 Committee, “Test Method for Adhesion or Cohesion Strength of Thermal Spray Coatings,” ASTM International. doi: 10.1520/C0633-79R99.
- [15]M. Xu, J. Li, J. Jiang, and B. Li, “Influence of Powders and Process Parameters on Bonding Shear Strength and Micro Hardness in Laser Cladding Remanufacturing,” *Procedia CIRP*, vol. 29, pp. 804–809, Jan. 2015, doi: 10.1016/j.procir.2015.02.088.
- [16]S. Wei, G. Wang, L. Wang, and Y. Rong, “Characteristics of microstructure and stresses and their effects on interfacial fracture behavior for laser-deposited maraging steel,” *Mater. Des.*, vol. 137, pp. 56–67, Jan. 2018, doi: 10.1016/j.matdes.2017.10.020.
- [17]A01 Committee, “Specification for Stainless Chromium-Nickel Steel-Clad Plate,” ASTM International. doi: 10.1520/A0264-09.
- [18]J. L. Meriam and L. G. Kraige, *Engineering Mechanics: Statics*, 7th Edition Binder Ready Version edition. New York u.a.: Wiley, 2011.
- [19]F. Dai, *Mechanics of Material James M. Gere Sixth /6th Edition*. .
- [20]S. T. Rasmussen, “Analysis of dental shear bond strength tests, shear or tensile?,” *Int. J. Adhes. Adhes.*, vol. 16, no. 3, pp. 147–154, Jan. 1996, doi: 10.1016/0143-7496(95)00029-1.
- [21]M. A. Meyers and K. K. Chawla, *Mechanical Behavior of Materials*. Cambridge University Press, 2008.
- [22]“ASM Handbook Volume 9: Metallography and Microstructures - ASM International.” https://www.asminternational.org/search/-/journal_content/56/10192/06044G/PUBLICATION (accessed Nov. 19, 2018).
- [23]C. Yue, L. Zhang, S. Liao, and H. Gao, “Kinetic Analysis of the Austenite Grain Growth in GCr15 Steel,” *J. Mater. Eng. Perform.*, vol. 19, no. 1, pp. 112–115, Feb. 2010, doi: 10.1007/s11665-009-9413-y.
- [24]A. Griebel, “Technical Brief: Fatigue Dimples,” *J. Fail. Anal. Prev.*, vol. 9, no. 3, pp. 193–196, Jun. 2009, doi: 10.1007/s11668-009-9228-z.

- [25]Z. Dhib, N. Guerhazi, A. Ktari, M. Gasperini, and N. Haddar, “Mechanical bonding properties and interfacial morphologies of austenitic stainless steel clad plates,” *Mater. Sci. Eng. A*, vol. 696, pp. 374–386, Jun. 2017, doi: 10.1016/j.msea.2017.04.080.
- [26]I. Barsoum and J. Faleskog, “Rupture mechanisms in combined tension and shear—Experiments,” *Int. J. Solids Struct.*, vol. 44, no. 6, pp. 1768–1786, Mar. 2007, doi: 10.1016/j.ijsolstr.2006.09.031.

CHAPTER 4. THE CHARACTERIZATION OF MICROSTRUCTURE AND MECHANICAL PROPERTIES OF SUBSTRATE/DEPOSITED MATERIAL INTERFACE IN DIRECT ENERGY DEPOSITION

Ali Baghersaghchi Khorasani^{1*}, Frank Peters¹, Scott Chumbley²

1. Department of Industrial and Manufacturing Systems Engineering, Iowa State University, 3004 Black Engineering, Ames, IA 50011
2. Department of Materials Science and Engineering, Iowa State University, 2240 Hoover, Ames, IA 50011

Introduction

Direct energy deposition (DED) is an additive manufacturing technology capable of rapid prototyping, producing parts with complex geometry, and repairing damaged components through a layer-by-layer deposition with minimum material losses [1]. DED is an emerging manufacturing technology with a wide variety of applications in aerospace, automotive, oil & gas, marine, architecture, and power generation industries [2] due to its capability to produce higher density and larger parts with high printing speed compared to the other metal AM processes. In DED process, the part is built simultaneously by directly melting the feed stock material (wire or metal powder) using a concentrated heat source (which is commonly a laser) and the deposition of the material on a substrate [1].

It was found that during DED process, thermal history, melt pool geometry, microstructural features, mechanical properties, and degree of porosity vary in as-deposited sample from bottom to top layer. Akbari et al. [3] reported that the geometry of melt pool varies in different layers of deposition in parts fabricated by DED. The corresponding microstructure characteristics such as grain size and morphology differ at different regions of deposited material. The reason can be attributed to different cooling rates and solidification rates that the part experiences in various layers. For example, the top layers experience slower cooling rates

and lower heat loss through the substrate. Manvatkar et al. [4] developed a 3D heat transfer model to simulate the temperature distribution and melt pool geometry in different layers of AM parts. The experimental and numerical results showed that the melt pool size increases continuously from the bottom layer to the top layer. They also reported that the thermal cycles and cooling rates vary from the first to the ninth layers. It is expected to observe different microstructural features and correspondingly mechanical properties in different layers of a given part due to different thermal history that they experience during the process. Xu et al. [2] demonstrated that different layers of the deposited part (first layer to ninth layer) can be distinguished via the different microstructural characteristics, indicating anisotropic microstructural distributions. For example, in the bottom layers of the sample, finer microstructure is formed due to the higher cooling rate. However, as the deposition progresses to the middle layers, the size of grains increases. In the middle layers, the dendrite and cellular structures with different grain growth orientations can be found due to the lower cooling rates. At top layers, the cooling rate increases and fine grains are formed accordingly. Also, Dinda et al. [5] investigated the changes of the microstructural morphology from the bottom to the top layer of the as-deposited samples of the Ni-based superalloy. Yadollahi et al. [6] performed the microhardness measurements along the length of a multi-layer single bead specimen at different layers and showed that there is a variation in microhardness values. They also showed that the compressive yield strength varies at different regions, so that the bottom layers and top layers exhibit higher yield strength compared to the middle layers. Izadi et al. [7] indicated that in the bottom layers that are close to the substrate, more porosity is seen compared to the top layers. The reason can be attributed to the higher heat loss and cooling rate in bottom layers. They also concluded that porosity is more sensitive to laser power.

The presence of porosity in a part built via DED has been proven to affect the overall quality of the part and mechanical properties like tensile strength. In fact, microstructure and integrity are two main factors that significantly influence the mechanical properties of the DED part. Two types of porosity can be formed during DED process: the interlayer porosity that results from lack of fusion; and intralayer or gas porosity. The former can be reduced by optimizing the process parameters. For example, with increasing laser power it is expected to observe less interlayer porosity in the boundaries [8]. Although some studies have shown that with increasing scanning speed, porosity tends to decrease [8], [9], there is no obvious correlation between scanning speed and porosity formation [10]. It has been reported that intralayer porosity highly depends on the powder feed rate and dynamics of melt pool [11], [12]. Valdez et al. [13] studied the effect of porosity on mechanical properties of Inconel 718 produced via laser AM. They intentionally introduced different amount of porosity in samples and compared the tensile and compression strength. They showed that the least dense sample exhibited yield strength that was about 25% of the Inconel 718 produced via conventional manufacturing, while the fully dense AM sample was about 90%. They concluded that the mechanical properties is highly sensitive to porosity. Bandyopadhyay et al. [14] demonstrated that if porosity increases from 18% to 32% the elastic modulus reduces by 10%.

Despite of all its advantages, there are challenges associated with DED. One of the key challenges is the sensitivity of the final microstructure and mechanical properties on the thermal history of the part during DED process. The interactions of DED process parameters such as scanning speed, laser power, and metal feed rate can lead to a complex thermal history within the part. A large number of studies have been conducted to analyze the effect of process parameters on thermal history and therefore the microstructure and mechanical properties of a DED part.

The subsequent heating and cooling cycles during deposition can cause the formation of anisotropic microstructure in the deposited layers. Zhang et al. [15] demonstrated that the temperature gradient and therefore microstructure and mechanical properties in 316L stainless steel produced by DED are more sensitive to scanning speed than the laser power. They showed that with decreasing laser power and increasing scanning speed, yield strength of tensile test specimens increased. Wang et al. [16] investigated the effect of process parameters on the tensile mechanical properties of 304L stainless steel printed by DED. They carried out tensile testing and found that the elongation in the sample loaded along the longitudinal direction (perpendicular to the deposition direction) is less compared to the transverse direction (parallel to the deposition direction), while there is no clear trend between yield strength and direction. They reported that lower laser power results in finer microstructure and therefore higher yield strength.

In this work, DED is used to build up a feature on a substrate that has been manufactured using conventional manufacturing technologies, in this particular work via wrought processes. Hence, evaluating the strength of the substrate/ deposited material interface will be required as the need arises for components to be produced by DED. In the present work, a suitable range of process parameters have been selected to minimize the formation of porosity for improving the mechanical properties of substrate/deposited material interface. A detailed study on the heat transfer modes and thermal history in the melt pool and their effects on microstructure and therefore mechanical properties is undertaken in the present research. The microstructural characterization of the parts is examined and the yield strength of the interface is evaluated. The analysis of variance (ANOVA) is employed to relate the process parameters with geometry characteristics of the melt pool. As a result, a correlation between process parameters and the strength of interface is established. Less is known about the mechanical properties of the

interface between the substrate and deposited DED material as prior studies have focused on the mechanical properties of the printed material.

Methodology and Materials

The DED process is carried out using a UMC750HAAS 5-axis vertical milling machine retrofitted with an AMBIT Series 7 laser deposition head developed by Hybrid Manufacturing Technologies that is used to build the samples for the current work. The schematic of DED process is shown in Figure 1A. The direct energy deposition head, Figure 2A, includes a laser beam and coaxial gas-powder. Samples are printed under an argon gas environment to protect the melt pool from atmospheric gases. The DED utilizes the laser beam head to move towards the substrate and generate a melt pool where a stream of metal powder is continuously blown into the melt pool to create a metallurgical bond between the substrate and new material, and build up a bead. The nozzle moves on top of the substrate and convert the 3D digital data into a desired physical part, by depositing material layer by layer.

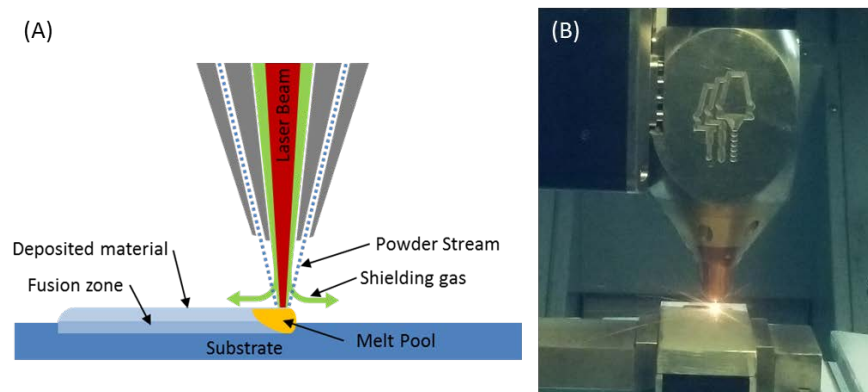


Figure 1- (A) Schematic of experimental set-up and DED machine that is depositing layers; (B) AMBIT Series 7 laser based DED head.

The AMBIT system includes the laser, shielding gas delivery and powder feeding system. Figure 2 shows the powder feeding mechanism. The powder feeding system consists of the

powder chamber, feeding disk, carrier gas supplier and feeding channel. As seen in the Figure 2B, there is a groove on the feeding disk that carries particles from the chamber to powder supplier. Gravity force causes the particles to move from chamber to the groove of the disk. The amount of particles that feed in the disk is constant. The disk rotates and transports the powder to the powder supplier. The gas flow causes the movement of the particles from the disk groove to the deposition area.

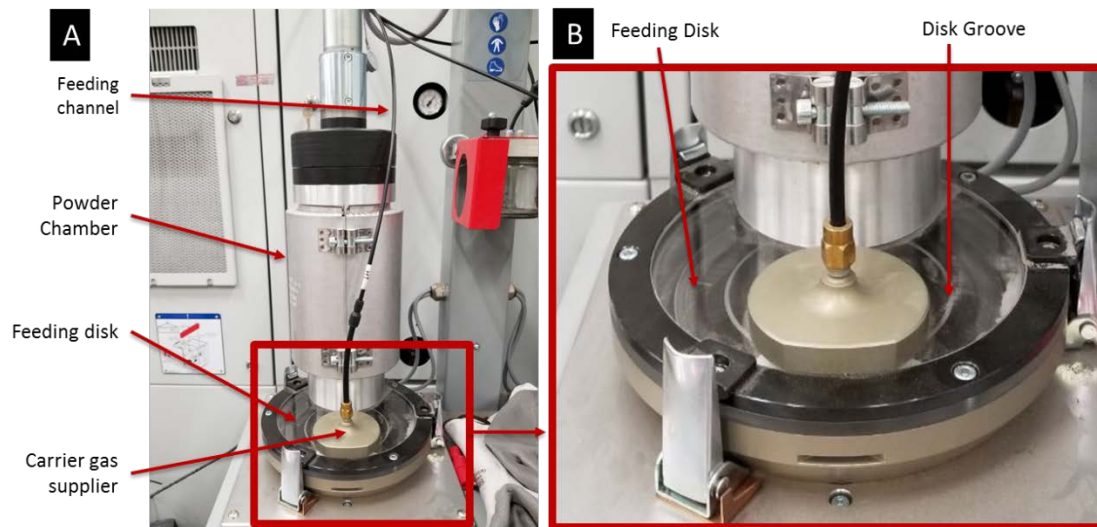


Figure 2- (A) Powder feeding system and (B) Feeding disk.

Both the substrate material and the powder selected for DED process is 316L stainless steel, due to its high corrosion resistance in comparison with other types of stainless steel, and good weldability in part because of its relatively low carbon content. The powder was purchased as LPW-316-AAAW from LPW Technology Inc. The particle size is between 45 to 90 μm and its chemical composition is shown in Table 1. Figure 3 illustrates a scanning electron microscopy (SEM) of powder sample, showing that the particles are generally spherical with attached smaller satellite particles.

Table1- Chemical composition of 316L stainless steel for the substrate and powder

Material Composition	Substrate (wt.%)	Powder (wt.%)
Iron	58.23-73.61	58.23-73.61
Carbon	0-0.08	0-0.03
Chromium	16-18.5	16-18.5
Copper	0-1	0-0.75
Manganese	0-2	0-2
Molybdenum	0-3	2-3
Nickel	10-15	10-14
Nitrogen	0-0.1	0-0.2
Phosphorus	0-0.045	0-0.045
Silicon	0-1	0-0.75
Sulfur	0.35	0-0.015

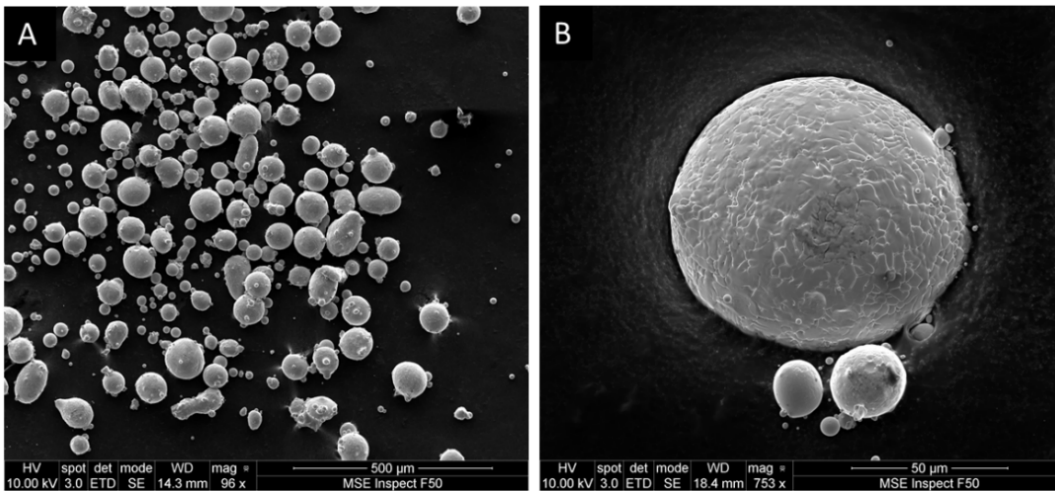


Figure 3- Scanning electron microscopy (SEM) of powder sample.

To prevent the formation of porosity and minimize the effect of porosity on the interfacial strength, specific rastering strategies are utilized in this work. The first rastering strategy that was

chosen is the perpendicular rastering in which the deposition direction of the following layer is perpendicular to the previous one, as shown schematically in Figure 4A. To measure and evaluate the amount of porosity within the parts, the sample is cut, polished, and observed under the optical microscope. In some samples, porosity was observed. It was noticed that at some specific cross sections it is hard to observe porosity. For example, if polishing stopped at cross section A-A (Figure 4B), the porosity is not detected as seen in Figure 4C, however if polishing process continues to remove more material the porosity gradually becomes visible, so that at cross section B-B (Figure 4B) the maximum porosity population is observed, as shown in Figure 4D. Therefore, the detection of the porosity depends on the amount of polishing as well as the cutting direction of the cross section. Hence, the authors propose the cutting angle of 45° with respect to the first deposition direction. At cross section of 45° , the porosity can be detected regardless of the amount of polishing. The investigation of porosity at cross section of 45° demonstrated that the perpendicular rastering strategy is not suitable for eliminating the porosity. After several trials, the parallel deposition rastering strategy was chosen to avoid the formation of porosity between the layers of the deposited material. Figure 5 shows the schematic and microstructure of the parallel deposition strategy that is used in this study. The top view and side view of the rastering strategy are shown in Figures 5A and 5B, respectively. Figure 5C illustrates the optical microscopy image of the sample deposited using parallel strategy, in which no porosity is observed.

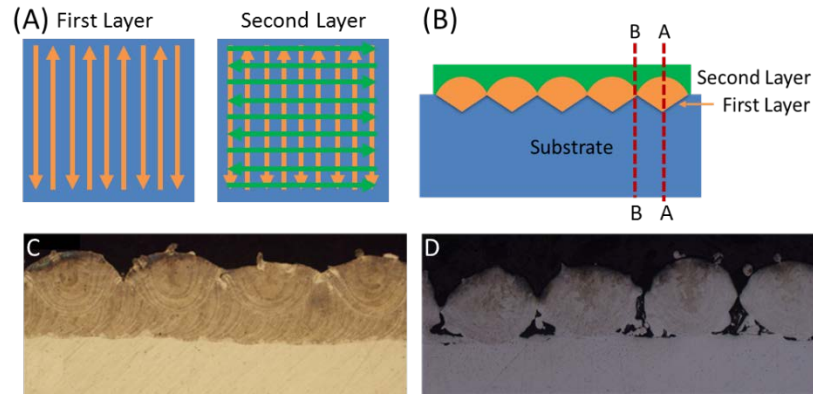


Figure 4- (A) Schematic of the perpendicular rastering strategy; (B) cross section view of perpendicular to the first layer deposition direction; Optical microscopy image of the sample in cross sections A-A (C), and B-B (D).

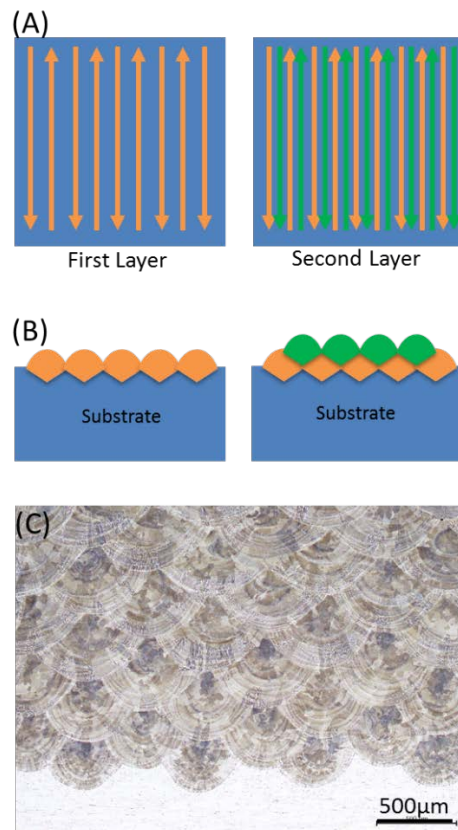


Figure 5- Schematic of the parallel rastering strategy (A) top view and (B) side view; (C) Optical microscopy image of the sample deposited using parallel strategy; no porosity was observed.

To evaluate the shear strength of substrate/deposited interface, the block shear test is conducted at room temperature and displacement rate of 1 mm/min, using a Shimadzu UH-300KNX tensile test machine. The block shear test specimen for AM part consisted of the substrate with dimensions of $50.8 \times 50.8 \times 12.7$ mm, and the printed volume with dimensions of $25.4 \times 6.35 \times 3.18$ mm. Figure 6 shows the schematic and dimensions of the block shear test specimen manufactured by DED process. A fixture is designed specifically for this work to accommodate the test specimen with the above-mentioned dimensions. The fixture consisted of two detachable parts, body and back plate that are shown in Figure 7A. The distance between the fixture body and back plate can be adjusted by using screws. Figure 7B shows the block shear testing setup, in which the specimen is placed in the fixture.

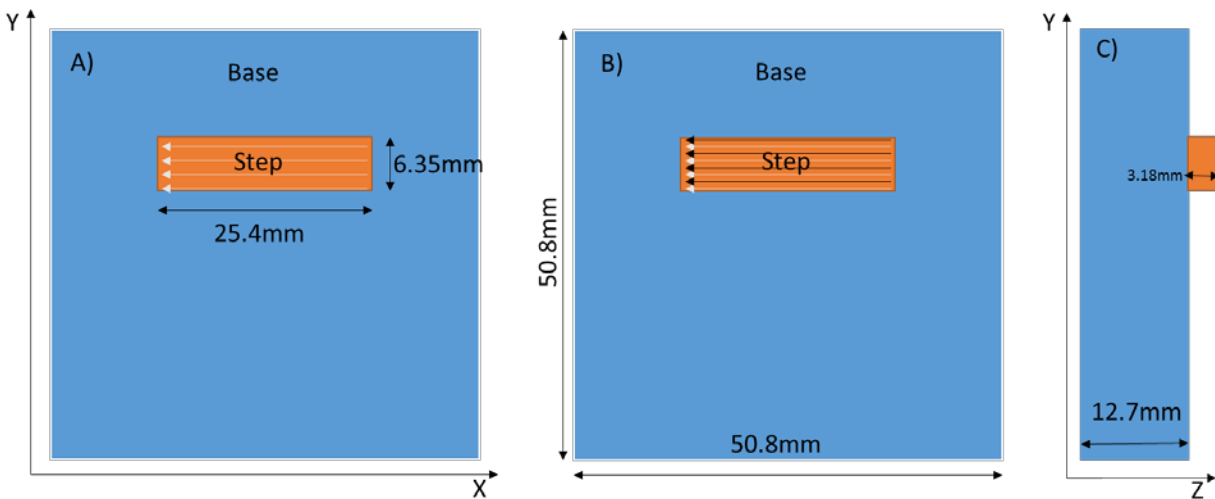


Figure 6- Schematic and dimensions of the block shear test samples.

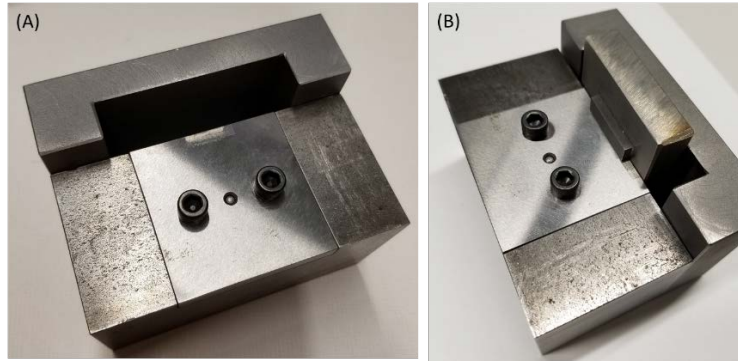


Figure 7- Block shear testing A) Fixture and B) setup.

To investigate the effect of DED process parameters on the strength of the interface, three levels of scanning speed and powder feed rate and two levels of laser power are considered. The scanning speed is directly determined by the speed of the CNC head that is introduced to the CNC with G-code. The laser power is determined directly by the process recipe. The recipe is defined in the G-Code, and the operator defines each recipe. The recipes include the laser power, the gas flow and the percentages of the maximum rotation rate of the powder disk, Figure 8.

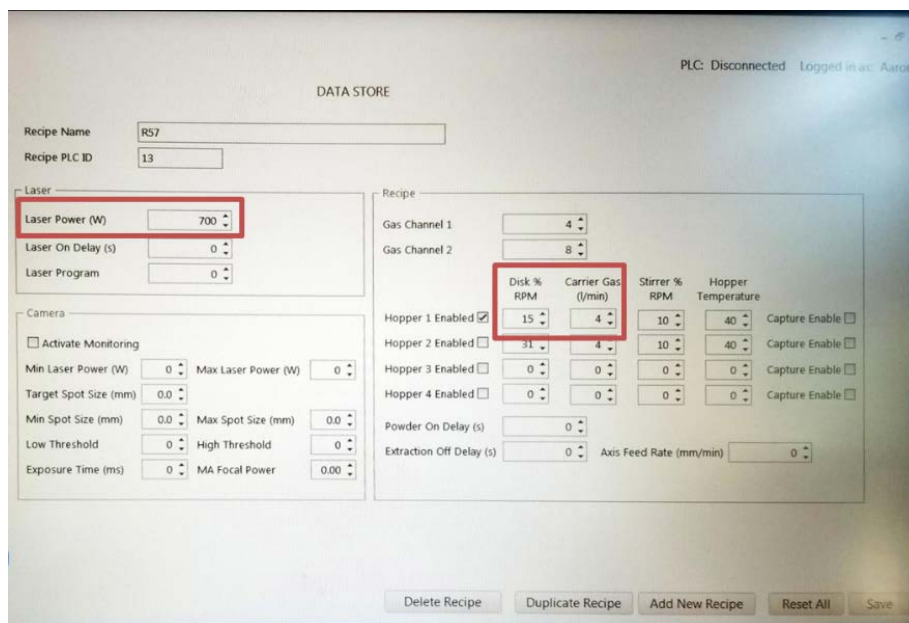


Figure 8- Recipe display on the machine

In theory, the powder feed rate depends on the disk rotation and can be expressed as,

$$F_{theory} = v_{groove} \times Disk\ RPM \times \rho_{powder}$$

$$Disk\ RPM = Disk\% \ RPM \times Motor\ RPM$$

where v_{groove} is the volume of the feeding disk groove, and ρ_{powder} is the density of the powder.

To measure the powder feed rate, different experiments with different recipes were conducted to determine the relationship between recipe variables (gas flow, Disk% RPM) and the powder feed rate. Figure 9A shows the relationship between gas flow and powder feed rate. As shown, with increasing gas flow the powder feed rate increases. However, there is a limitation for powder feed rate. It can be concluded that in the gas flow below a threshold, the gas flow is not sufficient to carry all powder particles that provided by the rotational disk. At the threshold point all the powder particles are carried from rotational disk to the deposition area. Therefore, with increasing gas flow beyond the threshold, the powder feed rate would be a constant because there are no more powder particles. Figure 9B Shows a linear relationship between Disk% RPM with powder feed rate.

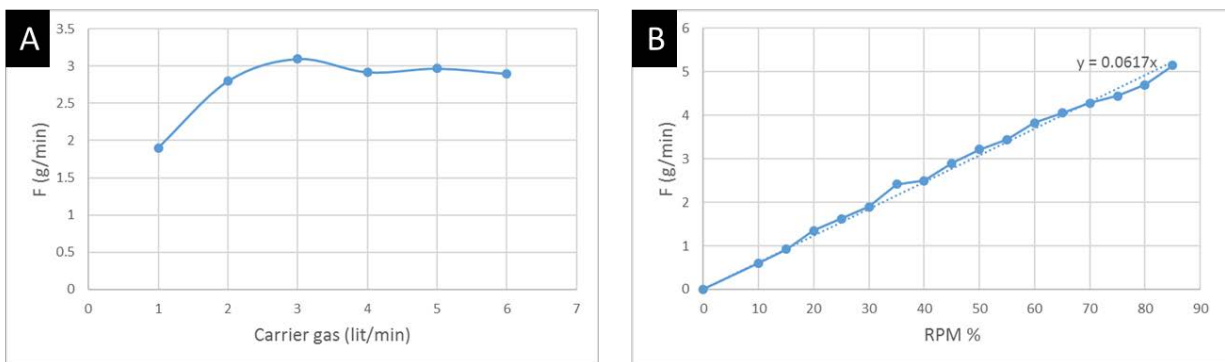


Figure 9- (A) Relationship between carrier gas flow with powder feed rate; (B) Relationship between disk %RPM with powder feed rate.

Several experiments were carried out to determine the desirable range of variables to deposit samples with no porosity. To prevent the porosity formation, the undercut in a single bead geometry should be avoided. , the contact angle should be greater than 90 degree. The contact angle greater than 90 degree causes the bead to spread on the surface, resulting in filling the gap between adjacent beads. The undercut can cause the lack of fusion and consequently formation of porosity in the DED manufactured parts. Figure 10 shows a single bead where H is the bead height, D is depth, W is bead width and θ is contact angle. The preliminary experiments were conducted using three levels of the parameters, including the scanning speed of 200, 600, 1000 mm/min, feeding Disk RPM of 15, 45, 75% and laser power of 100, 400 and 700 W. The results of these experiments are shown in Table 2. As seen, the laser power of 100 W is not strong enough to melt the substrate and as a result no deposition occurs. The contact angle of the beads at different process parameters are shown in Table 2. The beads with contact angles less than 90 degree are shown with red boxes as they were not acceptable. Based on these preliminary results, for this study, three levels of scanning speed were chosen, including 350, 500, 650 mm/min, three levels of feeding disk RPM, including 15%, 30%, and 45%, and two levels of laser power, including 300 and 500 W. The carrier gas was kept constant at 4 lit/min for all the experiments. Table 3 shows the process parameters proposed for this study. Eighteen samples were manufactured using each combination of scanning speed, laser power and powder feed rate.

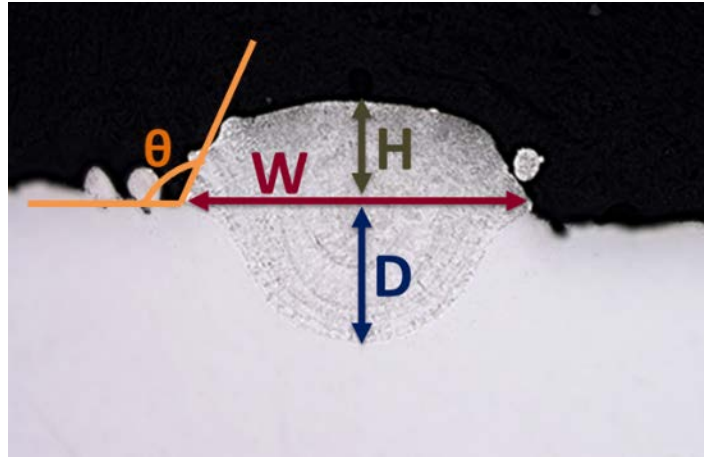


Figure 10- The geometry of a single bead where H is the bead height, D is depth, W is bead width and θ is contact angle.

Table 2- The geometry of the beads deposited in different process promoters

Laser Power (W)		100			400			700		
Scanning Speed (mm/min)		1000	600	200	1000	600	200	1000	600	200
Feeding Disk RPM (%)	15				150°	135°	126°	159°	148°	130°
	45				101°	93°	69°	107°	98°	83°
	75				106°	85°	49°	116°	87°	60°

Table 3- Sample number, laser power, scanning speed, and powder feed rate

	Samples	P (W)	V (mm/min)	F (g/min)
1	P500-V650-F3	500	650	3
2	P500-V650-F2	500	650	2
3	P500-V650-F1	500	650	1
4	P500-V500-F3	500	500	3
5	P500-V500-F2	500	500	2
6	P500-V500-F1	500	500	1
7	P500-V350-F3	500	350	3
8	P500-V350-F2	500	350	2
9	P500-V350-F1	500	350	1
10	P300-V650-F3	300	650	3
11	P300-V650-F2	300	650	2
12	P300-V650-F1	300	650	1
13	P300-V500-F3	300	500	3
14	P300-V500-F2	300	500	2
15	P300-V500-F1	300	500	1
16	P300-V350-F3	300	350	3
17	P300-V350-F2	300	350	2
18	P300-V350-F1	300	350	1

Catchment efficiency is a parameter that is used for the heat transfer and energy balance calculations. Catchment efficiency is defined as the mass of the deposited part divided by the total mass delivered to make the part. It can be accurately determined by weighing the substrate before deposition, and weighing the sample after deposition. The efficiency β can then be calculated as,

$$\beta = \frac{\text{weight of final component} - \text{weight of substrate}}{\text{weight of consumed powder}}$$

The amount of powder consumed for each recipe is obtained by activating the Capture Enable option in each recipe. In this mode, the machine starts collecting powder in a jar instead of depositing it on the substrate. Then the powder collected in the jar is weighed.

The microstructure characterization of the deposited part was examined by optical microscopy. To prepare the metallography specimen, the part is cut in transverse direction and then mounted in epoxy to facilitate handling. Grinding and polishing is performed to reach a final diamond grit size of 1 μm to achieve a reflective surface absence of machining marks. To reveal the microstructure, the samples were chemically etched in a methanolic aqua regia (45 ml HCL, 15 ml HNO_3 and 10 ml methanol) for 2 minutes. Microstructure observations were carried out using Leco LX31 optical microscope.

Results and Discussion

Figure 11 illustrates the variation of average yield strength obtained from three measurements for all samples varying with process parameters. The Y-axis has been sorted in three levels of laser power, scanning speed and powder feed rate, respectively. As seen, at constant scanning speed and powder feed rate, with increasing laser power the yield strength decreases. Generally, Figure 11 shows that yield strength has a direct correlation with scanning speed, however it is inversely proportional to the laser power and powder feed rate. The analysis of variance (ANOVA) is developed using R to identify interactions between the process parameters and significant factors. The analysis of variance and significant factors identified by ANOVA are listed in Table 4. P-values less than 0.05 is used to determine the significance of a factor. It can be concluded from Table 4 that laser power, scanning speed, and powder feed rate are significant factors for yield strength, however, secondary interactions of these parameters are not significant for yield strength.

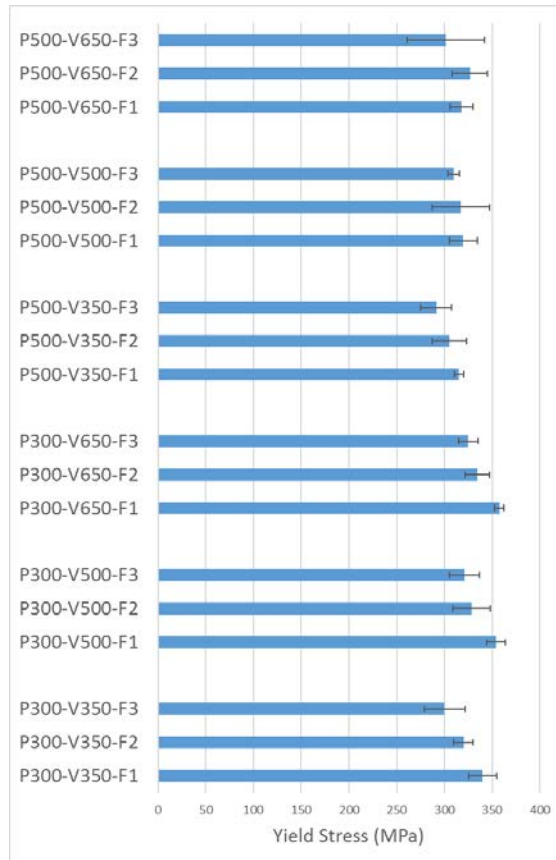


Figure 11 - The variation of average yield strength at different process parameters, including laser power, scanning speed and powder feed rate.

Table 4- Analysis of variance (ANOVA) of Yield Strength

Factor	Degree of freedom	Sum of Squares	Mean Square	F value	P	Significance
P	1	6609	6609	20.53	0.00006	Very high
V	2	2158	1079	3.35	0.0468	Relatively high
F	2	6855	3427	10.65	0.0002	Very high
P:V	2	547	273	0.85	0.4361	
P:F	2	969	484	1.50	0.2362	
V:F	4	357	89	0.27	0.8905	
P:V:F	4	331	82	0.25	0.9029	
Residuals	34	10940	321			

In order to analyze the effects of process parameters on strength of interface, first it is required to determine the fundamental phenomena that affect the strength. The strength of the interface is expected to be highly affected by porosity and microstructure. To investigate the

yield strength, the block shear test is conducted. The microstructural characterization is completed to analyze the occurrence of porosity and microstructure of the DED parts. The metallography results detected no porosity in the parts built by DED. Thus, the only factors that can influence the strength of the interface is microstructure and grain morphology.

The experimental investigation indicates key insights into the influence of process parameters on microstructural characteristics of the parts. The morphology and size of the grains are affected by thermal history and melt pool cooling rate, which depend on melt pool geometry. In addition, depth and width of the melt pool determine the melt pool geometry, which is dictated by process parameters. It can be concluded that process parameters determine the cooling rate and consequently, the grain size and morphology of the interface. According to Hall-Petch equation, there is a relationship between grain size and the strength of the part. So, grain size can be generally used to control the strength of the interface. Figure 12 shows the procedure that can illuminate the relationship between process parameters and strength of interface.

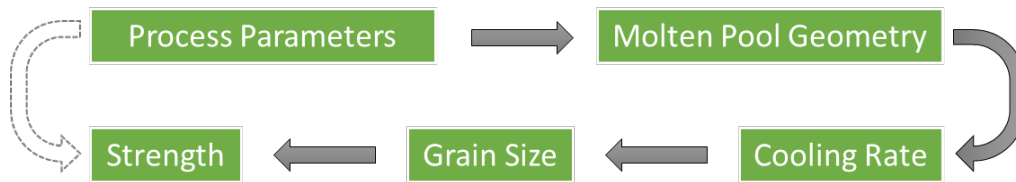


Figure 12- Hypothetical chain relationship between process parameters and interfacial strength.

Microstructure

Figure 13 shows the optical image of the DED part produced at laser power of 300 W, scanning speed of 350 mm/min, and powder feed rate of 1 g/min. In order to observe the microstructure, the sample was cross section and then ground, polished and etched. An example of a multilayer DED sample using the above-mentioned process parameters is shown in Figure

13A. In Figure 13B the typical deposition structure of beads can be seen; also note the absence of porosity. . The boundary of deposited material and morphological differences observed in microstructure of the substrate and deposited material depicted at higher magnification in Figure 13C, which will be discussed in the following sections.

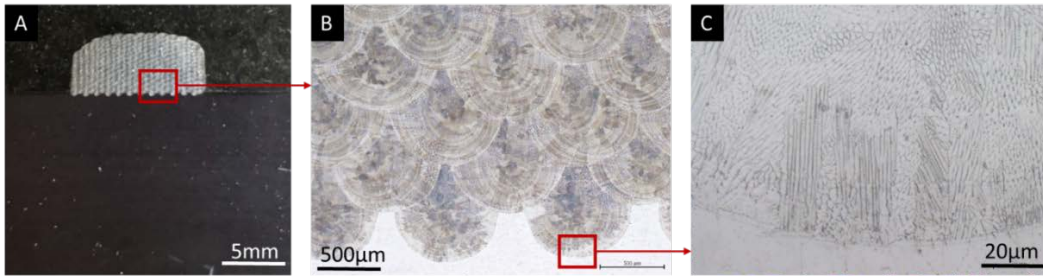


Figure 13- Optical microscopy of (A) multilayer DED sample; (B) deposition structure of beads; and (C) microstructure features of the substrate and deposited material.

Fundamentally, the microstructure evolution during DED process relies on thermal process of the melt pool such as rapid heating, melting, and rapid cooling. In general, the grain size and morphology of a DED part is determined by several parameters, particularly the thermal gradient, and the heating and cooling rate. A solidification map is constructed to relate the microstructure to the temperature gradient (G), and the solidification rate (R), Figure 14. Solidification rate is defined as the ratio of the cooling rate over the temperature gradient. In this map, the combined forms of $G \times R$ and G/R are found to be the most critical parameters that determine the size and the morphology of the microstructure at the liquid/solid interface, respectively [17]. As seen in Figure 14, depending on the local values of G and R , different solidification structures can be formed, including planar, cellular, columnar dendritic, and equiaxed dendritic. The solidification map with known values of G and R enables the ability to achieve the desired microstructure and mechanical properties in parts built via DED.

Various heat transfer mechanisms and consequently the local variations of cooling rate in different zones of melt pool result in different microstructural features in part produced via DED.

At the melt pool boundary, the conduction heat transfer mechanism dominates, while in the center of the melt pool, the convection heat transfer mechanism is often the main mechanism. Figure 15 shows the general optical microscope images of the 316L stainless steel produced by DED. The process parameters for the sample illustrated in Figure 15 are laser power of 500 W, scanning speed of 350 mm/min, and powder feed rate of 3 g/min. However, Figure 15 demonstrates the typical microstructure morphology that was observed. The first characteristic that is clearly visible in the Figure 15A is the curved boundary of the melt pool, which is induced by the Gaussian distribution of laser energy. At some regions in the melt pool boundary, Figure 15B, the planar structure is dominant, due to the high G/R ratio at the solidification interface. Also visible in the Figure 15 is the cellular structure of the grains as a results of the relatively high ratio of G/R that provides the growth of cellular subgrains. Directional growth of the grains illustrates an elongated morphology that starts from the melt pool boundary and drug into the center of the melt pool. The possible reason for this observation is the steep temperature gradient in the direction perpendicular to the melt pool boundary that leads to the formation of the cellular structure. Both Figures 15C and 15D demonstrate the cellular subgrains, but different growth orientation. In 2D cross section view, from the melt pool boundary to the center of melt pool the growth direction is perpendicular to the deposition orientation, however, in the center of the melt pool the grain growth occurs in the direction parallel to the deposition direction. Considering the 3D geometry of the melt pool, this is the reason that the different morphology for cellular structure is seen in Figure 15. To better illustrate the growth orientation in the cellular structure, three dimensional views of the microstructure are shown in Figures 15E and 15F.

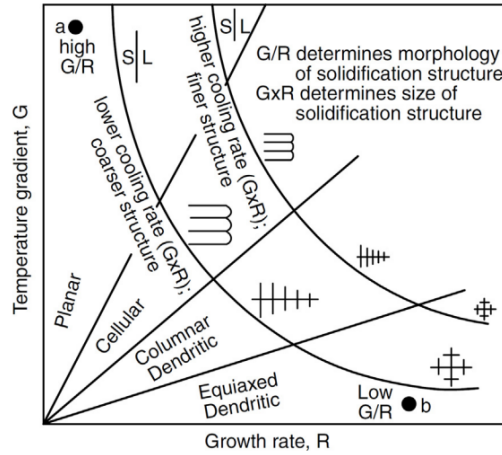


Figure 14- Solidification map showing the influence of thermal gradient (G) and solidification rate (R) on the size and morphology of the solidification structure [17].

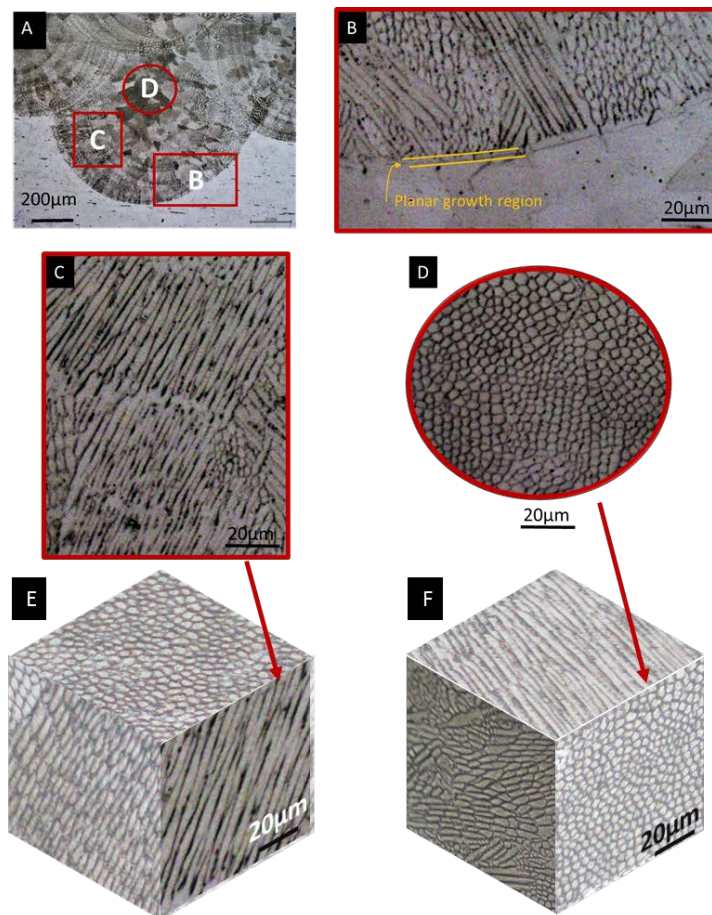


Figure 15- Optical microscope images of the 316L stainless steel produced by DED showing (A) the curved boundary of melt pool; (B) planar structure; (C) and (D) cellular subgrains growing in different orientations; (E) and (F) 3 dimensional views of the microstructure to illustrate growth dimension.

In order to analyze the microstructural evolution of the DED material, it is necessary to clearly define the solidification behavior under the DED processing conditions. Figure 16 illustrates the epitaxial nucleation and preferred cellular growth. There are two types of solidification nucleation: homogenous and heterogeneous [18]. In DED process (as with most welding processes), heterogeneous nucleation completely dominates the homogenous nucleation, and nucleation occurs from the solid-liquid interface. The epitaxial nucleation which is the dominant form of nucleation in welding, is defined as the heterogeneous nucleation that grow from substrate. The epitaxial nucleation occurs without any driving force. Consequently, once the temperature drops below the liquid temperature the solidification begins at the melt pool boundary and creates solidification front. In fact, the melt pool boundary acts as an active nucleation spot for newly formed grains. Then, the solidification front grows toward the inside of the melt pool and forms the cellular structure. Since the crystallization is initiated from a nuclei on the substrate, the newly formed grains continue to grow with the same crystallographic orientation as the substrate grains, and maintain the same degree of crystallographic misorientation into the solidifying zone, Figure 16B. As a result, a continuous grain boundary is seen across the fusion zone. As seen in Figure 16C, the substrate grains in polycrystalline metals are revealed and shows random crystallographic orientations in the microstructure.

In FCC metals, the preferential solidification growth or the most efficient solidification occurs along the $\langle 100 \rangle$ crystallographic directions [18]. This is also known as easy growth direction. The solidification behavior of the melt pool mainly depends on the solidification parameters, including the temperature gradient (G), solidification rate (R), and $G \times R$. The most favorable direction for grain growth is the direction parallel to the thermal gradient vector, which is perpendicular to the solid/liquid interface. At the initial stage of solidification, there is a

competition between grains to grow to the interior of the melt pool. In the direction perpendicular to the melt pool boundary, the thermal gradient is intense, and grains that their favorite orientations are parallel to the temperature gradient direction continue to grow faster to the interior of fusion zone and as a result these grains win the competition. However, the grains which are growing along the $\langle 100 \rangle$ direction but the favored orientation is less parallel to the temperature gradient at the solid/liquid interface are inhibited and their growth is terminated after a short distance. Consequently, near the melt pool boundary, small grains are formed. This phenomenon is defined as competitive growth, and the boundaries that are formed between these grains are called solidification grain boundaries (SGB).

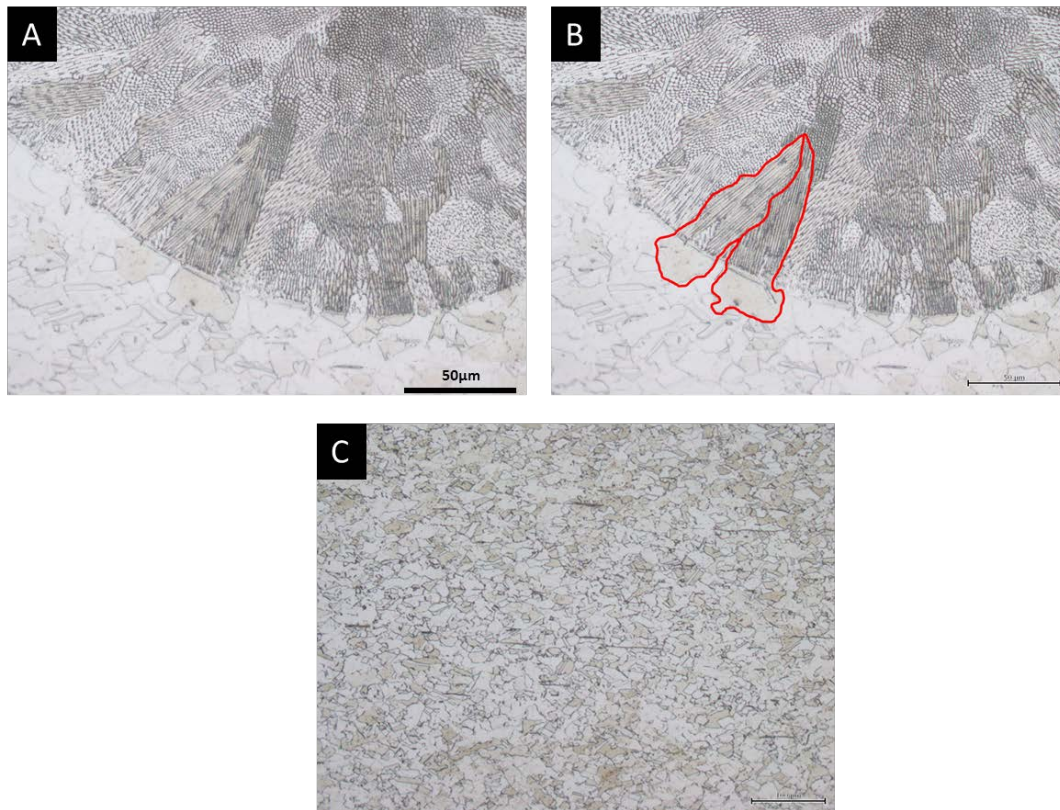


Figure 16- (A) and (B) the epitaxial nucleation and preferred cellular growth; (C) the microstructure of the substrate.

Heat Transfer

In order to understand the influence of process parameters on cooling rate, a thermal analysis is used to determine the relationship between melt pool shape and geometry with cooling rate. To understand the thermal behavior, the heat transfer that occurs between the molten pool, the substrate, and the surrounding environment was modeled. The powders are first melted by the focused heat source and the metallurgical bond is formed between the deposited material and the substrate. The rate of heat transfer from the laser beam to the melt pool depends on absorptivity of 316L stainless steel (α_λ), and the laser power (P) that can be expressed as,

$$\dot{q}_{in} = \alpha_\lambda P \quad (1)$$

The energy enters to the system is absorbed by the substrate, or lost due to convection, and radiation, or used to create the melt pool and melt the deposited powders [19]. Thus,

$$\dot{q}_{in} = \dot{q}_m + \dot{q}_{conv} + \dot{q}_{rad} + \dot{q}_{cond} \quad (2)$$

The energy that is used to heat the substrate and create the melt pool, and melt the incoming powders is expressed as,

$$\dot{q}_m = A_s V \rho \left(\int_{T_0}^{T_m} C_s dT + \Delta H_f + \int_{T_m}^T C_l dT \right) + \beta F \left(\int_{T_0}^{T_m} C_s dT + \Delta H_f + \int_{T_m}^T C_l dT \right) \quad (3)$$

where A_s is the molten substrate cross sectional area perpendicular to the deposition direction, V is the scanning speed (m/s^2), ρ is the density of the substrate (kg/m^3), C_s is the specific heat of solid (J/kg.K), C_l is the specific heat of liquid, ΔH_f is the latent heat of fusion of the clad (J/kg), F is the powder feed rate, T_0 is the temperature of the surrounding environment, T_m is the melting temperature (K), T is the temperature of the melt pool (K). The first term in the right

hand side of Equation 3 represents the energy that is needed to melt the substrate material and create melt pool. The second term represents the amount of energy needed for melting new powders that enter the melt pool and create the deposition track. Latent energy is the energy that is either absorbed or released by the material to change the physical state without changing its temperature.

Convection heat transfer occurs between a surface and a fluid flowing above the surface with different temperature. In this experiment, the DED process is shielded by a closed chamber filled with argon gas to produce high-quality parts. The estimated heat transfer loss in the molten pool occurs by convection can be obtained as,

$$\dot{q}_{conv} = hS_d(T - T_0) \quad (4)$$

here, h is convection coefficient of the argon gas ($\text{W}/\text{m}^2\text{K}$), and S_d is the surface area of the deposited material (m^2). Some portion of the laser energy input to the melt pool is lost by radiation from the melt pool surface. Thus, by applying Stefan-Boltzman's rule, the radiation is approximated as,

$$\dot{q}_{rad} = S_d \varepsilon \sigma (T^4 - T_0^4) \quad (5)$$

where, ε is the emissivity of the melt pool surface, and σ is the Stephan-Boltzmann constant ($\text{W}/\text{m}^2\text{K}^4$).

Some portion of the laser beam energy is absorbed by the substrate through conduction. The rate of conduction heat transfer is expressed as,

$$\dot{q}_{cond} = -k\nabla T = -k \left\{ \frac{\partial T}{\partial x} i + \frac{\partial T}{\partial y} j + \frac{\partial T}{\partial z} k \right\} \quad (6)$$

where k is thermal conductivity of the material (W/mK), and ∇T is temperature gradient.

Considering the above-mentioned equations for heat input and heat losses, the overall energy balance equation for this system can be expressed as,

$$\dot{q}_{in} = A_s V \rho \left(\int_{T_0}^{T_m} C_s dT + \Delta H_f + \int_{T_m}^T C_l dT \right) + \beta F \left(\int_{T_0}^{T_m} C_s dT + \Delta H_f + \int_{T_m}^T C_l dT \right) + h S_d (T - T_0) + S_d \varepsilon \sigma (T^4 - T_0^4) - k \nabla T \quad (7)$$

A sample thermal analysis is performed for one of the samples built with a laser power of 300 W, scanning speed of 350 mm/min, and powder feed rate of 1 gr/min. The thermo-physical properties of 316L stainless steel and the heat transfer constants that were used for the thermal analysis are listed in Table 5. The temperature of the melt pool is considered 2000 K [20]. For this sample, A_s and β were measured as 0.14 mm² and 0.27, respectively. Thus, the energy used for creating melt pool and deposition (the first term in the right hand side of Equation 7) is calculated to be 12 W. Considering the hemispherical model for molten pool gives S_d 0.77 mm², thus the energy loss through radiation from the melt pool surface is estimated about 0.5 W. In DED, argon is used as the shielding gas for the melt pool and as a carrier gas for the metal powder. For this system, the heat transfer coefficient is in the order of 10³ W/m²K [21], so the energy lost due to convection through the gas flow is then estimated about 1.5 W. For this experiment, the rate of heat entering the system from Equation 1 is 102 W, where the absorptivity of 316L stainless steel is 34% [22]. For this example, the calculations show that more than 85% of the total input energy is absorbed by substrate through conduction. This analysis demonstrates that in the molten pool, heat transfer due to conduction is more significant as compared to the radiation and convection losses.

Table 5- Thermo-physical properties of 316L stainless steel [19], [23], [24]

Symbol	Property and unit	Value
ρ	Density (kg/m ³)	8000
C_s	Specific heat of solid (J/Kg K)	$460 + 0.14T$
ΔH_f	Latent heat of fusion (J/Kg)	2.6×10^5
C_l	Specific heat of liquid (J/Kg K)	710
T	Ambient Temperature (K)	300
ε	emissivity	0.54
σ	Stefan-Boltzman's constant (W/m ² K ⁴)	5.67×10^{-8}

As the laser beam moves away from the molten pool, cooling occurs and solidification of the fusion zone begins at the melt pool boundary. This occurs mainly by dissipation of the heat through the substrate due to conduction. Figure 17 shows the cross section of a bead deposited at laser power of 500 W, scanning speed of 500 mm/min, and powder feed rate of 3 g/min, in which the melt pool boundary can be clearly observed. The maximum heat transfer occurs in the direction perpendicular to the melt pool boundary [18]. Thus, the solidification and consequently the grain growth occur in the opposite direction of thermal gradient toward the center of the melt pool.

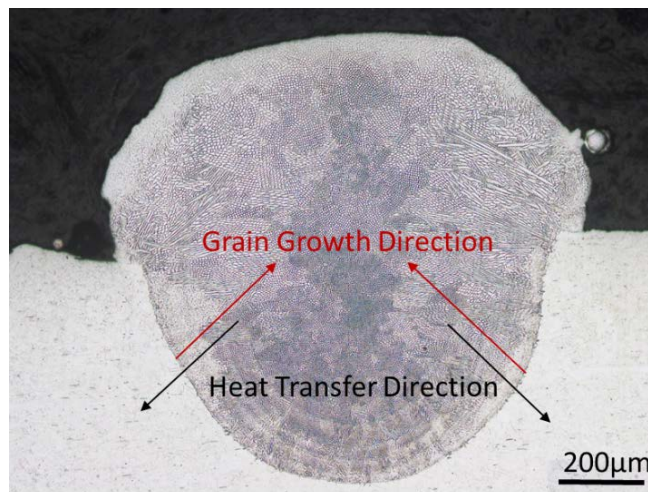


Figure 17- The cross section of a deposited bead showing the melt pool boundary, the heat transfer direction, and the grain growth direction.

The heat balance in the solidification front of the melt pool can be expressed as,

$$Q_{cond} = Q_{\Delta\theta_l} + Q_{l \rightarrow s} \quad (8)$$

where, $Q_{\Delta\theta_l}$ is the amount of heat transfer that results in temperature change in the melt pool, and

$Q_{l \rightarrow s}$ is the amount of energy released by the melt pool for solidification.

$$Q_{cond} = m_l C_l \Delta T + m_{l \rightarrow s} \Delta H_f \quad (9)$$

here, m_l and $m_{l \rightarrow s}$ are the mass of molten pool and solidified region, respectively, and ΔT is the reduction of melt pool temperature. In order to obtain the heat rate balance, the time derivative of both sides of the Equation 9 is determined. Since the melt pool mass is much greater than the mass of the solidified material, the variation of melt pool mass with time is assumed to be constant.

$$\dot{q}_{cond} = m_l C_l \frac{dT}{dt} + \dot{m}_{l \rightarrow s} \Delta H_f \quad (10)$$

$$\dot{q}_{cond} = V_{mp} \rho C_l \frac{dT}{dt} + S_{mp} \frac{dr}{dt} \rho \Delta H_f \quad (11)$$

where, V_{mp} is the melt pool volume, $\frac{dT}{dt}$ is the cooling rate of melt pool, S_{mp} is the surface area of the melt pool/ substrate interface, dr is the solidified layer, $\frac{dr}{dt}$ is defined as solidification rate that is known by R [18]. The rate of conduction heat transfer is calculated by applying Fourier's law as,

$$\dot{q}_{cond} = \frac{k S_{mp} (T_m - T_0)}{d} \quad (12)$$

where k is thermal conductivity of the material (W/mK), and d is the distance between two isothermal surfaces with temperatures of T_m and T_0 .

$$\frac{kS_{mp}(T_m - T_0)}{d} = V_{mp}\rho C_l \frac{dT}{dt} + S_{mp}R\rho\Delta H_f \quad (13)$$

$$\frac{dT}{dt} = \frac{1}{V_{mp}\rho C_l} \left(\frac{kS_{mp}(T_m - T_0)}{d} - S_{mp}R\rho\Delta H_f \right) \quad (14)$$

$$\dot{T} = \left(\frac{S_{mp}}{V_{mp}} \right) \left[\frac{1}{\rho C_l} \left(\frac{k(T_m - T_0)}{d} - R\rho\Delta H_f \right) \right] \quad (15)$$

Cooling rate for a thin layer of the melt pool with thickness of dl can be given by,

$$\dot{T} = \left(\frac{B_{mp} \times dl}{A_{mp} \times dl} \right) \left[\frac{1}{\rho C_l} \left(\frac{k(T_m - T_0)}{d} - R\rho\Delta H_f \right) \right] \quad (16)$$

By solving the heat balance equation for a thin layer of melt pool, the problem is simplified from a 3D to a 2D problem.

$$\dot{T} = \left(\frac{B_{mp}}{A_{mp}} \right) \left[\frac{1}{\rho C_l} \left(\frac{k(T_m - T_0)}{d} - R\rho\Delta H_f \right) \right] \quad (17)$$

where, B_{mp} is the melt pool boundary, and A_{mp} is the area of melt pool in 2D problem, which are shown in Figure 18. This equation shows that cooling rate is proportional to the ratio of melt pool boundary to melt pool area.

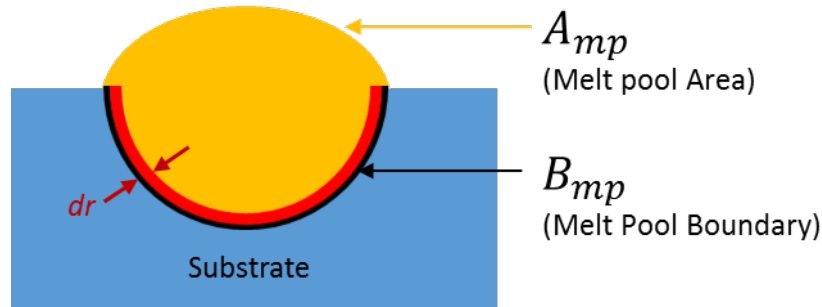


Figure 18- The schematic of melt pool showing the melt pool boundary (B_{mp}), and melt pool area (A_{mp}).

The heat in the melt pool released from the boundary of the melt pool to the substrate, and the ratio of the melt pool boundary to area gives an approximation of the cooling rate. A larger $\frac{B_{mp}}{A_{mp}}$ results in a higher cooling rate and faster heat transfer to the substrate. As a result, by measuring the ratio of melt pool boundary to melt pool area, it is possible to compare the solidification condition at different process parameters. The melt pool area consists of two different areas, including deposited area (A_d) and molten substrate area (A_s) as seen in Figure 19A and can be expressed as,

$$A_{mp} = A_d + A_s \quad (18)$$

A_d is calculated directly from powder catchment efficiency (β), and process parameters, including powder feed rate (F), and scanning speed (V) as,

$$A_d = \frac{\beta F}{\rho V} \quad (19)$$

With assuming the molten substrate has a parabolic geometry [25], the molten substrate area and melt pool boundary can be calculated using a single track width (w) and depth (d), which are shown in Figure 19B.

$$A_s = \frac{2}{3} wd \quad (20)$$

$$B_{mp} = \frac{1}{2} \sqrt{w^2 + 16d^2} + \frac{w^2}{8d} \ln \left(\frac{4d + \sqrt{w^2 + 16d^2}}{w} \right) \quad (21)$$

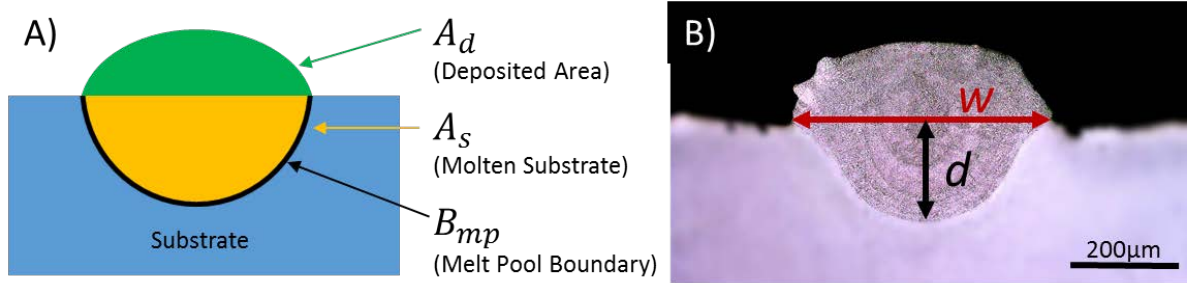


Figure 19- (A) Schematic of the melt pool showing the deposited area (A_d) and molten substrate area (A_s); (B) optical microscopy of the bead that shows the width and depth of the melt pool.

Figure 20A shows the variation of the melt pool dimensions with process parameters at different levels. The variance analysis, Table 6, allows us to find out the influencing significance of each parameter on experimental results. As seen from the figure and variance analysis table, the laser power has a significant effect on the bead width and height. By comparison, the scanning speed exhibits a relatively high influence on bead width and low influence on bead depth. Thus, the influence of scanning speed on the bead width is more remarkable than that on the bead depth. In addition, the influence degree of powder feed rate on bead width and depth is low. Since the beam spot has a constant value of 1 mm and the distribution of laser beam is Gaussian, the increase in laser power leads to an increase in beam intensity, causing more substrate material to melt and as a result, the melt pool penetration depth increases. In addition, with increasing laser power and decreasing scanning speed, the energy density per unit length increases, leading to a larger melt pool size and consequently an increase in the melt pool width.

Figure 20B shows the results of powder catchment efficiency with varying process parameters. Through the variance analysis Table 6, it can be concluded that laser power has the most significant influence on catchment efficiency. By comparison, scanning speed and powder feed rate exhibit the less influence on the catchment efficiency. Namely, the change of

catchment efficiency is more sensitive to laser power than that of the other two parameters. With increasing laser power, the melt pool size increases. This results in more catchment of powder in the melt pool.

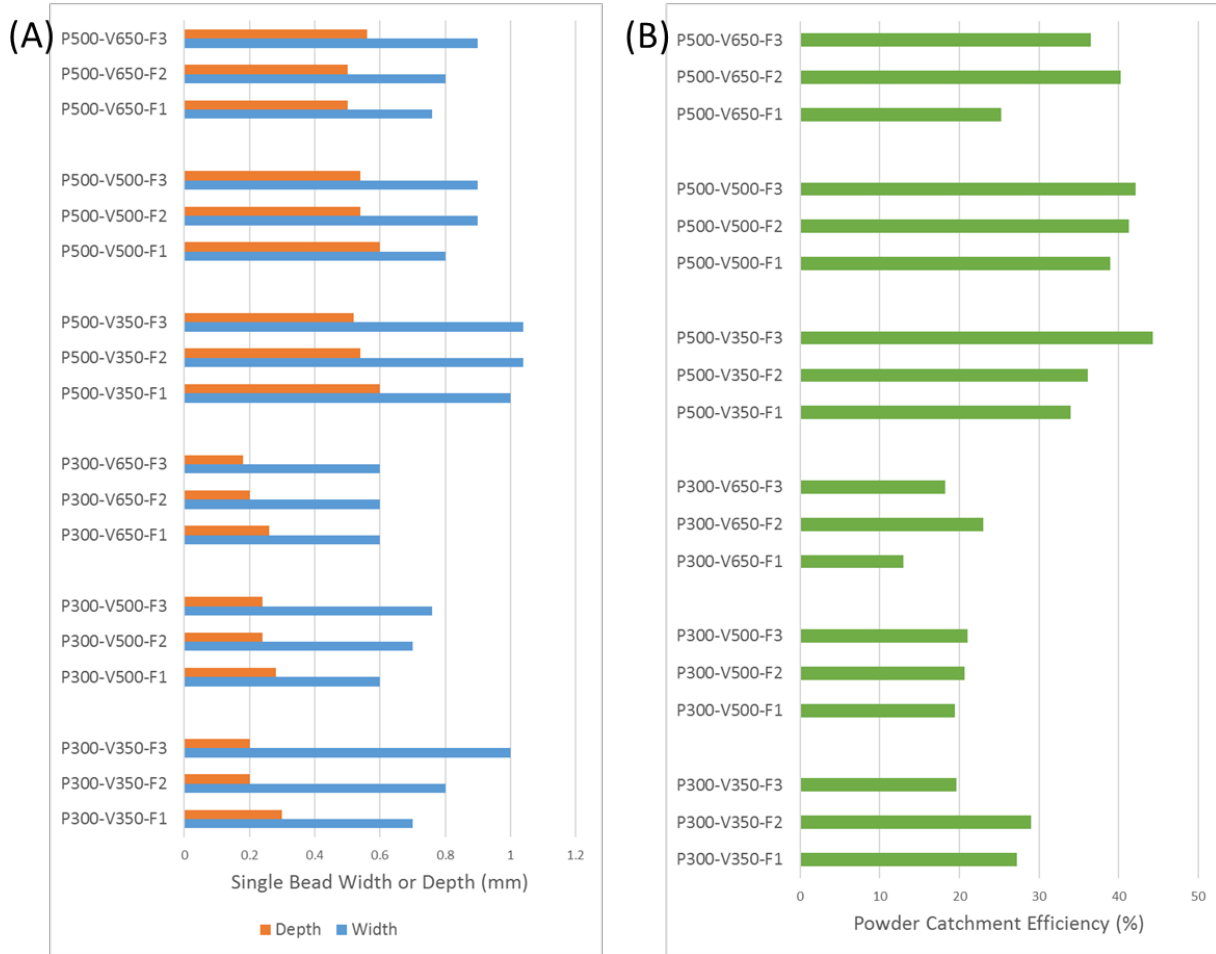


Figure 20- The variation of (A) melt pool dimensions with process parameters; (B) powder catchment efficiency with process parameters.

Table 6- Analysis of variance (ANOVA) of width, depth, and powder catchment efficiency

Factor	Width		Depth		Powder catchment efficiency	
	P-value	significance	P-value	significance	P-value	significance
P	0.0046	High	0.0002	Very high	0.0006	Very high
V	0.0154	Relatively high	0.1886		0.1042	
F	0.1037		0.0691		0.1169	
P:V	0.8944		0.9130		0.2879	
P:F	0.7566		0.4888		0.2190	
F:V	0.8420		0.5561		0.3512	

Figure 21 shows the relationship between the ratio of melt pool boundary to melt pool area (B_{mp}/A_{mp}) and the process parameters. The analysis of variance (ANOVA) is implemented to realize the effect of critical process parameters on geometrical features of deposits (B_{mp}/A_{mp}). Table 7 illustrates that laser power has the most significant effect on the ratio of B_{mp}/A_{mp} . By comparison, the scanning speed and powder feed rate also exhibit the high influence on the B_{mp}/A_{mp} ratio. To investigate the possibility of changing B_{mp}/A_{mp} by varying process parameters of DED, two extremes of the current parameters are selected. It is observed from the Figure 21 that the highest value for B_{mp}/A_{mp} obtained at the lowest value of laser power (300 W) and powder feed rate (1 gr/min), and highest value of scanning speed (650 mm/min). By comparison, the lowest value of B_{mp}/A_{mp} is calculated at the highest value of laser power (500 mm/min) and powder feed rate (3 gr/min), and the lowest value of scanning speed (350 mm/min). Thus, it is concluded that B_{mp}/A_{mp} ratio follows a relation of proportionality with decreasing laser power and powder feed rate, and increasing scanning speed. This shows that there is a direct relationship between the laser power and powder feed rate with deposited area (A_d) Equation 19, however the scanning speed shows an inverse relationship. With increasing A_d , the melt pool area increases, and the ratio of B_{mp}/A_{mp} decreases.

Table 7- Analysis of variance (ANOVA) of B_{mp}/A_{mp}

Factor	P-value	Significance
P	0.0008	Very high
V	0.0047	High
F	0.0018	High
P*V	0.3325	
P*F	0.4008	
F*V	0.3405	

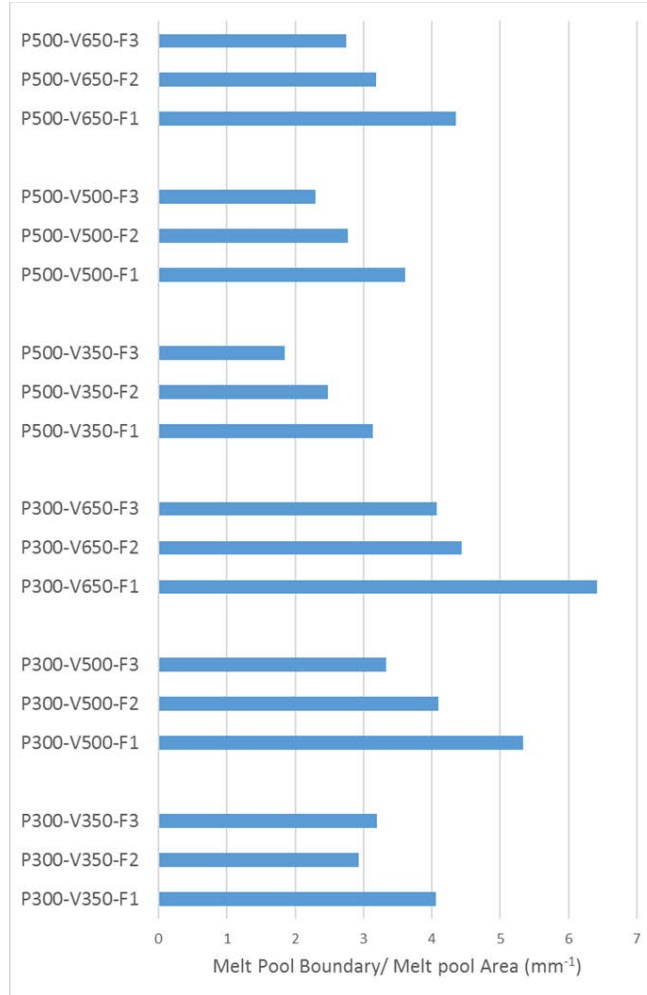


Figure 21- The variation of the ratio of melt pool boundary to melt pool area (B_{mp}/A_{mp}) with process parameters.

Figure 22 shows the microscopy images that are used to analyze the cellular spacing at various process parameters. Figure 22A depicts the cellular microstructure of a DED part printed at laser power of 500 mm/min, a powder feed rate of 3 gr/min, and a scanning speed of 350 mm/min. At these process parameters the lowest value of B_{mp}/A_{mp} is obtained. In contrast, Figure 22B shows the cellular spacing for a sample with highest value of B_{mp}/A_{mp} ratio, which is printed at a laser power of 300 W, a powder feed rate of 1 gr/min, and a scanning speed of 650 mm/min. In this work, the variation of cell spacing is investigated only for the highest and lowest

values of B_{mp}/A_{mp} ratio. Comparing these two microstructures reveal that cell spacing decreases from approximately 4 μm in Figure 22A to about 2.5 μm in Figure 22B. Reduction in cell spacing results in higher yield strength, according to the Hall-Petch relationship.

One of the main factors that influences cell spacing is cooling rate (\dot{T}) during solidification that occurs at the solid/liquid interface. Cooling rate is directly related to thermal gradient (G) and solidification rate (R), so that the higher thermal gradient and higher solidification rate lead to a higher cooling rate and consequently, finer cellular structure and lower cell spacing. As shown in Equation 17 an approximation of the cooling rate can be derived based on the ratio of B_{mp}/A_{mp} . A larger B_{mp}/A_{mp} ratio causes a faster heat transfer from melt pool to the substrate, thus resulting in higher cooling rate and finer microstructure. On the other hand, a smaller B_{mp}/A_{mp} ratio corresponds to lower cooling rates during the solidification. As expected, Figure 22B has a larger B_{mp}/A_{mp} , that results in finer microstructure and lower cell spacing. In general, cellular/dendrite spacing (λ) can be estimated theoretically as a function of R and G [26],

$$\lambda = C R^{-1/3} G^{-1/3} \quad (22)$$

where, C is a constant that depends on thermal and material properties, however is not discussed in detail, here. This theoretical model shows the influence of solidification parameters on the microstructure parameter.

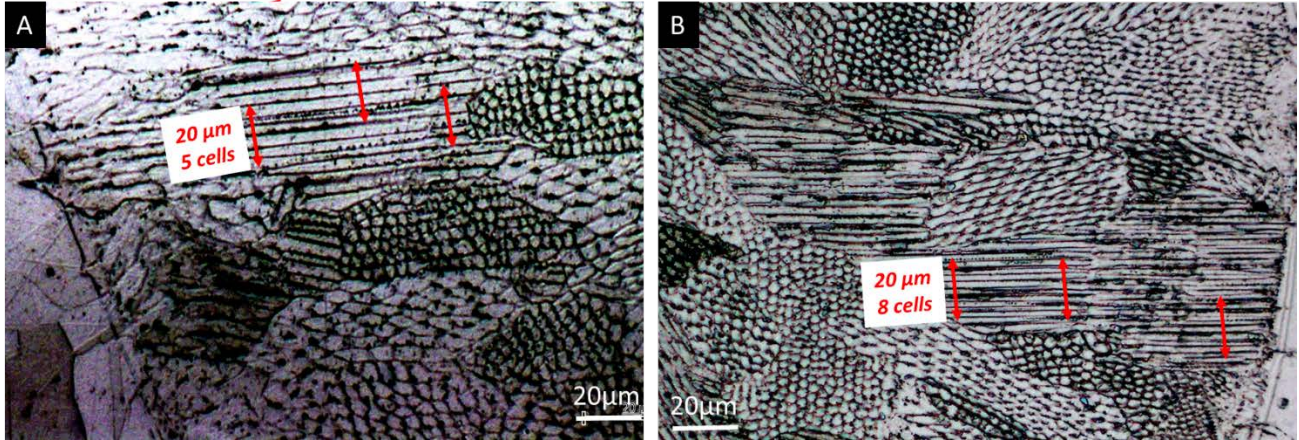


Figure 22- Optical micrographs showing cell spacing and cellular microstructure of first layer of DED deposited part (A) at laser power of 500 mm/min, powder feed rate of 3 gr/min, and scanning speed of 350 mm/min; (B) at laser power of 300 W, powder feed rate of 1 gr/min, and scanning speed of 650 mm/min.

Figure 23 demonstrates that the average yield strength of DED part is increasing from 290 MPa to 360 MPa while the ratio of B_{mp}/A_{mp} increases. The blue dashed line represents a linear relationship between yield strength and the ratio of B_{mp}/A_{mp} with the R-Squared value of 84%. The black and red dashed lines shows the fitted line plots for the upper and lower confidence bounds for all points within the range of data, using the confidence interval of 95%. The sample with lowest yield strength has been printed at laser power of 500 mm/min, a powder feed rate of 3 gr/min, and with a scanning speed of 350 mm/min, and the sample with highest yield strength has been produced at laser power of 300 W, a powder feed rate of 1 gr/min, and a scanning speed of 650 mm/min. The higher B_{mp}/A_{mp} results in a finer microstructure, therefore according to the Hall-Petch equation, grain size has a strong influence on the yield strength that is expressed as [27],

$$\sigma = \sigma_0 + kd^{-1/2} \quad (23)$$

where, σ_0 is materials constant, k is the strengthening coefficient, σ is the yield strength, and d is the diameter of grain. It has been established that B_{mp}/A_{mp} ratio changes with different process

parameters. Therefore, it can be concluded that with changing the process parameters, the yield strength will change, so that with decreasing laser power and powder feed rate, and increasing scanning speed the yield strength increases.

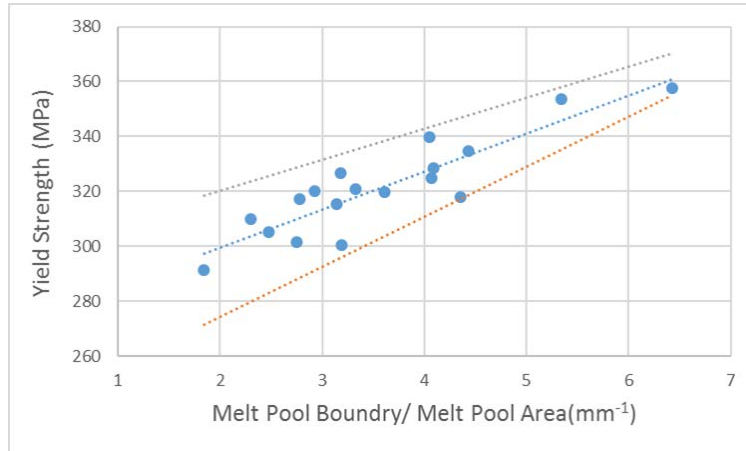


Figure 23- The variation of average yield strength with B_{mp}/A_{mp} ratio. The blue dashed line is a trend line that best fits the points. The black and red dashed lines shows the fitted line plots for the upper and lower confidence bounds.

Conclusion

In this work, the microstructure and mechanical properties of substrate/deposited material interface in a part manufactured via DED were investigated. The effect of DED process parameters (laser power, scanning speed, and powder feed rate) on microstructure and strength of the substrate/deposited material interface were examined. In order to prevent the formation of porosity, a desirable range of process parameters were selected and a specific rastering strategy was utilized. Since no porosity was detected in the DED parts, the important factors that influence the mechanical properties are the microstructure and grain size. The microstructural characterization of the part was carried out using optical microscopy and the yield strength of the interface was evaluated using block shear test. Fundamentally, the microstructure evolution during deposition, and melt pool geometry depend on heat transfer and thermal parameters of the

melt pool such as temperature gradient and heating/cooling rate. Thus, to understand the influence of process parameters on the final properties of DED part, a thermal analysis was developed to determine the melt pool geometry. The optical microscopy results showed the epitaxial nucleation and preferred cellular growth in DED part. The analysis of variance (ANOVA) was employed to relate the process parameters to geometry characteristics of the melt pool. The ratio of melt pool boundary to melt pool area (B_{mp}/A_{mp}) can be used as a factor to compare the solidification condition and therefore yield strength at different process parameters. The analysis of variance showed that laser power has the most significant effect on (B_{mp}/A_{mp}). As a result, a correlation between process parameters and the strength of interface was established. The block shear test results showed that yield strength of DED part is increasing from 290 MPa to 360 MPa while the ratio of B_{mp}/A_{mp} increases. The results showed that yield strength has a direct correlation with scanning speed, however it is inversely proportional to the laser power and powder feed rate.

References

- [1] A. Saboori, D. Gallo, S. Biamino, P. Fino, and M. Lombardi, "An Overview of Additive Manufacturing of Titanium Components by Directed Energy Deposition: Microstructure and Mechanical Properties," *Appl. Sci.*, vol. 7, no. 9, p. 883, Sep. 2017, doi: 10.3390/app7090883.
- [2] X. Xu, G. Mi, Y. Luo, P. Jiang, X. Shao, and C. Wang, "Morphologies, microstructures, and mechanical properties of samples produced using laser metal deposition with 316L stainless steel wire," *Opt. Lasers Eng.*, vol. 94, pp. 1–11, Jul. 2017, doi: 10.1016/j.optlaseng.2017.02.008.
- [3] M. Akbari and R. Kovacevic, "An investigation on mechanical and microstructural properties of 316LSi parts fabricated by a robotized laser/wire direct metal deposition system," *Addit. Manuf.*, vol. 23, pp. 487–497, Oct. 2018, doi: 10.1016/j.addma.2018.08.031.
- [4] V. Manvatkar, A. De, and T. DebRoy, "Spatial variation of melt pool geometry, peak temperature and solidification parameters during laser assisted additive manufacturing process," *Mater. Sci. Technol.*, vol. 31, no. 8, pp. 924–930, Jun. 2015, doi: 10.1179/1743284714Y.0000000701.

- [5] G. Dinda, A. Dasgupta, and J. Mazumder, "Laser aided direct metal deposition of Inconel 625 superalloy: Microstructural evolution and thermal stability," 2009, doi: 10.1016/J.MSEA.2009.01.009.
- [6] A. Yadollahi, N. Shamsaei, S. Thompson, and D. W. Seely, "Effects of process time interval and heat treatment on the mechanical and microstructural properties of direct laser deposited 316L stainless steel," 2015, doi: 10.1016/J.MSEA.2015.07.056.
- [7] M. Izadi, A. Farzaneh, I. Gibson, and B. Rolfe, "The effect of process parameters and mechanical properties of direct energy deposited stainless steel 316," *SFF 2017 Proc. 28th Annu. Int. Solid Free. Fabr. Symp. - Addit. Manuf. Conf.*, pp. 1058–1067, Jan. 2017.
- [8] M. N. Ahsan, R. Bradley, and A. J. Pinkerton, "Microcomputed tomography analysis of intralayer porosity generation in laser direct metal deposition and its causes," *J. Laser Appl.*, vol. 23, no. 2, p. 022009, May 2011, doi: 10.2351/1.3582311.
- [9] P. A. Kobryn, E. H. Moore, and S. Semiatin, "The effect of laser power and traverse speed on microstructure, porosity, and build height in laser-deposited Ti-6Al-4V," 2000, doi: 10.1016/S1359-6462(00)00408-5.
- [10] C. Zhong, T. Biermann, A. Gasser, and R. Poprawe, "Experimental study of effects of main process parameters on porosity, track geometry, deposition rate, and powder efficiency for high deposition rate laser metal deposition," *J. Laser Appl.*, vol. 27, no. 4, p. 042003, Jul. 2015, doi: 10.2351/1.4923335.
- [11] L. Wang *et al.*, "Pore Formation in Laser-Assisted Powder Deposition Process," *J. Manuf. Sci. Eng.*, vol. 131, no. 5, Oct. 2009, doi: 10.1115/1.3184087.
- [12] G. K. L. Ng, A. E. W. Jarfors, G. Bi, and H. Y. Zheng, "Porosity formation and gas bubble retention in laser metal deposition," *Appl. Phys. A*, vol. 97, no. 3, p. 641, May 2009, doi: 10.1007/s00339-009-5266-3.
- [13] M. Valdez, C. Kozuch, E. J. Faierson, and I. Jasiuk, "Induced porosity in Super Alloy 718 through the laser additive manufacturing process: Microstructure and mechanical properties," *J. Alloys Compd.*, vol. 725, pp. 757–764, Nov. 2017, doi: 10.1016/j.jallcom.2017.07.198.
- [14] A. Bandyopadhyay, F. Espana, V. K. Balla, S. Bose, Y. Ohgami, and N. M. Davies, "Influence of porosity on mechanical properties and in vivo response of Ti6Al4V implants," *Acta Biomater.*, vol. 6, no. 4, pp. 1640–1648, Apr. 2010, doi: 10.1016/j.actbio.2009.11.011.
- [15] K. Zhang, S. Wang, W. Liu, and X. Shang, "Characterization of stainless steel parts by Laser Metal Deposition Shaping," *Mater. Des.*, vol. 55, pp. 104–119, Mar. 2014, doi: 10.1016/j.matdes.2013.09.006.
- [16] Z. Wang, T. A. Palmer, and A. M. Beese, "Effect of processing parameters on microstructure and tensile properties of austenitic stainless steel 304L made by directed energy deposition additive manufacturing," *Acta Mater.*, vol. 110, pp. 226–235, May 2016, doi: 10.1016/j.actamat.2016.03.019.
- [17] T. DebRoy *et al.*, "Additive manufacturing of metallic components – Process, structure and properties," *Prog. Mater. Sci.*, vol. 92, pp. 112–224, Mar. 2018, doi: 10.1016/j.pmatsci.2017.10.001.

- [18] *Welding Metallurgy and Weldability*, 1st ed. John Wiley & Sons, Ltd, 2015.
- [19] T. L. Bergman, F. P. Incropera, D. P. DeWitt, and A. S. Lavine, *Fundamentals of Heat and Mass Transfer*. John Wiley & Sons, 2011.
- [20] W. Devesse, D. De Baere, and P. Guillaume, "High Resolution Temperature Measurement of Liquid Stainless Steel Using Hyperspectral Imaging," *Sensors*, vol. 17, no. 1, Art. no. 1, Jan. 2017, doi: 10.3390/s17010091.
- [21] "Measurement and Database Construction of Heat Transfer Coefficients of Gas Quenching," *Journal of Mechanical Engineering*. <https://www.sv-jme.eu/article/measurement-and-database-construction-of-heat-transfer-coefficients-of-gas-quenching/> (accessed Sep. 17, 2020).
- [22] J. Sears, "Measuring laser absorption coefficient during laser additive manufacturing of 316L stainless steel and Ti-6V-4Al alloys," *Int. Congr. Appl. Lasers Electro-Opt.*, vol. 2007, no. 1, p. 401, Sep. 2018, doi: 10.2351/1.5061066.
- [23] C. S. Kim, *Thermophysical Properties of Stainless Steels*. Argonne National Laboratory, 1975.
- [24] H. G. Kraus, "Experimental measurement of stationary SS 304, SS 316L and 8630 GTA weld pool surface temperatures," *Weld. J. Miami USA*, vol. 68:7, Jul. 1989, Accessed: Sep. 17, 2020. [Online]. Available: <https://www.osti.gov/biblio/5306495-experimental-measurement-stationary-ss-ss-gta-weld-pool-surface-temperatures>.
- [25] Y. Huang, M. B. Khamesee, and E. Toyserkani, "A new physics-based model for laser directed energy deposition (powder-fed additive manufacturing): From single-track to multi-track and multi-layer," *Opt. Laser Technol.*, vol. 109, pp. 584–599, Jan. 2019, doi: 10.1016/j.optlastec.2018.08.015.
- [26] M. Rappaz, and J. A. Dantzig, "Solidification," EPFL Press, 2009.
- [27] B. P. Kashyap and K. Tangri, "On the Hall-Petch relationship and substructural evolution in type 316L stainless steel," *Acta Metall. Mater.*, vol. 43, no. 11, pp. 3971–3981, Nov. 1995, doi: 10.1016/0956-7151(95)00110-H.

CHAPTER 5. CONCLUSION AND FUTURE WORK

Summary and Contribution

In this dissertation, the surface quality, geometry, microstructure and mechanical properties of 316L stainless steel parts manufactured by hybrid manufacturing were characterized theoretically, fundamentally and experimentally. The surface quality and mechanical properties play a significant role in the functionality of hybrid manufactured parts. Moreover, a new testing method was developed to evaluate the strength of interface in hybrid manufacturing.

For characterization the surface quality of manufactured parts, several experiments were performed to measure the surface roughness, waviness, and hardness at different process parameters. The effect of scanning speed, step over and laser remelting on surface roughness and surface waviness of DED parts have been examined. In most of the literatures that evaluate the surface topology of DED parts, only the effect of geometry of the beads has been investigated. However, in a few of studies, in addition to the bead geometry, the effect of partially melted particles on surface quality have been investigated. In this work, a new phenomenon which is called “lack of uniformity” that is an intrinsic feature of the DED process was found. To analyze the surface quality, in addition to bead geometry and partially melted particles, for the first time, the effect of lack of uniformity on surface quality was demonstrated. Since lack of uniformity is an accumulative phenomenon (the geometry of the current bead is affected by the geometry of the previous deposited bead), it has significant impact on the surface quality. The results showed that with decreasing step over, the more partially melted particles are remelted, and surface roughness decreases. Furthermore, the surface roughness and surface waviness of the samples significantly decreased after laser remelting. This dissertation has made

some important contributions to the deeper analysis of the nature of the hybrid manufacturing process that affects the surface quality.

In addition to surface quality, the mechanical properties are critical features of hybrid manufactured parts. In the literature, the mechanical properties of DED parts have been investigated, but the substrate and deposited part interfacial strength has not been analyzed yet. It is interesting that there was not found any standard testing method for measuring interfacial bond in hybrid manufacturing. To characterize the mechanical properties of interfacial bonding, the first step was designing and developing a new testing method that is capable of measuring the strength of interface. The important contribution that the authors made is to propose a new testing method which is called “block shear” test to characterize the mechanical properties of interface in hybrid manufacturing. For designing this test, a theoretical framework was developed to find out the dimensions of test specimens required for obtaining the shear strength. To validate this testing methodology, another group of specimens were fabricated completely by machining. In addition, the differences between tensile shear test and block shear test in terms of stress and strain distribution were analyzed theoretically and solved numerically by using finite element method. Thereafter, the numerical results were successfully verified by performing several experiments, including stress- displacement curves obtained after tensile shear and block shear tests, and fractography. The fractography observations of block shear specimens showed that the fracture takes place due to the shear stress in the interface plane, whereas in tensile shear specimens the combination of tensile fracture and shear fracture was observed. By using block shear testing method, the interfacial bonding strength of DED part was able to be successfully measured.

Finally, a desirable range of DED process parameters (laser power, scanning speed, and powder feed rate) were selected and the microstructural features and mechanical properties of parts manufactured via DED were examined. In this work, the formation of porosity was prevented by using suitable deposition strategy to improve the mechanical properties. Since no porosity was detected in the DED parts, it is expected that the strength of interface to be highly affected by microstructural features. The microstructural characterization of DED part was examined by optical microscopy and the strength of substrate/deposited material interface was evaluated using block shear test. In order to understand the influence of process parameters on the final properties of DED part, a thermal analysis was developed to determine the melt pool geometry and model the heat transfer between the molten pool and substrate. The variance analysis (ANOVA) showed that the laser power has a significant effect on the bead width and height. By comparison, the scanning speed exhibited a relatively high influence on bead width and low influence on bead depth. It was concluded that process parameters determine the cooling rate and consequently, the grain size and morphology of the interface. There is a relationship between grain size and the strength of the interface in DED part, according to Hall-Petch equation. The analysis of results showed that yield strength has a direct correlation with scanning speed, however it is inversely proportional to the laser power and powder feed rate.

Future Work

In recent years, industries such as automotive and aerospace show a growing demand in hybrid manufacturing as a cost-effective technology associated with adopting additive manufacturing to provide a more practical technique for manufacturing parts specifically net shape rapid prototyping and in-situ repairing. Since hybrid manufacturing is a newly developed

technique, the properties of parts that are manufactured with this process are not fully understood. To validate the thermal model proposed in this dissertation, more experiments can be performed on different substrates with different thermal properties as a future work.

In addition, more research is needed on characterizing microstructure and mechanical properties of dissimilar joints built by hybrid manufacturing. One of the main challenges of hybrid manufacturing of dissimilar metals is the formation of bi-metallic structures at the interface as a result of different crystallographic characteristics and thermal properties. The testing method developed can be used to evaluate the strength of interface in dissimilar joints manufactured by hybrid manufacturing. In addition to mechanical properties, the microstructural features and particularly the intermetallic structures and their effects on mechanical properties can be studied.

Future work can also focus on numerical (finite element analysis) or analytical simulation of DED process and develop a modeling framework to predict thermal history during deposition as well as microstructural evolution, and strength of interface at a given value of process parameters. Based on the temperature distribution during deposition, it is possible to predict grain size and consequently the strength of interface.